1-1-2013

Evolution of Microstructure of Haynes 230 and Inconel 617 Under Mechanical Testing At High Temperatures

Kyle Hrutkay
University of South Carolina

Recommended Citation

Hrutkay, K.(2013). *Evolution of Microstructure of Haynes 230 and Inconel 617 Under Mechanical Testing At High Temperatures.* (Master's thesis). Retrieved from http://scholarcommons.sc.edu/etd/2365

EVOLUTION OF MICROSTRUCTURE OF HAYNES 230 AND INCONEL 617 UNDER MECHANICAL TESTING AT HIGH TEMPERATURES

by

Kyle Hrutkay

Bachelor of Science
Colorado State University, 2010

Submitted in Partial Fulfillment of the Requirements

For the Degree of Master of Science in

Nuclear Engineering

College of Engineering and Computing

University of South Carolina

2013

Accepted by:

Djamel Kaoumi, Director of Thesis

Anthony Reynolds, Reader

Lacy Ford, Vice Provost and Dean of Graduate Studies

ACKNOWLEDGEMENTS

First, I would like to thank my family and friends for their unwavering support during this period of research. Without your encouragement I could never have successfully finished this thesis. Thank you Kimberly, my mother who continued to energize me in this long process.

My thesis advisor, Dr. Djamel Kaoumi, who helped make this project a success: without your guidance this project would not have been completed with such vision. It was a pleasure learning from you during this process and your continual insight made this thesis better in every way.

I would also like to thank my research team who offered their guidance in my daily work. Thank you Jimmy Adamson, for providing me with any assistance I required; thank you David Catalini, for contributing your technical help to the project; and thank you Bo-Shiuan Li, for sharing this experience with me from beginning to end. It was my fellow researchers who related to my challenges and ultimately helped me conquer them.

Thank you everyone for supporting me and for your help in making this project possible; I am forever grateful for your assistance and the time you took out of your lives helping me make this thesis a success.

ABSTRACT

Haynes 230 and Inconel 617 are austenitic nickel based superalloys, which are candidate structural materials for next generation high temperature nuclear reactors. High temperature deformation behavior of Haynes 230 and Inconel 617 have been investigated at the microstructural level in order to gain a better understanding of mechanical properties. Tensile tests were performed at strain rates ranging from 10^{-3}-10^{-5} s^{-1} at room temperature, 600 °C, 800 °C and 950 °C. Subsequent microstructural analysis, including Scanning Electron Microscopy, Transmission Electron Microscopy, Energy-Dispersive X-ray Spectroscopy, and X-Ray Diffraction were used to relate the microstructural evolution at high temperatures to that of room temperature samples. Grain sizes and precipitate morphologies were used to determine high temperature behavior and fracture mechanics.

Serrated flow was observed at intermediate and high temperatures as a result of discontinuous slip and dynamic recrystallization. The amplitude of serration increased with a decrease in the strain rate and increase in the temperature. Dynamic strain ageing was responsible for serrations at intermediate temperatures by means of a locking and unlocking phenomenon between dislocations and solute atoms. Dynamic recrystallization nucleated by grain and twin bulging resulting in a refinement of grain size. Existing models found in the literature were discussed to explain both of these phenomena.

TABLE OF CONTENTS

LIST OF TABLES

LIST OF FIGURES

LIST OF ABBREVIATIONS

AC	Active Case Detection
ACR	Adequate Clinical Response
BCC	Body-Centered Cubic
DDI	Dislocation-Dislocation Interaction
DRX	Dynamic Recrystallization
DSA	Dynamic Strain Ageing
DSI	Dislocation-Interaction
EBSD	Electron Backscatter Diffraction
EDM	Electron Discharge Machining
EDX	Energy Dispersive Spectroscopy
FCC	Face-Centered Cubic
FESEM	Field Emission Scanning Electron Microscopy
GBS	Grain Boundary Serration
IHX	Intermediate Heat Exchanger
MRF	Materials Research Furnace
PLC	Portevin-Le Chatelier

SEM	Scanning Electron Microscopy
TEM	Transmission Electron Microscopy
UTS	Ultimate Tensile Strength
VHTR	Very High Temperature Reactor
XRD	X-Ray Diffraction
YSA	Yield Strength Anomaly

CHAPTER 1

Introduction

Researchers in nuclear energy are putting every effort into developing the economical use of Very-High Temperature Reactors (VHTR). Material limitations are one of the biggest obstacles engineers face in advancing these next generation designs. Due to the extreme temperatures faced in these reactors, many materials cannot withstand the heat for extended periods of time. With outlet gas temperatures as high as 900-1000 °C, current steels and alloys simply cannot withstand the reactor environment. The necessary material requires creep resistance, oxidation resistance, microstructural stability, and excellent mechanical properties.

Several studies have focused on INCONEL 617 as a possible choice for the intermediate heat exchanger (IHX) in the VHTR. However, there are other alloys which need to be studied as a possibility for the heat exchanger. Haynes 230 is a solid-solution nickel-based alloy with excellent oxidation resistance, superior creep-rupture strength, thermal stability, and fatigue resistance [1]. Fewer studies have been carried out on the microstructure of Haynes 230, and therefore these two alloys will be the focus of this research.

Both of these alloys are austenitic superalloys having a face-centered cubic (FCC) crystal structure. Their outstanding strength at high temperatures has widely been attributed to solid solution strengthening and the formation of secondary $M_{23}C_6$ carbides along grain boundaries [2]. Because creep is a diffusion controlled phenomenon, Haynes

230 has superior creep resistance over alloys containing cobalt because tungsten diffuses slower in nickel than cobalt [1]. Grain boundary carbides provide impediments to dislocations, which enhances creep strength [3]. Also, a protective oxide layer is formed by the addition of chromium and aluminum, offering oxidation and carburization resistance.

1.1 Research Objectives

The research presented in this thesis used Inconel 617 and Haynes 230 to investigate five primary objectives, listed below:

1. Examine the dependence of mechanical properties on deformation conditions, including temperature and strain rate.
2. Examine the tensile stress-strain curves of Haynes 230 and Inconel 617 as a function of temperature and strain rate.
3. Evaluate the mechanisms causing stress oscillations during high temperature tensile testing.
4. Compare the microstructural behavior of Haynes 230 and Inconel 617 and determine the relationship between microstructure changes and mechanical behavior.

1.2 Thesis Overview

In this investigation, microstructure behavior of Inconel 617 and Haynes 230 during hot tension were investigated at the expected temperatures of operation in the VHTR. Elevated temperature uniaxial tension was performed at varying temperatures, environments, and strain rates. Resulting behavior was related to corresponding microstructural development. Multiple microscopy techniques, such as scanning electron microscopy (SEM), energy-dispersive x-ray spectroscopy (EDX), x-ray diffraction (XRD) and transmission electron microscopy (TEM) were used to investigate microstructural evolution, grain morphology, carbide evolution, dislocation motion, and possible recrystallization mechanisms. The deformation and recrystallization behavior was compared to the similar superalloy Inconel 617 to determine the effect of alloying and initial microstructure on hot deformation behavior.

Chapter 1 contains the background section on hot deformation and recrystallization behavior. The background describes the effects of grain sizes, deformation conditions, precipitates and stacking fault energies on the microstructural evolution and behavior. The mechanisms for dynamic and static recrystallization described in the literature are discussed as a prelude to the work on Inconel 617 and Haynes 230. Previously proposed models for recrystallization during hot deformation have shown tremendous differences, so understanding the limitations of such models is essential for applying them to new materials and deformation conditions. The background in Chapter 1 discusses some of these limitations, proposes reasons for some of the controversy in the literature, and describes recrystallization behavior. The effects of initial microstructures and stacking fault energies on texture evolution and recrystallization mechanisms are also described. Chapter 1 also explores the phenomenon of dynamic strain ageing (DSA) and the associated macroscopic effect of known as Portevin-Le Chatelier (PLC) effect. Different theories are presented explaining the mechanisms behind DSA and the resulting effect these have on mechanical properties.

The experimental procedures are described in Chapter 2, including the methods used for hot tension testing and subsequent microstructural analysis. Specific operating conditions for scanning electron microscopy, x-ray diffraction, and transmission electron microscopy are provided. The design of the experimental procedures is also discussed and related to some of the discrepancies in recrystallization mechanisms and modeling, which are discussed in Chapter 1.

The results and discussion, presented in Chapters 3 and 4, use Haynes 230 as a model material for further understanding deformation behavior and microstructure of austenitic materials at high temperatures. Regions of the stress-strain curves are analyzed and compared to Inconel 617, proposing possible mechanisms driving the shape of the curves. Precipitate and grain evolution assist in understanding characteristics in the stress-strain curves and describing the modes of deformation and recrystallization at varying temperatures, strains, and strain rates. Mechanisms causing stress oscillations are also explored as they vary by temperature and strain rate. Models for steady state flow behavior and recrystallized grain size are presented for Haynes 230 and Inconel 617 with a detailed description on their development and limitations.

Finally, a summary of conclusions and future work are detailed in Chapters 5 and 6. Important aspects such as redistribution of precipitates, grain changes, recrystallization modes, and their relation to the stress-strain curves are all concisely summarized.

1.3 Literature Review

The following section goes into detail about the possible deformation mechanisms which may be encountered during tensile testing of Inconel 617 and Haynes 230. A literature review of the high temperature phenomena of recrystallization, grain boundary serration (GBS), and DSA is conducted. The effects of annealing twins and the resulting deformation behavior are also explored.

1.3.1 Dynamic Recrystallization

During hot deformation of a crystalline metal two competing processes may occur: strain-hardening and softening [4]. Strain-hardening is due to an increase in the dislocation density acting under external forces. On the other hand, softening consists of a decrease in dislocation density by a redistribution of dislocations into more energetically stable configurations. The mechanisms related to softening are time dependent and strongly relate to temperature, the amount and rate of deformation, stacking fault energy, initial structural state and the phase composition of the material [5].

Dynamic recovery and dynamic recrystallization are the two softening processes which work against strain hardening when a crystalline material is deformed at high temperatures. Generally dynamic recovery is the dominant mechanism which leads to the annihilation of pairs of dislocations. It also tends to occur at temperatures below 0.5 that of the melting point. However, materials with a moderate to low stacking fault energy more generally exhibit dynamic recrystallization. Each dislocation has a small strain field around it which adds to the material's stored energy. Recovery occurs when two dislocations with opposite strain fields meet and annihilate each other. This is true of several metals including silver, copper, and nickel [4]. Nickel, of interest in this study, has a stacking fault energy around 90 mJ/m^2 [6, 7]. Unlike dynamic recovery, dynamic recrystallization is less well understood and will thus be a topic of study in this research.

Recrystallization is a collective term applied to stages in which crystal orientation is altered by the passage of high-angle grain boundaries through the material [8]. At high temperatures, when dynamic recrystallization takes place during tension of the material it has a softening effect reflected in the stress-strain curve. This is a mechanism in which dislocations are eliminated by the migration of high angle boundaries. Due to a higher density of dislocations at higher temperatures, dynamic recovery cannot completely eliminate all of the dislocations, which leads to localized areas of high dislocation density as the material is stressed. This process can have a significant effect on the stress-strain curve of the material at high temperatures. Should the strain at which recrystallization begins, ε_{cr}, become greater than the strain caused by recrystallization, ε_x, then the recrystallization occurs periodically [4, 5]. The macroscopic effect of this event is a serration in stress flow as the material alternates between softening and hardening cycles.

Strain rate plays the largest factor in dynamic recrystallization [5, 9-11]. Generally, a high strain rate will produce a single peak recrystallization, while a lower strain rate will produce cyclic recrystallization consistent with the periodicity of softening and hardening.

In one of the first studies conducted on dynamic recrystallization, Luton et. al analyzed the mechanical aspects of the process. They showed that the transition from periodic to continuous behavior is associated with different strain rate. By conducting a torsion test on nickel they showed at low strain rate, recrystallization is cyclic (see Figure 1.1a) and conversely at relatively high strain rates recrystallization is continuous (see Figure 1.1b) [12]. In a study conducted by Coryell et. al, the flow behavior of Incoloy alloy 945 was characterized in the high temperature range of 950-1150 °C. By varying the strain rates between 0.001-1.0 s^{-1}, the researchers could observe the extent of recrystallization. The microstructure of a specimen deformed at 1.0 s^{-1} is more recrystallized than that deformed at 0.1 s^{-1}, indicating that there is a transition from static to dynamic recrystallization in this fast strain regime. However, at even slower strain rates the extent of recrystallization again increases, suggesting that both static and dynamic recrystallization are taking place [13].

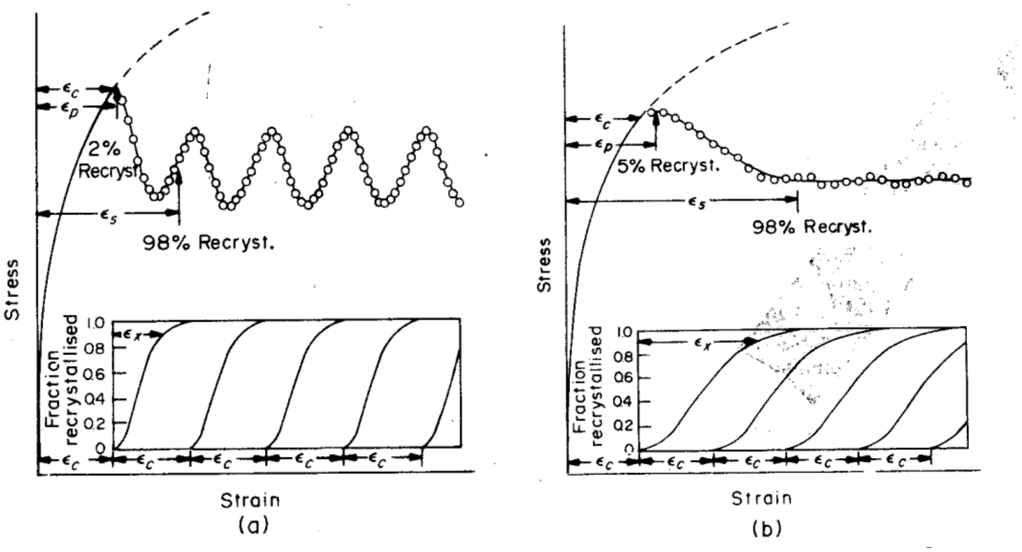

Figure 1.1. Predicted stress-strain curves for dynamic recrystallization a) critical strain to initiate recrystallization, $\varepsilon_c > \varepsilon_x$ b) $\varepsilon_c < \varepsilon_x$ [12]

Temperature is also an important parameter as dynamic recrystallization is a hot deformation mechanism [5, 13, 14]. The degree of recrystallization is closely related to temperature of the experiment. In a 2010 study, Li et. al, conducted compression tests on Inconel 625 in the temperature range 900-1200 °C. They observed that with increasing deformation temperature, the volume fraction of recrystallized grains increases as well. Full recrystallization occurred at a deformation of 0.7 at 1150 °C. As can be seen in Figure 1.2, grain refinement occurred as the grains continued to recrystallize [14]. The degree of recrystallization has a direct correlation to the oscillations seen in the flow curves. As evidenced in Figure 1.3, Petkovic et. al observed an increased occurrence of serration with increasing temperature [15].

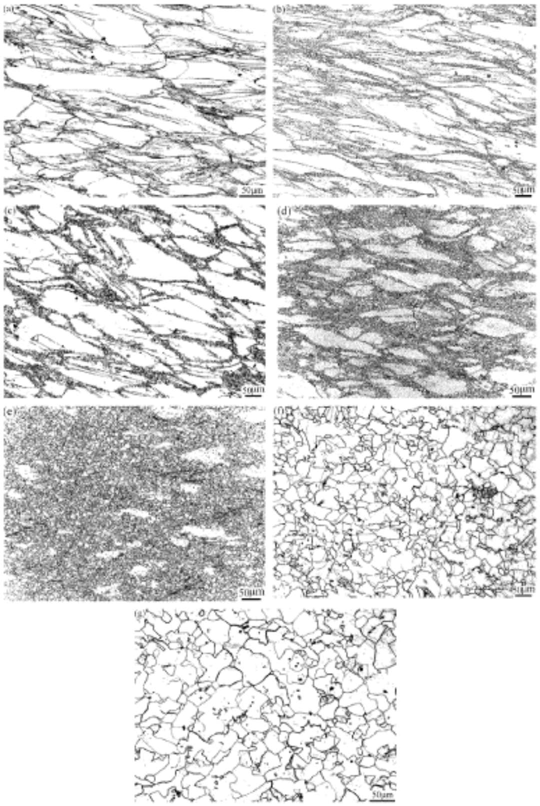

Figure 1.2 Optical micrograph of Inconel 625 superalloy deformed to 0.7 true strain at different temperatures with a strain rate of 0.1 s^{-1}: a) 900 °C, b) 950 °C, c) 1000 °C, d) 1050 °C, e) 1100 °C, f) 1150 °C, g) 1200 °C [14]

However, in a more recent investigation on Inconel 617, Rahman et. al found evidence suggesting that different deformation mechanisms occur at different temperatures and different strain rates. The study conducted tensile tests on specimens at 600 °C and 800 °C with straining rates between 10^{-6} and 10^{-3} s^{-1}. Interestingly, at 600 °C the amplitude of the stress oscillation was as high as 25 MPa, compared to only 5 MPa at 800 °C (Figure 1.4). Researchers also observed a significant increase in yield strength, ultimate tensile strength, and elongation with faster straining rates. The study has suggested two different deformation mechanisms at the different temperatures. At 600 °C, the serrated flow was attributed to carbon insterstitial atoms locking and releasing mobile dislocations. On the other hand, a thermally assisted climb mechanism released the dislocations causing a lower amplitude serrated flow at 800 °C [11].

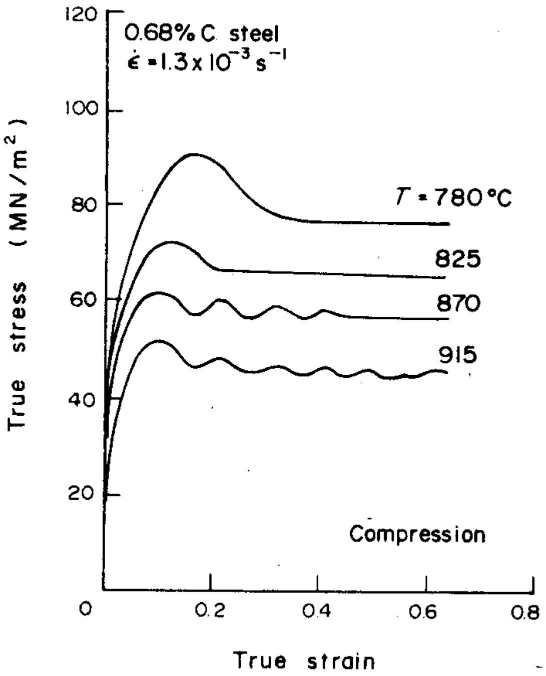

Figure 1.3 Effect of temperature on the flow curves determined in axisymmetric compression on 0.68% C steel at a strain rate of 1.3 x 10^{-3} s^{-1}

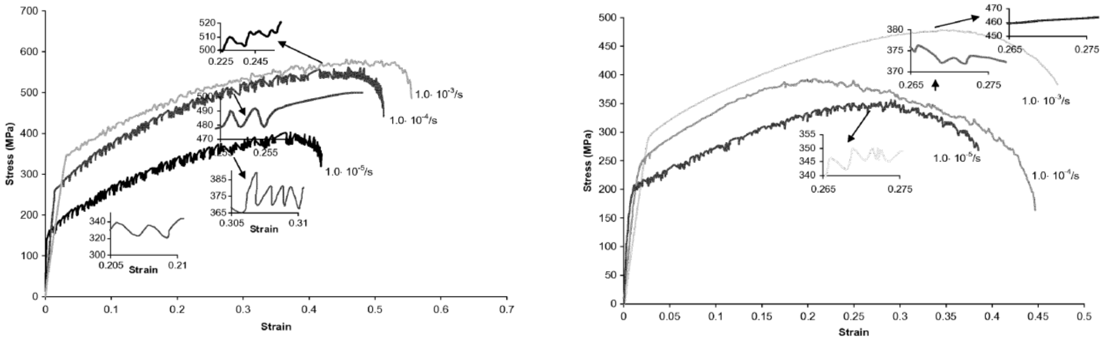

Figure 1.4 Engineering stress vs strain curve of alloy 617 at different strain rates at a) 600 °C, and b) 800 °C [11]

Several aspects of dynamic recrystallization have yet to be fully understood [5]. Grain size of the newly recrystallized grains still requires a more thorough investigation. Studies have shown both grain refinement and grain coarsening following recrystallization. Another puzzling matter is grain morphology as some grains have an elongated structure while others remain equiaxed. There are still contradicting studies on the effect of temperature and its role in flow serration. Some suggest that serrations increase indefinitely with temperature while other studies have observed a maximum intermediate temperature. Finally, evidence of the mechanisms leading to the serrations observed in the flow curves have yet to be elucidated. Some studies have suggested that the amplitude of serrations simply increases with temperatures while others have seen a maximum amplitude at intermediate temperatures with a decrease in size at higher temperatures. This study will examine all of these aspects as microstructural characteristics and mechanical properties are explored.

1.3.2 Grain Boundary Serration

Grain boundary serration is a phenomenon observed when materials are aged or deformed at high temperatures. This is one mechanism by which many superalloys draw their superior strength. By transforming from a straight edge to one with a wave-like structure, the serrations resist grain boundary sliding [16-18]. During deformation grain boundary serration can also enhance dynamic recrystallization as the bulged area surrounded by the serrated boundaries act as a nucleus for the recrystallization of a new grain [18]. The mechanism is still not well understood and will be a focus of the present research.

GBS has been linked to the diffusivity of carbon in an austenitic matrix [16]. In a study conducted by Kim et. al, the authors subjected austenitic stainless steel to several aging temperatures without stress. By calculating the activation energy for GBS and comparing this value to the activation energy for lattice diffusion of carbon in γ-iron, the authors concluded that the two were directly linked. As seen in Figure 1.5 the grain boundary experiences serrations of greater depth with a longer aging treatment, offering a direct correlation to the diffusivity of carbon [17].

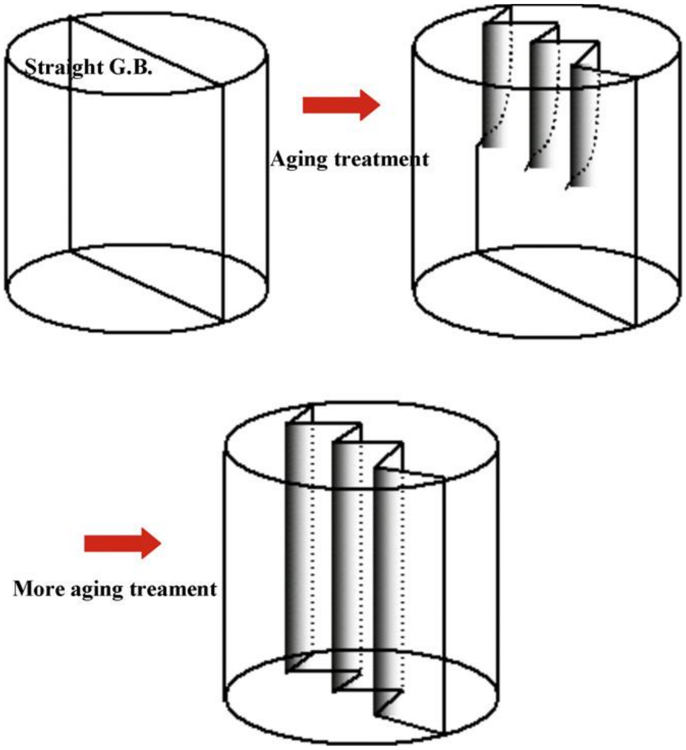

Figure 1.5 Schematic model of the grain boundary serration [17]

In a more recent study Jiang et. al, examined the effects of the $M_{23}C_6$ carbide on the formation of GBS in Haynes 230. Again, by way of ageing processes the authors could study the effect that carbon plays as well as the role of temperature. They discovered that the amplitude of serrations and the proportion of serrated boundaries increase with the rise of the solution heat treatment applied to the alloy. More importantly they found that initial M_6C carbides dissolve at high temperature and the carbon atoms then diffuse to grain boundaries to participate in the nucleation and growth of $M_{23}C_6$ carbides. These planar $M_{23}C_6$ carbides result in the formation of GBS at some grain boundaries preferentially, but then expands to nearly all boundaries during cooling [16].

As stated before GBS is effective in improving the creep life and creep ductility in a material. Tanaka performed a study in which he aged cobalt-base superalloys to transform some grain boundaries into serrated grain boundaries while leaving others with straight grain boundaries [19]. Following the heat treatments creep-rupture tests were performed on the samples. He found that those with serrated edges were more ductile and reached a greater elongation than those with straight edges. He proposed that serrated grain boundaries are effective in retarding the initiation and growth of grain boundary cracks.

1.3.3 Twinning

Twinning is a phenomenon by which the interior crystal lattice within the same grain transforms into a mirror image of the exterior lattice [20-22]. Most metallic crystals exhibit some amount of twinning in one form or another. However, twins can be broken down into two categories: those induced by mechanical deformation, and those induced by annealing. Generally, body-centered cubic (BCC) metals will exhibit deformation twinning while face-centered cubic (FCC) metals display annealing twins [22].

In a BCC metal, the crystal lattice will deform through slip or twins. As a metal is stressed uniaxially the crystal lattice may slip one atomic distance causing a heterogeneous deformation in a localized area. As a means to save energy that same metal may also deform homogeneously in shear by the formation of twins [7]. Not only does this phenomenon conserve energy, but strain is also reduced as atoms move less than a full atomic distance, as is seen in slipping [22, 23]. Shown in Figure 1.6, the twinned structure only moves a fraction of an atomic distance compared to the original structure. Because twinning is a strain hardening process, some studies have suggested that the mechanism causes serrations in stress-strain curves during tensile tests [22, 23].

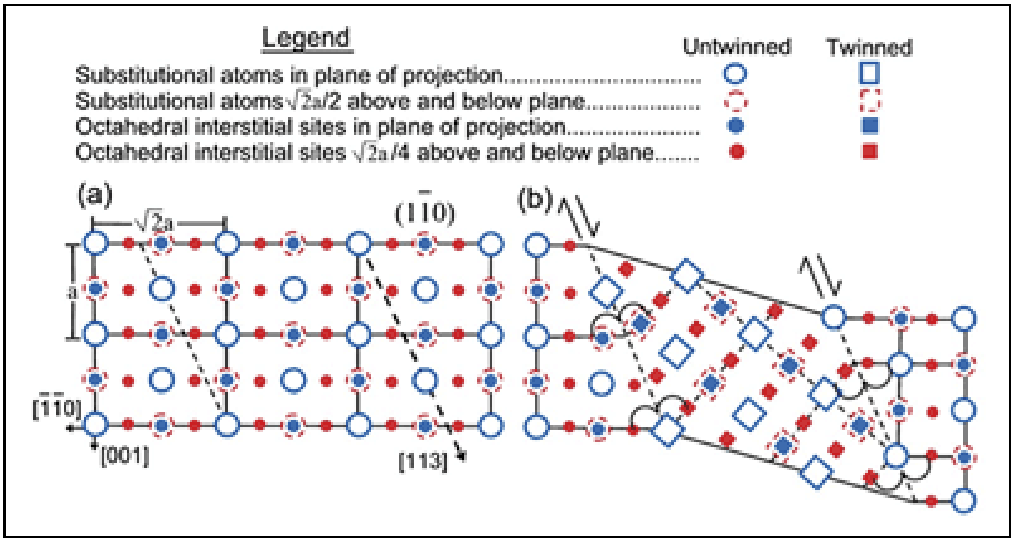

Figure 1.6 a) Untwinned structure showing direction of [113] twinning shear and b) final twinned structure showing mirror symmetry across twin-matrix surface

FCC metals are far more likely to develop twins during annealing than deformation. Annealing twins can be obtained by annealing cold-worked metals at high temperatures for relatively short times [21]. Because twinning is a stacking fault deformation, another requirement is that the material has a low stacking fault energy [24]. Nickel meets both of these conditions and twinning has been observed extensively in nearly every nickel superalloy. Other factors affecting the frequency of annealing twins are: grain size, the temperature and time of annealing, grain boundary velocity, texture, and the degree of prior deformation [25, 26].

Annealing twins occur in FCC metals so frequently because the crystal lattice shifts an even lesser amount than is required for BCC metals. An ideal FCC crystal structure is stacked ABCABCABC. However, when a stacking fault is introduced in the form of a twin, the structure may be transformed into ABCABACBA, where the middle B is the twinning plane [22]. This concept is more easily illustrated in Figure 1.7. The stacking faults lie on consecutive (111) planes in the [11-2] direction, and are produced by the glide of Shockley partial dislocations [26].

One of the more puzzling aspects of twinning is how they nucleate in the absence of an applied stress. Out of the several models that have been proposed over the years, two have gained traction in the scientific community: growth accidents [24, 25] and the nucleation of twins by fault packets [27, 28]. The early studies of growth accidents lacked some of the mechanistic details for all of the different types of annealing twins. Pande et al. carried out a study on nickel in which they found that the change in twin density, ΔN, has a direct correlation to the change in grain size, ΔD, and the driving force for boundary migration, F:

$$\Delta N \propto \Delta D F$$

They applied this model to their results for nickel as well as previous studies carried out by Meyers and Murr which showed that stacking fault packets pop out from ledges on the grain boundaries [27]. Mahajan et. al continued work in developing models of twin nucleation. They determined that the nucleation of Shockley partials on consecutive (111) planes by growth accidents are associated with the velocity of a migrating grain boundary. Thus, they concluded the higher the velocity of the grain boundary, the higher the probability of a growth accident [26]. Combining these models it is possible to predict twin morphologies in several different FCC materials, including nickel alloys.

Twins play a major role in the strength of an alloy as they act as impediments to the normal movement of dislocations [23]. The strength of metals generally decreases as temperature increases due to the thermally assisted movement of dislocations. However, many superalloys draw superior strength at intermediate temperatures due to their high propensity to develop annealing twins. In a study conducted by Kim et. al the formation of microtwins prevailed over slip and climb of dislocations causing a minimum elongation at intermediate temperatures. The graphical results of YS, UTS, and elongation for the alloys CM247LC, Alloy 263, Haynes 230, and Hastelloy X are shown below in Figure 1.7 [29]. An increase in YS and UTS also accompanied the minimum elongation for alloy CM247LC at 800° C. Such a decrease in ductility coincided with an increase in YS, as dislocation motion was impeded by twin formation.

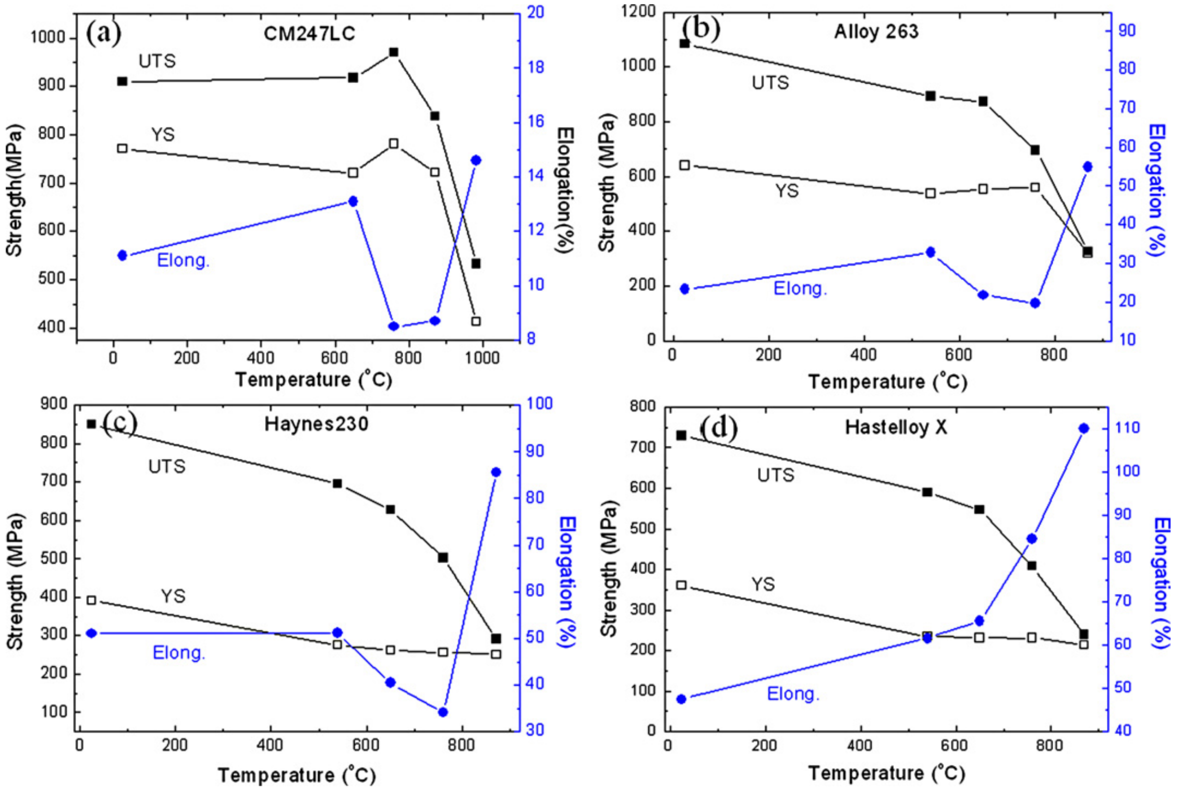

Figure 1.7 Tensile properties of the superalloys at various temperatures: a) CM247LC, b) Alloys 263, c) Haynes 230, and d) Hastelloy X [29]

1.3.4 Dynamic Strain Ageing (DSA)

The phenomenon of dynamic strain ageing (DSA) is common in alloys containing interstitial and substitutional atoms which can slow dislocation motion. Strain ageing can occur simultaneously with deformation if the deformation temperature is sufficiently high. DSA manifests itself as serrations in the stress-strain curve which is known as the Portevin-Le Chatelier (PLC) effect and will be examined in more detail in the following section.

There are two more prevalent models explaining the finer mechanisms of how DSA occurs. In the dislocation-solute interaction (DSI) model, proposed by Beukel et.

al, solute atoms interact with mobile dislocations which are pinned by obstacles causing an increase in the flow stress [30]. During the ageing time the diffusing solute atoms pin the dislocations in place [31]. Due to the lack of mobility of the dislocations no further plastic deformation can take place until a sufficiently high stress has been reached. In the dislocation-dislocation interaction (DDI) model, Kocks et. al suggested that mobile dislocations interact with forest dislocations resulting in DSA [32]. In this case mobile solute atoms move from immobile forest dislocations to mobile dislocations. This mobility results in the redistribution of solutes and affects the interaction of mobile dislocations with forest dislocations.

1.3.5 Portevin-Le Chatelier (PLC) Effect

The PLC effect describes the serrated flow in the stress-strain curve which is observed due DSA. Generally PLC takes effect when the strain rate sensitivity becomes negative and when inhomogeneous deformation begins. Oftentimes there are also macroscopic bands which form and propagate along the gauge length. Temperature, strain rate and precipitates all have an effect on the onset of serrations and the magnitude of serrations.

Temperature affects the diffusion of solute atoms through the matrix. An increased temperature will aid in solute diffusion to mobile dislocations moving due to deformation. Strain rate determines the time it takes for dislocations to overcome obstacles. Generally an increase in strain rate will cause a decrease in the critical strain necessary for serrations to begin. Finally, the presence of precipitates complicates the motion of dislocations and the diffusion of solutes. Precipitates add another obstacle to impede the motion of dislocations and also provide a place for solute atoms to form a secondary phase. These three factors all effect the types of serrations which will be observed in the stress strain curve. The five types of serrations are shown below in Figure 1.8.

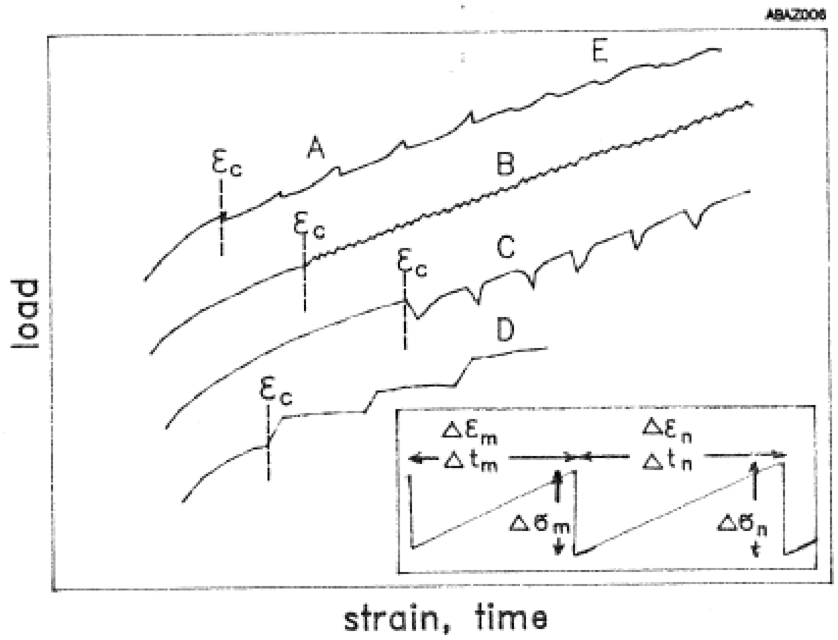

Figure 1.8 Schematic representation of five types of serration

Type A serrations show a rise and fall in stress above the general level of the stress-strain curve. They are associated with the repeated initiation and continuous propagation of deformation bands along the specimen gauge length. The initiation of each band corresponds to a yield point on the stress-strain curve which is followed by a smooth curve corresponding to band propagation. Type A serrations are usually observed at low temperatures or high strain rates and can occur alone or associated with B serrations with A predominating.

Type B serrations show a rise and fall in stress around the general level of the stress-strain curve. They are associated with discontinuous band propagation, each hop or jump of the band resulting in a serration on the stress-strain curve. Type B serrations are usually observed at intermediate temperatures and strain rates. They are usually accompanied by type A or type D.

Type C serrations show a fall and rise in stress below the general level of the stress-strain curve and are referred to as unlocking serrations. They are associated with discontinuous band propagation and are observed at high temperatures or low strain rates.

Type D serrations are observed in alloys with high stacking fault energies and consist of more or less flat plateaus separated by stress jumps. Each plateau corresponds to a deformation band propagating through the specimen from one end to the other. The bands are called plateau bands. These serrations occur alone or accompanied by those of type B, and are usually observed at high temperatures or low strain rates.

Type E serrations are irregular serrations and are observed at high strains. Type E serrations cancel type A serrations if type A comes before type E. Type E serrations can also be associated with type B and C serrations and usually occur at low temperatures or high strain rates.

CHAPTER 2

Materials and Experimental Methods

This chapter outlines the methods used to characterize the microstructure including testing procedures, sample preparation, and microscopy techniques. The composition and processing of the as received material is also presented.

2.1 Materials

Solid-solutioned strengthened Inconel 617 and Haynes 230 sheets were provided by California Metal & Supply Inc. Inconel 617 came in the form of a 0.063" (0.060"-0.066") x 48" x 18" sheet. This sheet was then cut by EDM to provide for samples with a thickness of 0.025". Haynes 230 was provided in a 0.020" (0.019"-0.022") x 36" x 16.50" sheet.

2.1.1 Chemical Composition

The chemical composition of Haynes 230 and Inconel 617 sheets are provided below in Table 2.1. All values are listed in weight percent.

Table 2.1 Weight percent chemical compositions of nickel superalloys

	Haynes 230	Inconel 617
Al	0.45	1.13
B	0.003	0.005
C	0.11	0.09
Co	0.29	11.49
Cr	21.84	22.29
Cu	0.04	0.04
Fe	1.75	2.17
La	0.022	-
Mn	0.49	0.09
Mo	1.50	9.72
Ni	Bal	Bal
P	0.005	0.003
S	0.005	0.001 max
Si	0.35	0.05
Ti	0.01 max	0.32
W	13.87	-
Zr	0.01 max	-

2.1.2 Microstructure

A large emphasis was placed on the microstructural analysis of the as-received sheets of Inconel 617 and Haynes 230 in order to provide a benchmark to compare with deformed samples.

Figure 2.1 shows a low magnification SEM micrographs of the grains of Inconel 617 in solution annealed condition. Using ImageJ software the average grain size of the undeformed alloy was determined to be about 30 µm. The solution annealed microstructure showed equiaxed grains with precipitates located primarily along grain boundaries, but also with some small precipitates located intragranularly as seen in Figure 2.1a. Also, some of the larger precipitates were seen to be deformed due to mechanical working of the sheet so that the precipitate extends in the rolling direction. There is also evidence of twins of some of the grains as seen in Figure 2.1d.

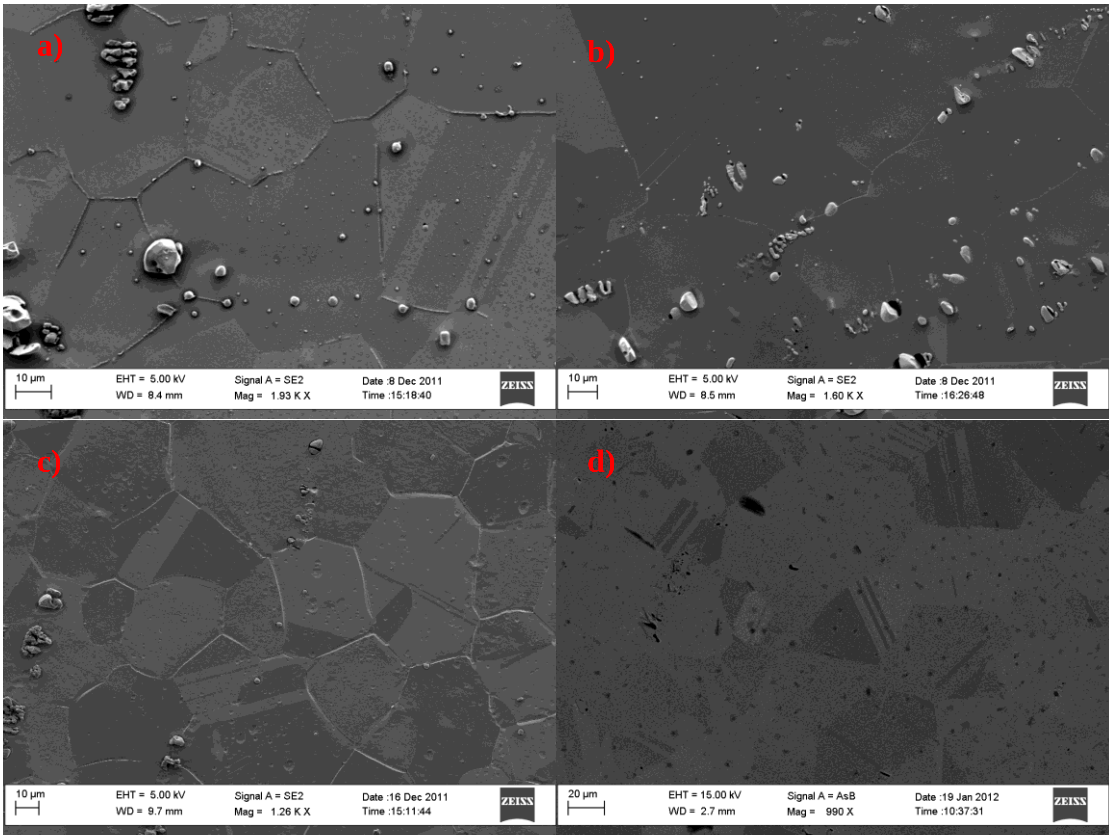

Figure 2.1 Low magnification SEM micrographs of Inconel 617 showing a) inter and intra-granular precipitates b) deformed precipitates in the rolling direction c) equiaxed grains and d) the presence of twins in some grains

The precipitates present in the microstructure were primarily carbides found on grain boundaries, with fewer appearing intra-granularly. The primary carbides were M_6C, with smaller, secondary $M_{23}C_6$ carbides [11]. Shown in Figure 2.2 are typical precipitates with corresponding EDX analysis revealing that the precipitates in Inconel 617 are Cr and Mo-rich. Notice in all of the figures the morphology of the carbides which are heavily faceted. The size of the carbides varied anywhere between 400 nm-1000 nm.

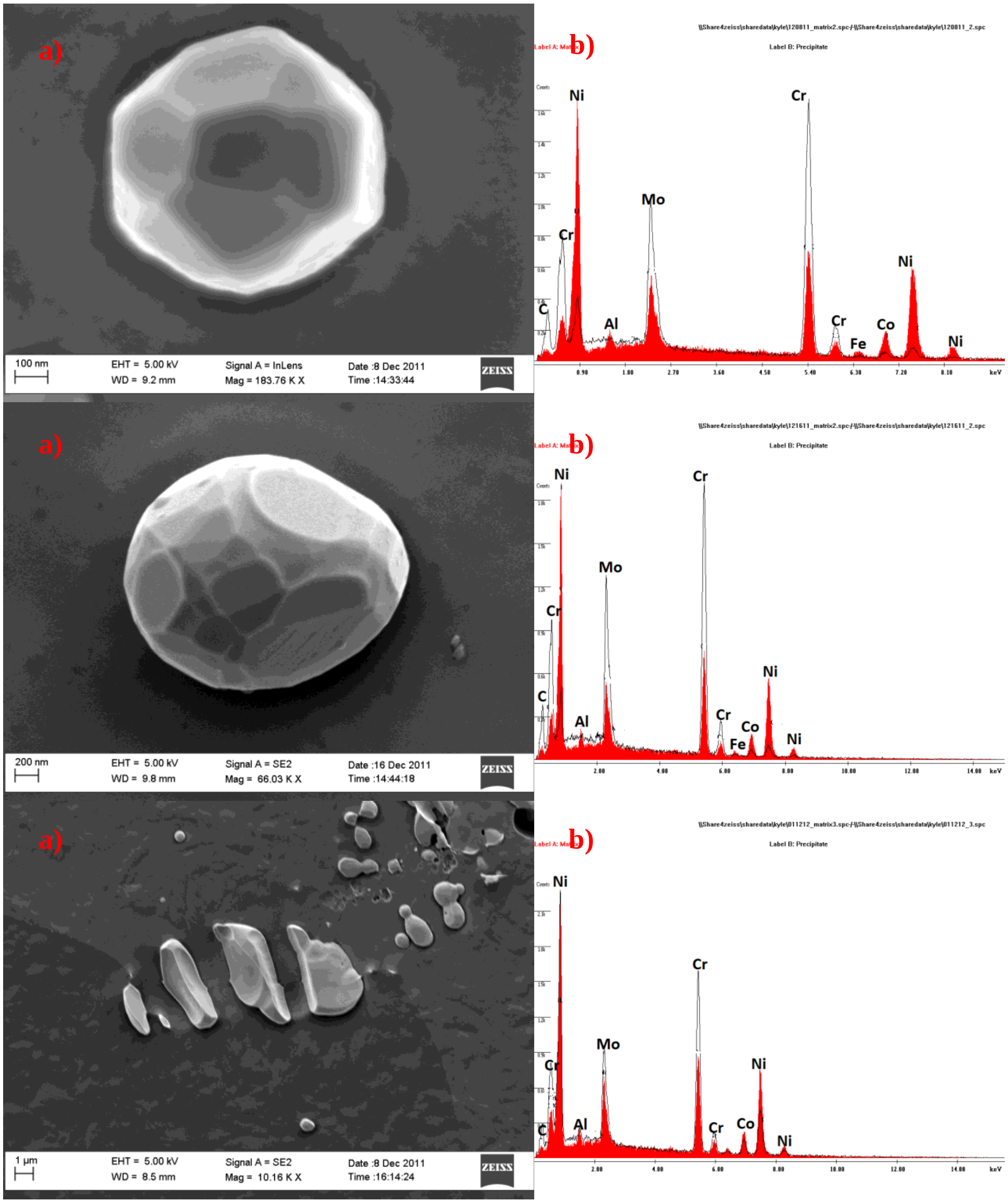

Figure 2.2 a) Cr and Mo rich carbide present in Inconel 617 with b) EDX analysis

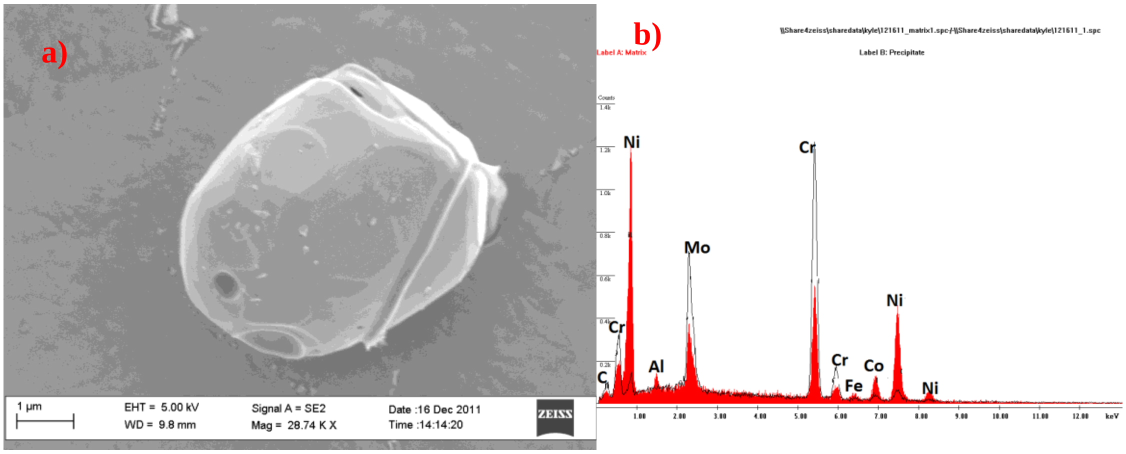

Figure 2.2 a) Cr and Mo rich carbide present in Inconel 617 with b) EDX analysis

Further evidence of the nature of the carbides can be seen in the elemental maps shown in Figure 2.3. These maps again show that the carbides are rich in chromium and molybdenum while the matrix is primarily made up of nickel.

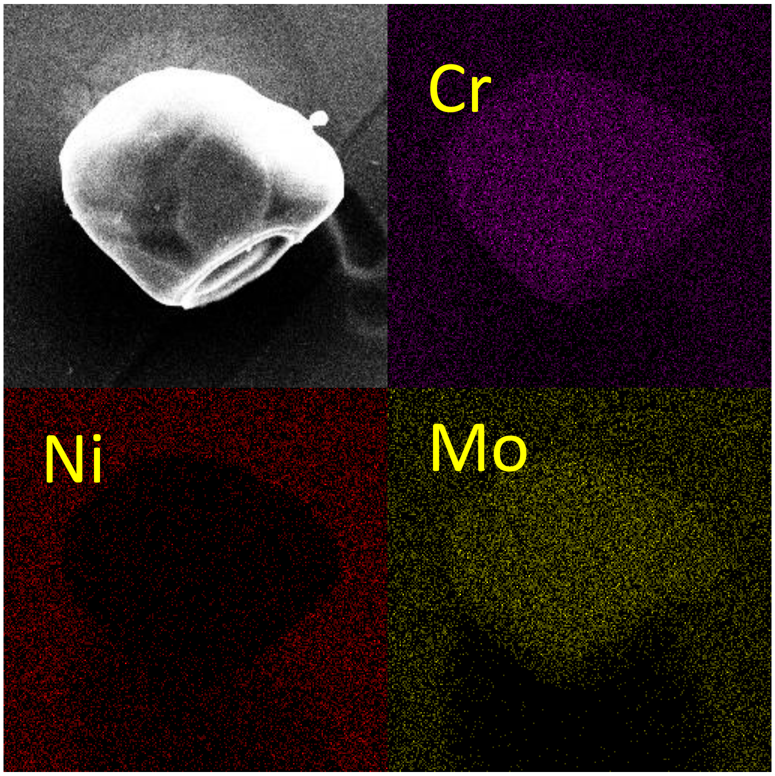

Figure 2.3 Elemental maps of carbide precipitates of Inconel 617

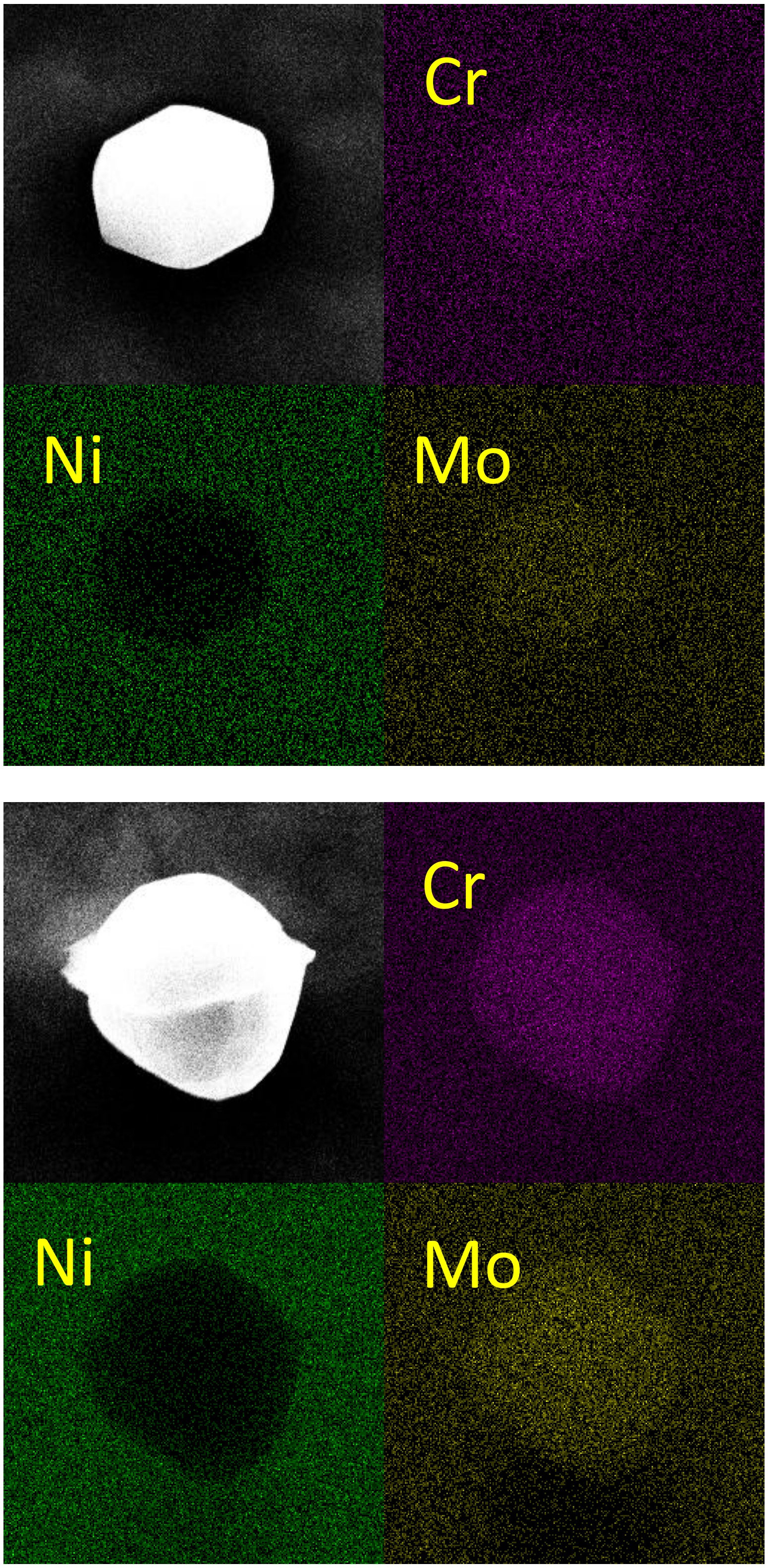

Figure 2.3 Elemental maps of carbide precipitates of Inconel 617

The as-received Haynes 230 showed similar microstructural features to those of Inconel 617. Haynes 230 showed the same large, equiaxed grains as Inconel 617 and these were measured to be an average of 46 µm. Appendix A shows the images of Inconel 617 and Haynes 230 used to calculate grain sizes. The solution annealed Haynes 230 had several annealing twins present throughout the matrix as can be seen in Figure 2.4b, to a greater extent than those observed in Inconel 617. Finally, strings of large, deformed precipitates were present along the rolling axis as seen in Figure 2.4a. These were the M_6C type carbides, while smaller $M_{23}C_6$ type carbides were found intragranularly as can be seen in Figures 2.4d. Both types of carbides were rich in tungsten and molybdenum as is evidenced in the EDX analysis of Figure 2.5.

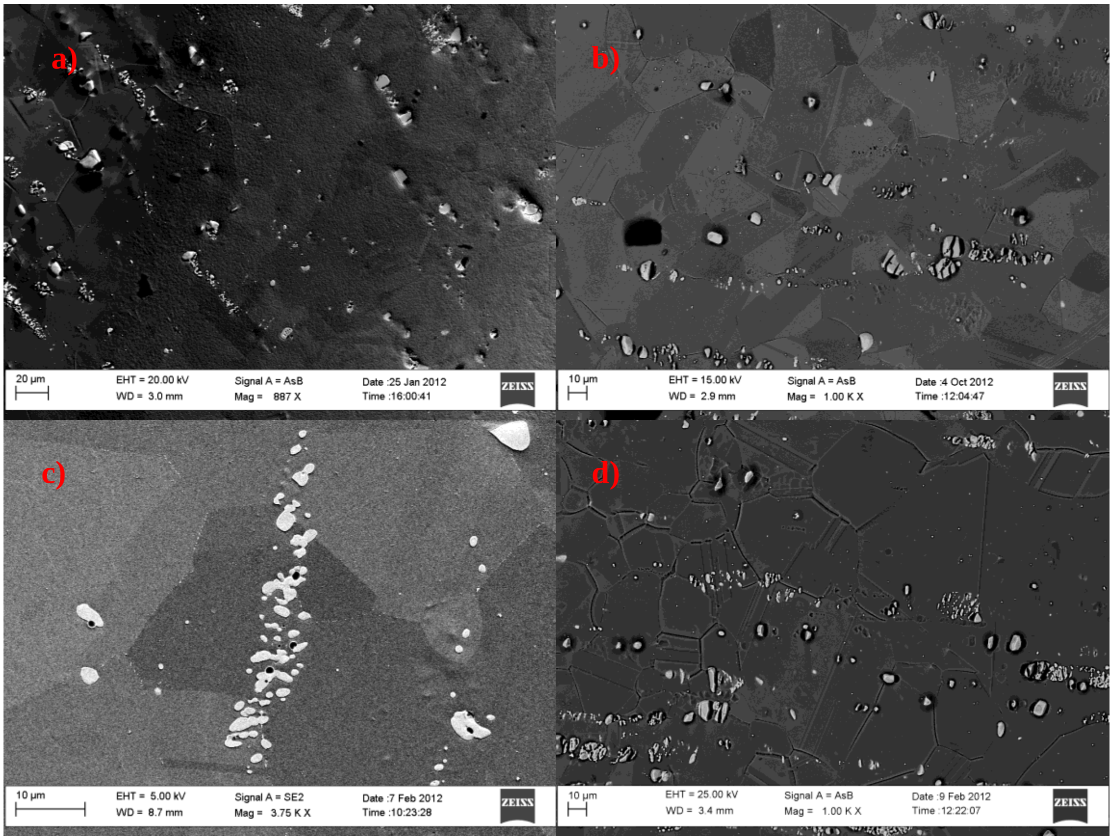

Figure 2.4 Low magnification SEM micrographs of Haynes 230 showing a) the deformed precipitates in the rolling direction b) the high density of annealing twins c) the morphology of the deformed precipitates and d) the equiaxed grains

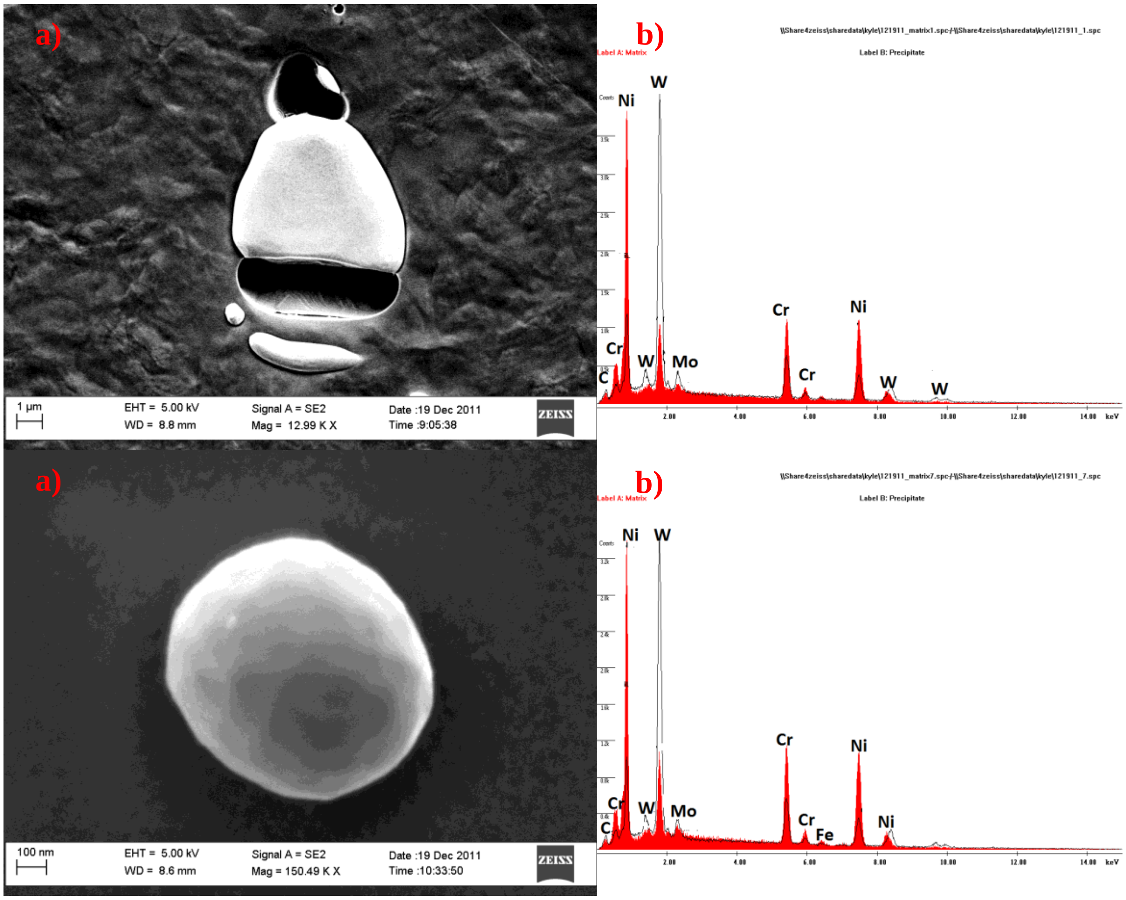

Figure 2.5 W and Mo rich carbide present in Haynes 230 with EDX analysis

Elemental mapping was again performed on Haynes 230, further exposing the composition of the carbides. Figure 2.6 shows these elemental maps which reinforce that the precipitates are rich in tungsten and molybdenum. Tungsten was chosen as the primary alloying element due to its larger atomic size and lower diffusivity in nickel than molybdenum. Tungsten also reduces the stacking fault energy of nickel which in turn reduces the cross slip of dislocations [33].

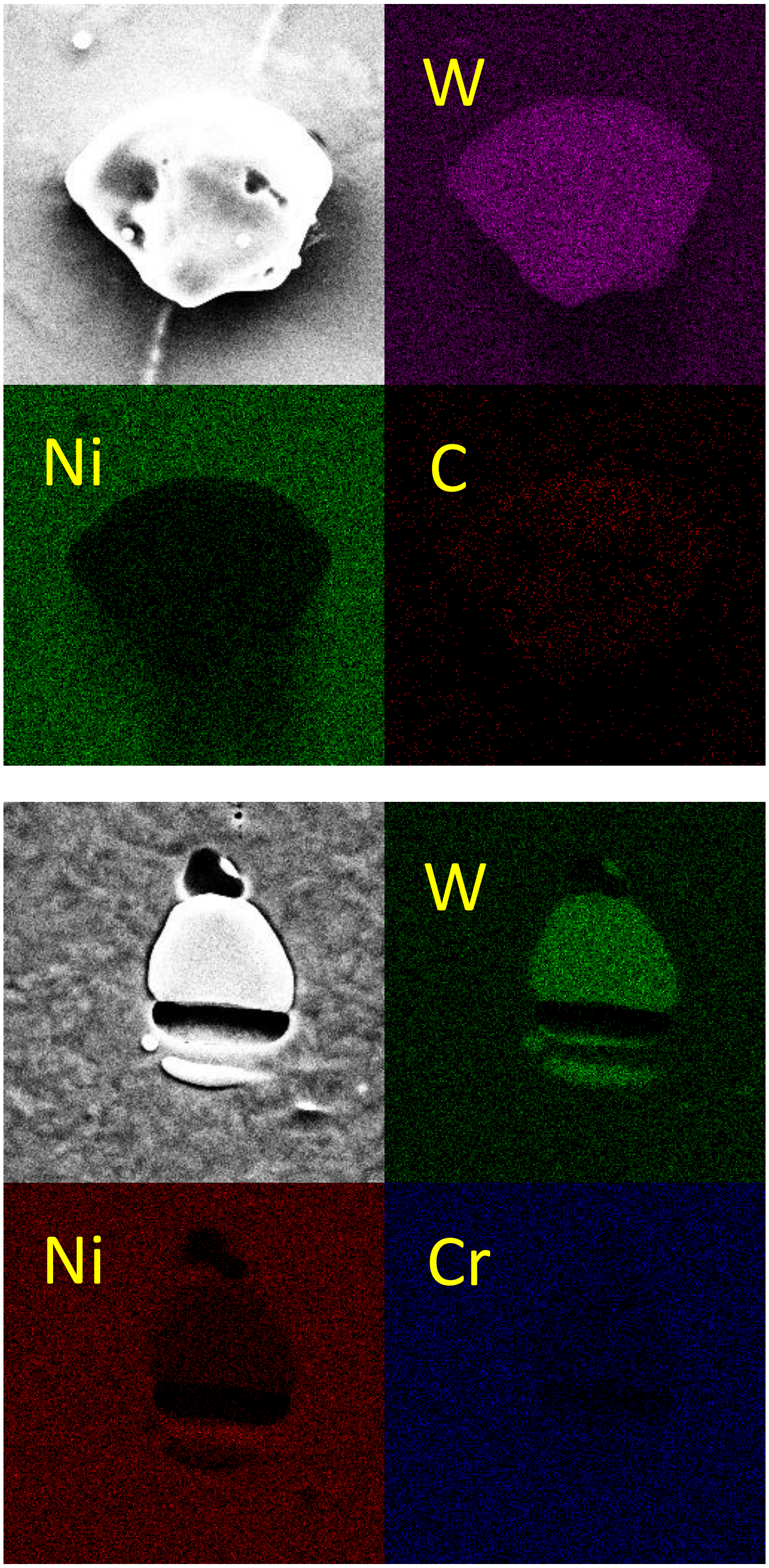

Figure 2.6 Elemental maps of carbide precipitates of Haynes 230

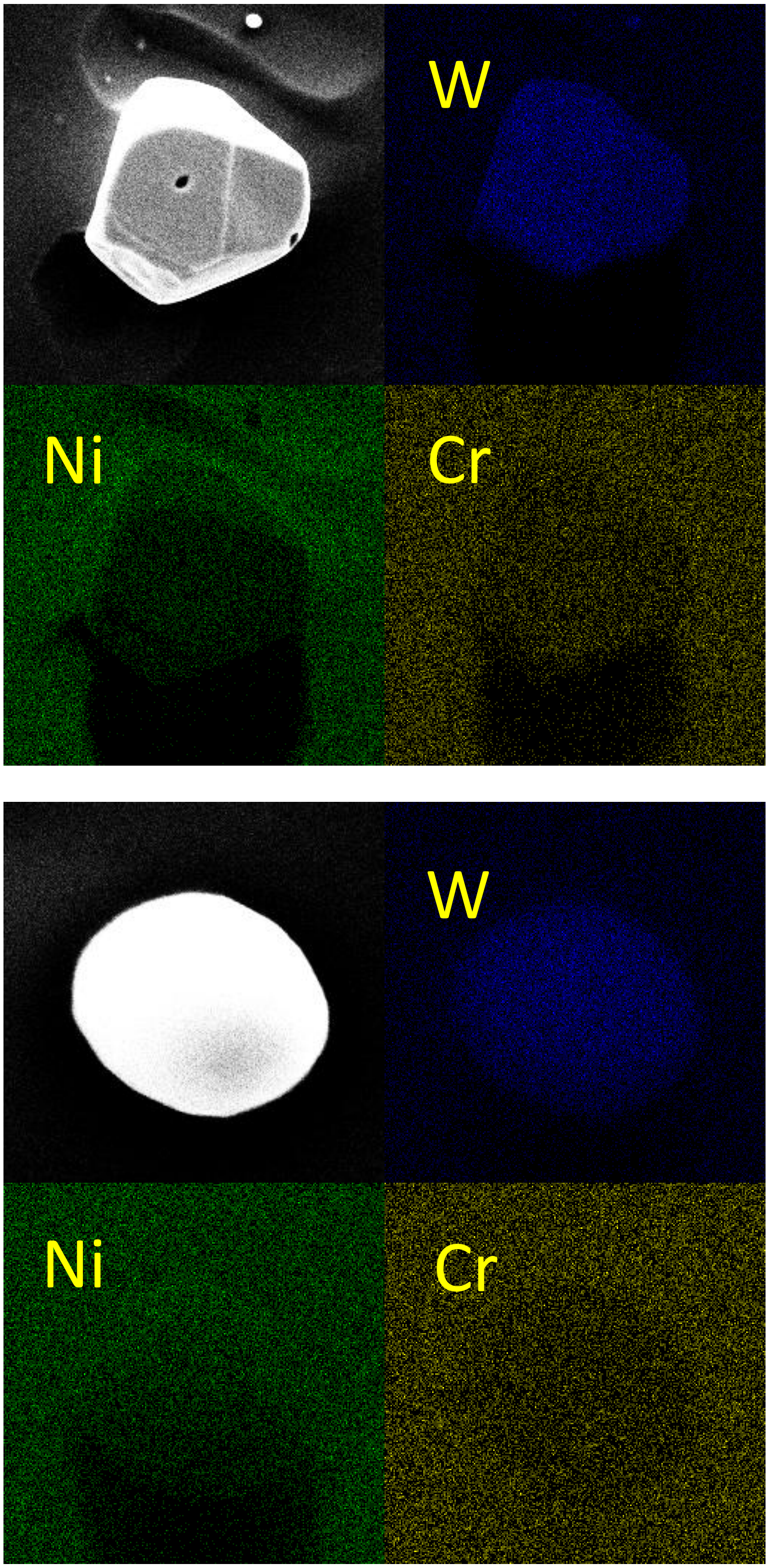

Figure 2.6 Elemental maps of carbide precipitates of Haynes 230

2.2 Tensile Testing

Uniaxial tensile testing was performed on Inconel 617 and Haynes 230 to determine mechanical properties at various temperatures. This section explains the specimen design, the machine setup, and the testing conditions.

2.2.1 Specimen Design

Samples were cut from the Inconel 617 and Haynes 230 sheets by way of wire Electrical Discharge Machining (EDM). The specimens were machined with the dog bone geometry shown in Figure 2.7. The samples had dimensions of 0.02” thickness, 0.25” gage width, and a 1.25” gage length. The total length of the sample measured 4.72”. The geometry is a subsize specimen and is a scaled down version of the standard ASTM pin-loaded tension test specimen [34].

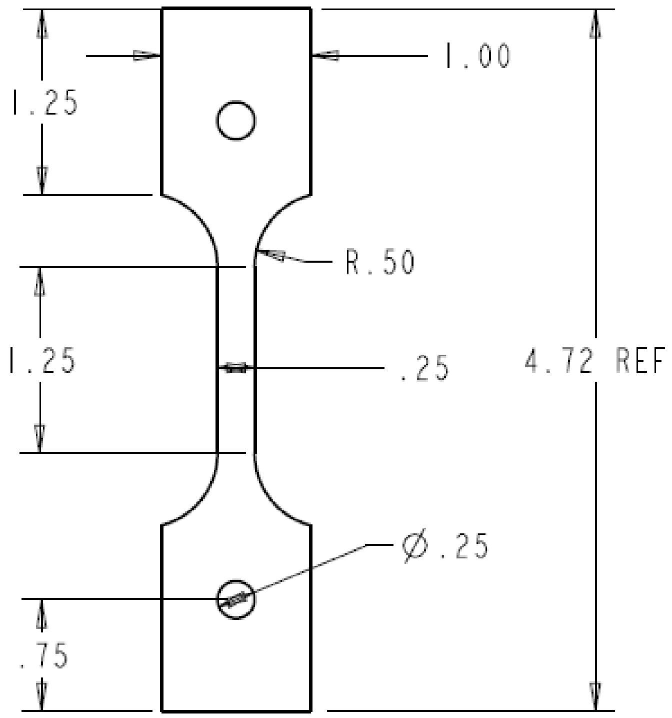

Figure 2.7 Geometry of tensile specimen

2.2.2 Machine Setup

Hot tensile tests were performed by a 5980 Instron® machine with a Materials Research Furnace® (MRF) which took specimens up to temperatures as high as 950 °C. The Instron® load frame is comprised of a base, two columns, a moving crosshead, and a top plate. A 30 kN load cell is mounted on the crosshead and rotation of a ballscrew drives the crosshead up or down while the guide column provides stability. The specimen is held in place by pin-and-clevis grips with a ¼” pin on either side of the gage length. Strain is registered by an Epsilon strain gage held taut against the specimen by way of cords looped around the opposite side of the specimen. The strain gage uses pointed ceramic tips directly touching the thin edge of the specimen. Instron Bluehill®

software was provided by Instron® which controlled the testing system, ran tests, and analyzed test data to produce results.

The MRF® furnace housed several components necessary to control the hot tensile tests. Water coolant lines are simply connected to the main water inlet valve and run throughout the furnace to remove heat. The controller can be used to adjust pressure and temperature setpoints, monitor process variables, and shut down the furnace. Two thermocouples are placed in the hot zone: the primary thermocouple is located close to the specimen to monitor the temperature of the metal, the secondary thermocouple is located farther from the specimen and automatically shuts down the furnace should the temperature increase beyond the maximum of 980 °C.

2.2.3 Hot Tensile Procedures

Prior to testing, the samples were loaded into the Instron machine and held in place with pin-and-clevis grips. The strain gage was then attached by placing the tips 1” apart along the gage length. To prevent fraying of the cords holding the strain gage in place, two small steel clamps were placed on one side of the specimen. At this point the furnace was sealed shut and a vacuum was pulled to prevent oxidation of the sample. Once a pressure of 0.1 torr had been reached, the furnace was refilled with high purity air.

Both elongation and load were zeroed at this point (assuming that the sample had returned to its original position before the vacuum was pulled). A preload of 20 N was also placed on the sample at this point, and held throughout the heating process in order to prevent a buckling action as the metal parts expanded during heating. The test sample was then heated at a rate of 25 °C/min to the temperature of interest. Upon reaching this temperature the specimen was held for a duration of 30 minutes in order to allow thermal equilibrium between the sample, the grips, and the pulling rods.

Tests were conducted at room temperature, 800 °C, and 950 °C. All tests were strain controlled and held constant at a strain rate of either 10^{-5} s^{-1}, 10^{-4} s^{-1}, or -10^{-3} s^{-1}. These strain rates correspond to an extension rate of 0.000461 mm/s, 0.00461 mm/s, and 0.0461 mm/s, respectively. Strains were relayed from the strain gage and strain rate was controlled by the Bluehill software. Specimens were taken to fracture, after which the Instron machine was cooled by flowing water to room temperature. To determine yield, a 0.2% offset was used and the Ultimate Tensile Strength (UTS) was taken from the maximum stress on the flow curve.

2.2.4 Tensile Test Matrix

A series of tensile tests were run at the temperatures of 25 °C, 600 °C, 800 °C, and 950 °C, at strain rates of 10^{-3} s^{-1}, 10^{-4} s^{-1}, and 10^{-5} s^{-1}. At each test temperature and strain rate, up to three trials were run to provide statistical accuracy as seen in Table 2.2.

Table 2.2 Experimental test matrix

Trial	Temperature (°C)	Strain Rate (s^{-1})	Atmosphere	# I617	# H230
1	25	10^{-3}	Air	2	1
2	25	10^{-4}	Air	2	0
3	25	10^{-5}	Air	1	0
4	300	10^{-3}	HP Air	1	0
5	400	10^{-3}	HP Air	1	0
6	600	10^{-3}	HP Air	2	1
7	600	10^{-4}	HP Air	2	0
8	600	10^{-5}	HP Air	2	0
9	800	10^{-3}	HP Air	3	1
10	800	10^{-4}	HP Air	3	1
11	800	10^{-5}	HP Air	2	1
12	850	10^{-3}	HP Air	1	0
13	900	10^{-3}	HP Air	1	0
14	950	10^{-3}	HP Air	2	1
15	950	10^{-4}	HP Air	2	1
16	950	10^{-5}	HP Air	2	1

2.3 Electron Microscopy

Several electron microscopy techniques, including SEM, EDX, and TEM were used to inspect the microstructure of the as-received material as well as the specimens fractured at high temperature. They were used to inspect precipitate morphology, grain sizes, and grain boundaries. In addition they were used to relate recrystallization mechanisms to microstructural deformation during hot deformation. This section provides an overview of the procedures used for each technique.

2.3.1 Sample Preparation

Sample preparation started by sectioning tensile specimens longitudinally using a low speed diamond saw. The sectioned samples were then mounted on aluminum stubs with the adhesive Crystalbond and ground on silicon carbide paper with a water lubricant to remove burrs and ensure a flat surface. Initial grinding started with 400 grit paper, followed by 600 grit, 800 grit, and finally 1200 grit paper. Samples were ground to a thickness of roughly 100 µm.

Following the polishing, 3 mm foils were punched and subsequently electropolished in a solution of 5% $HClO_4$ and 95% methanol. Foils for electron microscopy were prepared in a twin-jet Struers electropolisher at -40 °C using a potential of 18 V d.c. and a current of 116 mA. After electropolishing samples were placed in a series of cold baths: methanol, ethanol, and a final methanol bath before drying on a paper towel.

2.3.2 Scanning Electron Microscopy (SEM)

A Zeiss Ultra plus Field Emission SEM (FESEM) was used to obtain high resolution images of the microstructures of the as-received and deformed specimens of both alloys. The high resolution allowed for close inspection of grain morphology, precipitation location, precipitation morphology, annealing twins, and other features which contribute to recrystallization mechanisms. The optimum imaging voltage was determined to be 5 kV and allowed for clear images of particles as small as 100 nm. Backscattered electrons were also used to gain clearer images of grain boundaries and these were operated at 20 kV. The working distance for all samples was held constant at 3 mm.

2.3.3 Energy-Dispersive X-Ray Spectroscopy (EDX)

In order to compare the composition of precipitates to the surrounding matrix, EDX spectra and maps were created. Imaging conditions were changed to an operating voltage of 15 kV to obtain a higher number of counted electrons. EDX provided information on the chemical evolution of precipitates present in the nickel-rich matrix. The software identified peaks of high intensity elements which gave a simple composition of the alloy. Also, elemental maps could be generated which show a visual representation of areas rich in certain elements (precipitates compared to matrix).

2.3.4 Transmission Electron Microscopy (TEM)

All TEM experiments were conducted at Argonne National Lab (ANL) using an Intermediate Voltage Hitachi H-9000NAR TEM. Higher resolution than the SEM showed grain boundary serrations, carbide diffusion, and most importantly dislocation motion. The TEM could also more clearly identify grain boundaries at higher temperatures. In-situ tensile tests at elevated temperatures could be viewed in order to see dislocation motion during deformation. An illustration of TEM can be seen in Figure 2.8.

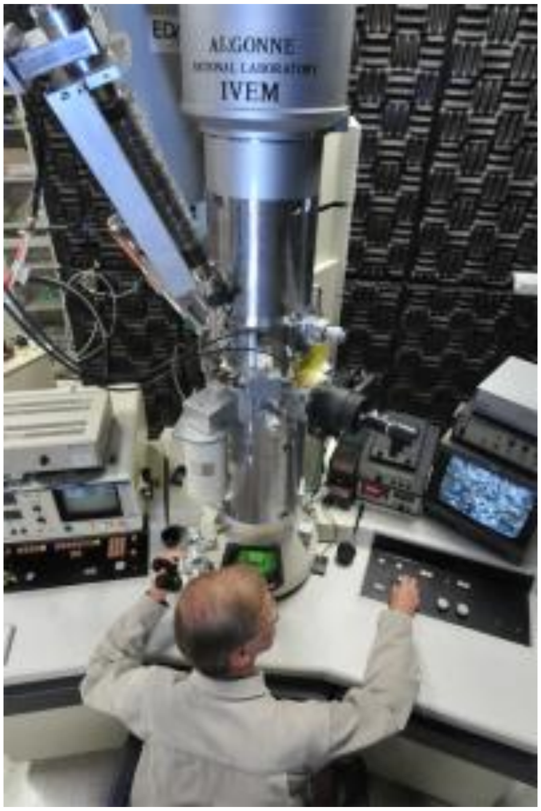

Figure 2.8 TEM setup at Argonne National Laboratory

2.4 X-Ray Diffraction (XRD)

In order to determine the stoichiometric composition of the carbides present in the as-received and deformed material, XRD analysis was employed. XRD was performed on both the bulk material as well as precipitates extracted by way of dissolution. To perform the extraction 2-4 g samples of Haynes® 230 and Inconel 617 were disassociated in the highly acidic solution, aqua regia, in order to separate the carbides from the matrix. The solution was a 3:1 mixture of 15 M nitric acid added to 12 M hydrochloric acid [35]. The complete dissolution of the metallic matrix took roughly three days. Once the matrix had dissolved in the solution, the solution was neutralized by slowly pouring it into sodium bicarbonate and then further diluting it with deionized water. The precipitates were left at the bottom of the solution and water was slowly added to dilute the remaining acid. After this the remaining solution was filtered with 0.02 μm filter paper and the particles were left to dry.

At this point XRD analysis was carried out on the remaining particles to observe carbide evolution and to determine the metals present in the precipitates. XRD was carried out by focusing an x-ray beam on the precipitates and observing the scattering angles of the diffracted beam. The scattering angle can be related to the distance between planes by Bragg's Law:

$$n\lambda = 2dsin\theta \tag{2.1}$$

where n is an integer, λ is the wavelength of the incident x-ray beam, d is the atomic distance between the layers in the crystal, and θ is the scattering angle. The distance between the atomic planes in the crystal is then used to identify the elements which make up each precipitate.

2.6 Grain Size Characterization

The size of undeformed grains as well as recrystallized grains was determined by using ImageJ software. Low magnification SEM images of the grains were outlined in dark ink and then scanned into the software. The software determined the area of each grain, from which an equivalent radius could be derived to calculate the average grain size. The average grain size was measured using three different areas of the same magnification in order to minimize statistical error.

CHAPTER 3

Results

This chapter presents the experimental results obtained from tensile testing and the subsequent microstructural analysis. This chapter is divided into two sections: hot tensile flow behavior and microstructural examination. The results are presented first allowing for a lead-in to the discussion in the following chapter.

3.1 Hot Tensile Flow Behavior

Tensile tests were performed on Inconel 617 and Haynes 230 alloys at several different temperatures and strain rates. The resulting mechanical properties, stress-strain behavior and microstructure are examined in this section.

3.1.1 Mechanical Properties

The effects of temperature exposure on the tensile properties of Inconel 617 and Haynes 230 have been investigated by carrying out tensile tests at room temperature, 300 °C, 400 °C, 600 °C, 800 °C, and 950 °C and comparing those with tensile tests conducted at room temperature. Details about the procedure and the specimens were described in sections 2.2.1 and 2.2.3. Samples were tested at different temperatures, at different strain rates, and in different environments in order to examine the effect that each variable had on the mechanical properties. Table 3.1 gives average values of the results of the 0.2% Yield Strength (YS), the Ultimate Tensile Strength (UTS), and the total elongation at fracture.

Table 3.1 Testing Matrix of Inconel 617 and Haynes 230

Material	Temperature (°C)	Strain Rate (s^{-1})	Atmosphere	YS (MPa)	UTS (MPa)	% Elongation	# Samples
Inconel 617	25	10^{-3}	Air	426.5	857.4	52.1	2
Inconel 617	25	10^{-4}	Air	425.1	860.3	61.9	2
Inconel 617	25	10^{-5}	Air	412.4	850.1	64.0	1
Inconel 617	300	10^{-3}	HP Air	318.8	741.6	58.46	1
Inconel 617	400	10^{-3}	HP Air	294.2	734.9	54.28	1
Inconel 617	600	10^{-3}	HP Air	270.9	696.1	54.7	2
Inconel 617	600	10^{-4}	HP Air	279.0	758.6	62.7	2
Inconel 617	600	10^{-5}	HP Air	297.5	739.6	51.7	2
Inconel 617	800	10^{-3}	HP Air	277.9	387.7	72.4	3
Inconel 617	800	10^{-4}	HP Air	301.3	301.3	71.1	3
Inconel 617	800	10^{-5}	HP Air	198.4	201.8	64.4	2
Inconel 617	950	10^{-3}	HP Air	181.1	182.7	44.5	2
Inconel 617	950	10^{-4}	HP Air	111.4	112.9	34.6	2
Inconel 617	950	10^{-5}	HP Air	72.6	75.9	25.3	2
Haynes230	25	10^{-3}	Air	370.4	823.9	55.1	1
Haynes230	600	10^{-3}	HP Air	262.1	682.1	53.0	1
Haynes230	800	10^{-3}	HP Air	275.2	405.4	44.1	1
Haynes230	800	10^{-4}	HP Air	302.5	303.9	34.5	1
Haynes230	800	10^{-5}	HP Air	187.6	191.8	29.9	1
Haynes230	950	10^{-3}	HP Air	177.6	179.7	33.3	1
Haynes230	950	10^{-4}	HP Air	116.4	120.8	24.3	1
Haynes230	950	10^{-5}	HP Air	76.0	79.9	20.7	1

3.1.1.1 Inconel 617

The results indicate that both temperature and strain rate play an important role in the mechanical behavior of these alloys.

a) Strain Rate Dependence at Each Temperature:

At room temperature the YS and UTS stay nearly constant (430 MPa and 850 MPa respectively) at each strain rate. The elongation increases with a decrease in strain rate. Samples fracture at about 50% strain at a strain rate of 10^{-3} s^{-1}, but the figure increases to about 64% at a strain rate of 10^{-5} s^{-1}.

Strain rate plays a larger factor at 600 °C. Yield strength increases roughly 11% from 270 MPa at a strain rate of 10^{-3} s^{-1} to 300 MPa at a strain rate of 10^{-5} s^{-1}. The UTS has a maximum of 760 MPa at a strain rate of 10^{-4} s^{-1} and decreases to 735 MPa at a strain rate of 10^{-5} s^{-1} as seen in Figure 3.1. Significant strain hardening takes place at both room temperature and 600 °C. The YS is reached quickly and dislocations continue to build up, acting as obstacles to further dislocation movement. The elongation also reaches a peak of 64% at a strain rate of 10^{-4} s^{-1}. At strain rates of 10^{-3} s^{-1} and 10^{-5} s^{-1}, elongation at fracture only reaches about 50%.

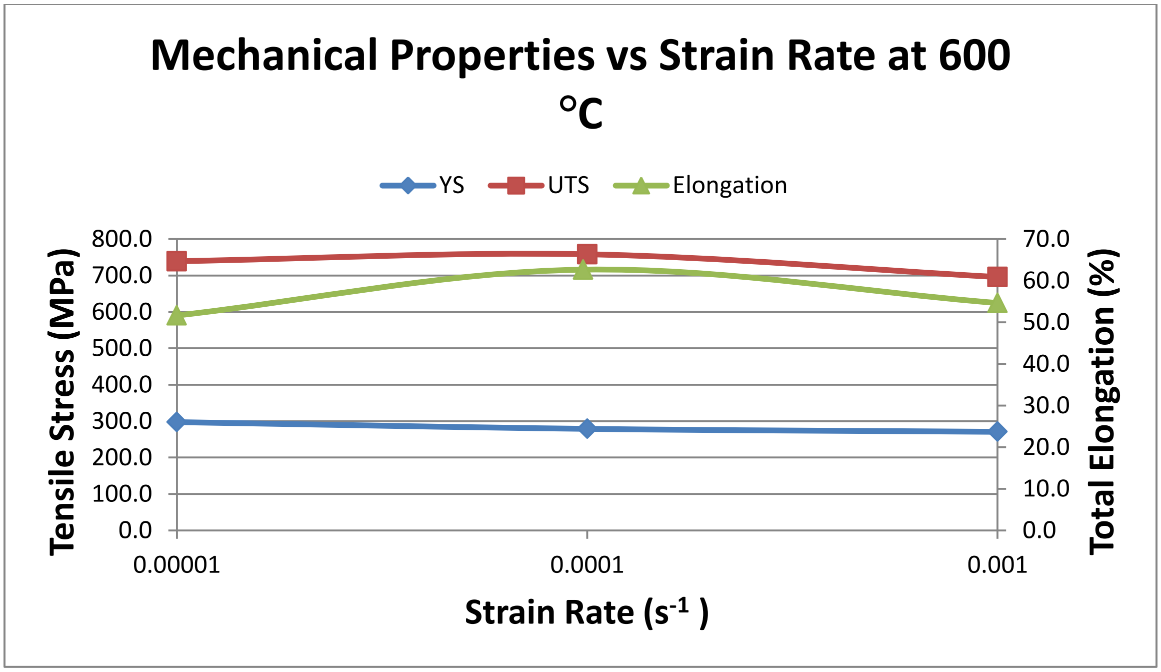

Figure 3.1 Mechanical properties of Inconel 617 at 600 °C

At 800 °C the mechanical properties have a marked difference for each different strain rate. Although the strain rate of 10^{-4} s^{-1} has slightly higher yield strength than the sample tested at strain rate of 10^{-3} s^{-1}, the latter sample experiences significant strain hardening upon reaching yield. The sample tested at a faster strain rate has a UTS over 90 MPa higher than the sample tested at a strain rate of 10^{-4} s^{-1}. Meanwhile the sample tested at a strain rate of 10^{-5} s^{-1} experiences minimum YS, UTS, and final elongation shown in Figure 3.2. The values for YS and UTS at this speed are 198 MPa and 201 MPa, respectively, about 100 MPa less than the sample tested at a strain rate of 10^{-4} s^{-1}.

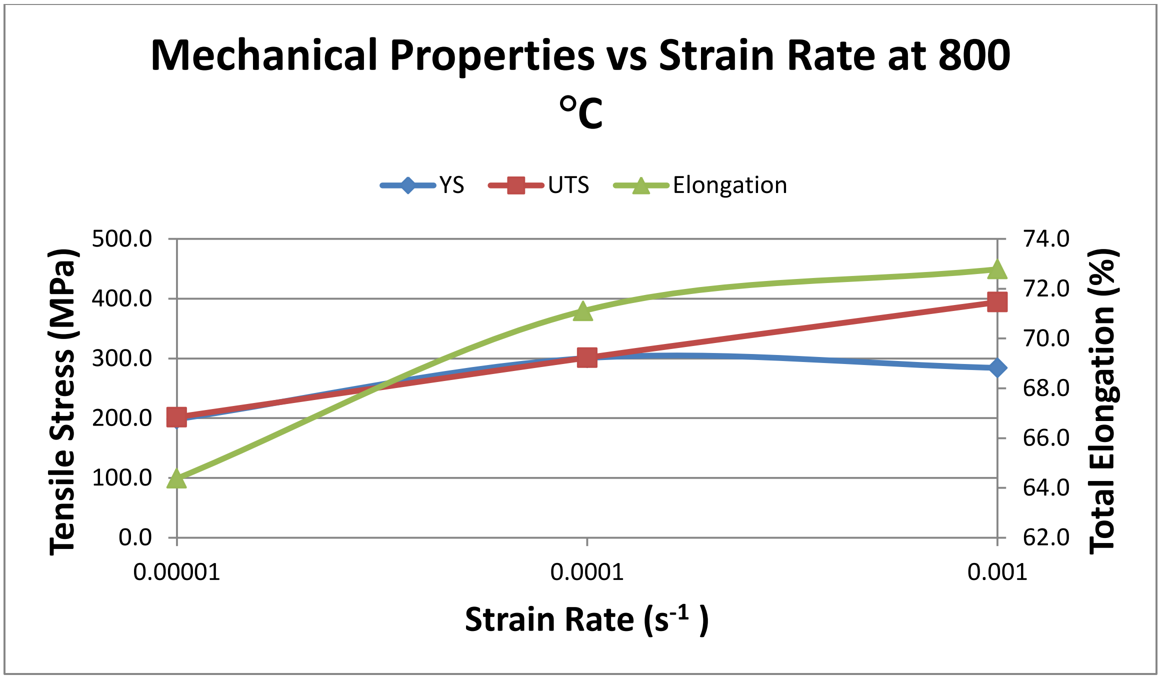

Figure 3.2 Mechanical properties of Inconel 617 at 800 °C

Finally at 950 °C each mechanical property shows a clear dependence on the strain rate. As seen in Figure 3.3 values for YS, UTS, and elongation all decrease as the strain rate is slowed. The YS decreases from 181 MPa to 111 MPa to 74 MPa at strain rates of 10^{-3} s^{-1}, 10^{-4} s^{-1}, and 10^{-5} s^{-1}, respectively. UTS decreases from 183 MPa to 113 MPa to 77 MPa. Regardless of strain rate, there is little work hardening, as each sample quickly reaches its UTS and the strength declines quickly from that point. Final elongation takes a steady drop as well, decreasing from 44.5% to 34.5%, and then ultimately dropping to 22.6% at the slowest strain rate.

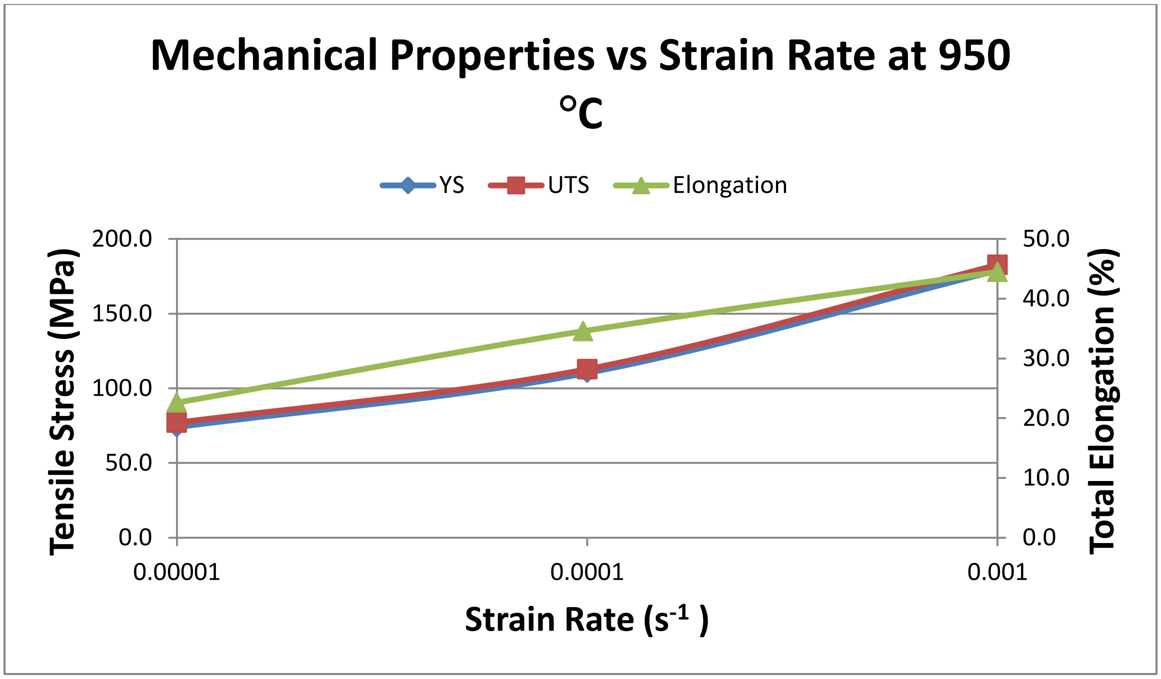

Figure 3.3 Mechanical properties of Inconel 617 at 950 °C

b) Temperature Dependence at Each Strain Rate:

Some interesting observations can be made about the mechanical properties' dependence on temperature. Yield strength shows a gradual decrease from its maximum value at room temperature to its minimum value at 950 °C. However, at strain rates 10^{-3} s^{-1} and 10^{-4} s^{-1}, there is a slight increase in YS from 600 °C to 800 °C. This is a phenomenon known as yield strength anomaly (YSA) and will be discussed in subsequent chapters. YS increases about 5% and 8% for strain rates of 10^{-3} s^{-1} and 10^{-4} s^{-1}, respectively. At a strain rate of 10^{-5} s^{-1}, this same trend does not hold true as seen in Figure 3.4. The trend lines below are simply guides but most likely do not reflect the true behavior at strain rates of 10^{-4} and 10^{-5} s^{-1} in the temperature range of 300-400 °C because there is not the same inflection point seen at a strain rate of 10^{-3} s^{-1}.

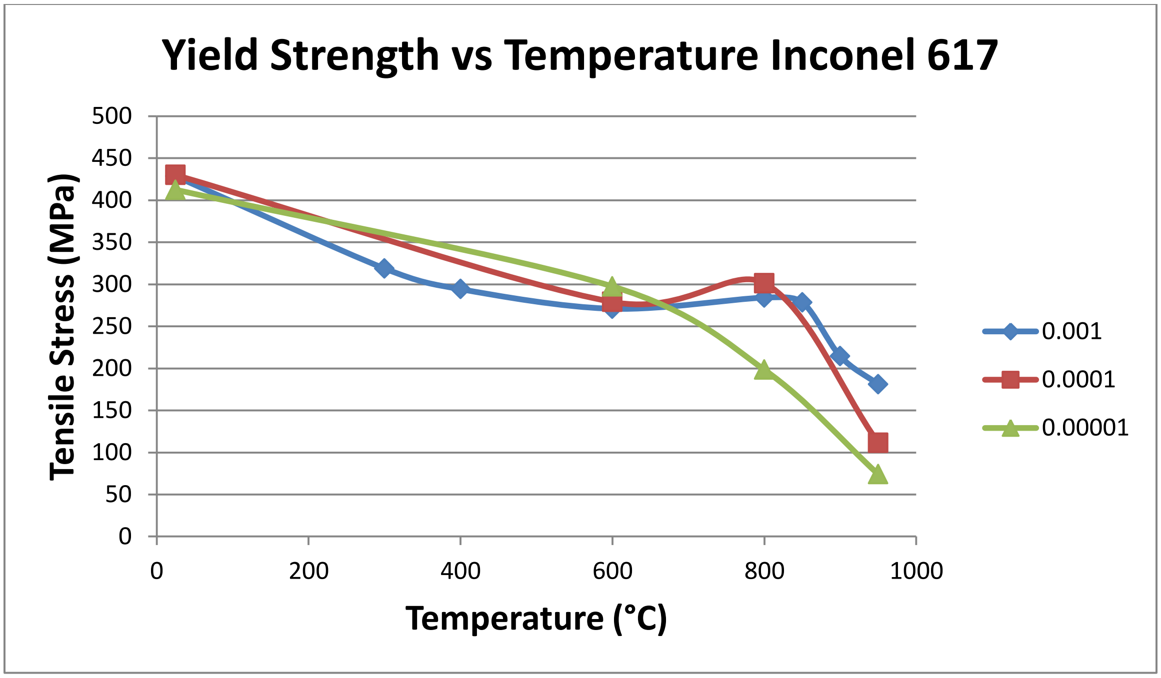

Figure 3.4 Yield Strength Temperature Dependence of Inconel 617

Inconel 617 holds its strength very well as temperature increases. As seen in Figure 3.5 the UTS only decreases a small amount from room temperature to 600 °C. In fact, Inconel only loses about 14% of its strength in this temperature range. At higher temperatures the UTS drops off quickly, losing nearly 65% its strength by the time it reaches 800 °C.

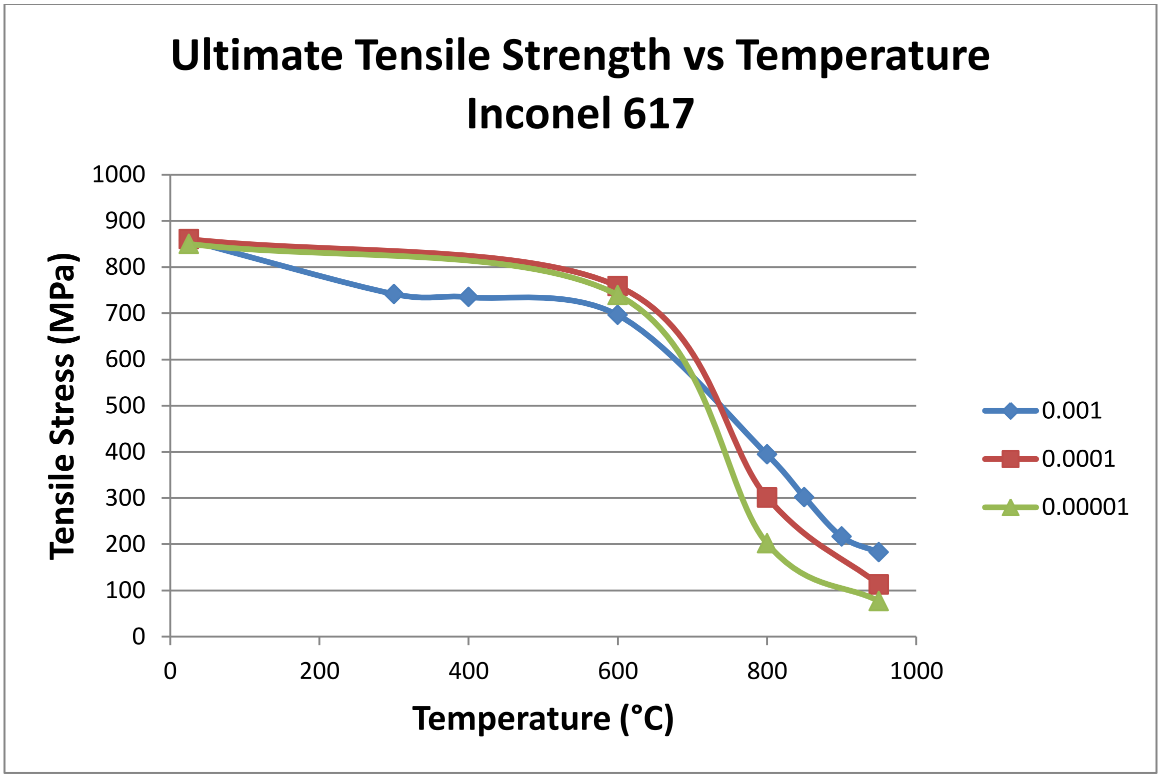

Figure 3.5 Ultimate Tensile Strength of Inconel 617 at various temperatures

At a strain rate of 10^{-3} s^{-1}, the mechanical properties of Inconel 617 are seen in Figure 3.6. There is a slight increase in YS from 600 to 800 °C. Also, there is a plateau in UTS from 300 to 400 °C. Eventually the YS and UTS values unite at about 850 °C. Total elongation also shows a large increase from 600 to 800 °C, followed by a severe decrease at higher temperatures. At each strain rate there is an initial peak similar to that seen at 800 °C. At 10^{-3} s^{-1}, it is a single peak followed by a smooth plastic curve which is an indication of grain refinement. However at strain rates of 10^{-4} and 10^{-5} s^{-1}, the initial peak is followed by successive oscillations which signal recrystallization and grain coarsening.

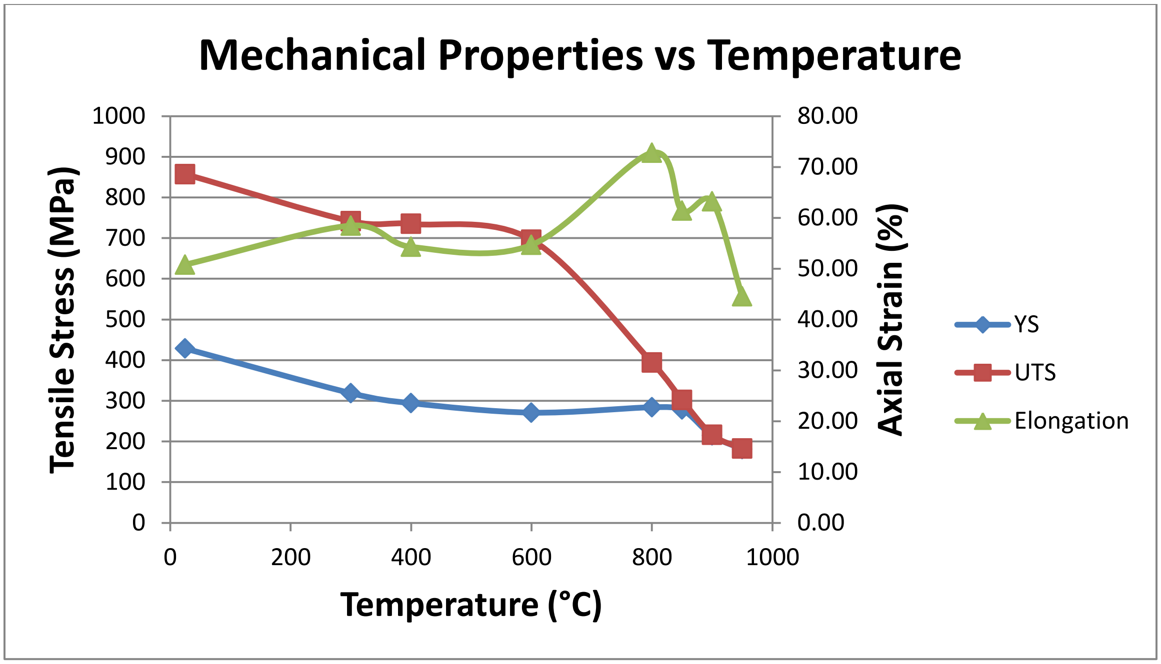

Figure 3.6 Mechanical properties of Inconel 617 as a function of temperature at a strain rate of 10^{-3} s^{-1}

The mechanical properties of this study compare pretty similarly to those provided by the manufacturer, Special Metals. Tensile properties at high temperatures of solution annealed, cold-rolled rods are shown in Figure 3.7. The test specimens were from rod of 0.50-in (13-mm) or 0.62-in (16-mm) diameter. The tests were performed in the transverse direction on sheet of 0.187-in. (4.75-mm) thickness [36]. Much like our study there is a peak in YS around 800 °C, there is a plateau in UTS from 300-600 °C, and the elongation shows a dip in the intermediate temperatures before reaching its peak at temperatures around 800-900 °C. Due to the similarities in results it can be assumed that these tests were conducted at a strain rate of roughly 10^{-3} s^{-1}.

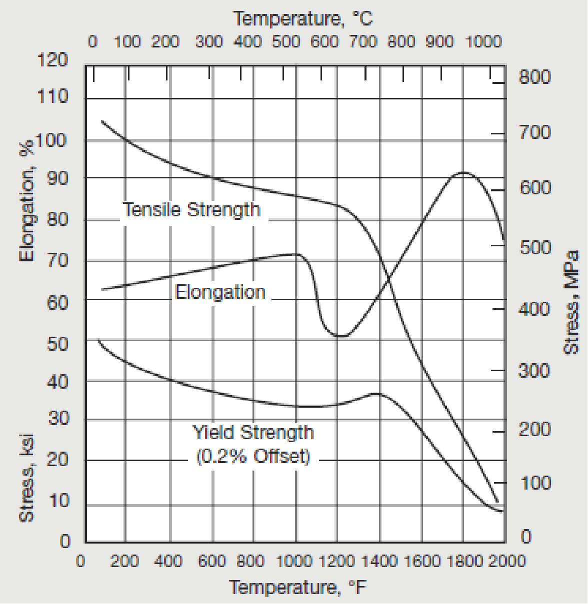

Figure 3.7 Mechanical Properties of Inconel 617 provided by Special Metals

c) Curve Behavior:

The stress-strain curve behavior also experiences marked differences based on temperature and strain rate. As stated before mechanical properties are largely affected by temperature and strain rate; but the stress-strain curve between the YS, the UTS, and the fracture point offers significant insight to the behavior of the alloys. Often, the stress-strain curve behavior can be even more telling about the underlying mechanisms than the mechanical properties.

First, we will examine the effect that strain rate has on Inconel 617 at 600 °C as shown in Figure 3.8. Mentioned in the previous section, the biggest difference in these curves is the point of fracture. Samples strained at a rate of 10^{-4} s^{-1} had a longer elongation than those strained at 10^{-3} s^{-1} and 10^{-5} s^{-1}. Another significant observation that can be made in these curves is the large amount of oscillations in the plastic region. The next section will thoroughly cover these oscillations seen at different temperatures.

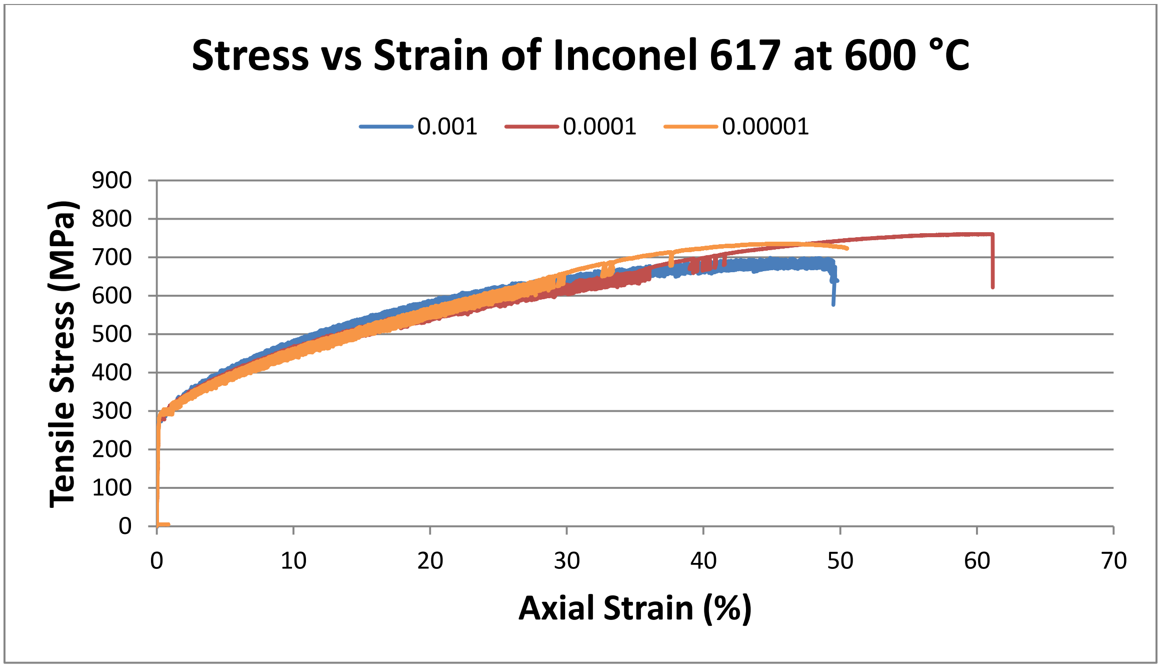

Figure 3.8 Stress-strain curves of Inconel 617 at 600 °C

At 800 °C, strain rate plays a more important role in the curve behavior of Inconel 617. As can be seen in Figure 3.9, each strain rate has a unique stress-strain curve. At a strain rate of 10^{-3} s^{-1} there is significant strain hardening once yield has been reached. Accompanying the strain hardening there are also significant oscillations in the curve. Upon reaching UTS at about 4% strain, the curve becomes smooth and gradually the alloys loses strength. The slower strain rates of 10^{-4} s^{-1} and 10^{-5} s^{-1} produce curves with no strain hardening, indicating that a different microstructural mechanism has become dominant in mechanical behavior. The alloy reaches its yield strength and proceeds to slowly lose strength until fracture. The curve at a strain rate of 10^{-5} s^{-1} is similar in appearance to that strained at 10^{-4} s^{-1}. The YS, UTS, and elongation at fracture are all proportionally lower to the samples strained at a faster rate.

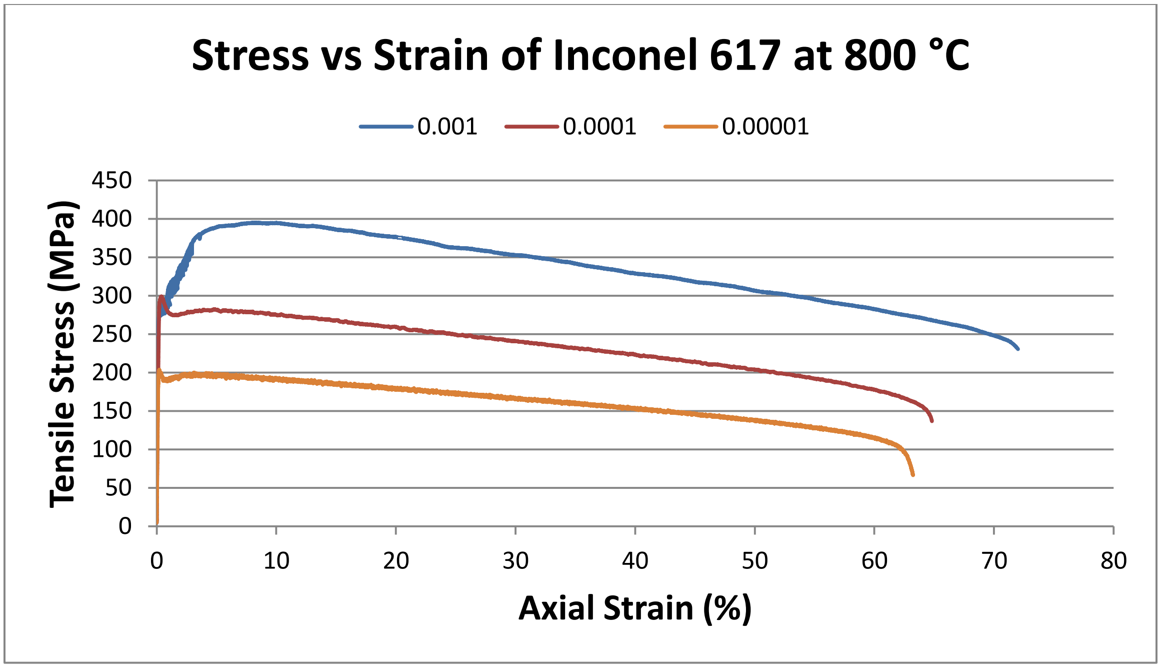

Figure 3.9 Stress strain curves of Inconel 617 at 800 °C

Again at 950 °C the samples strained at 10^{-3} s^{-1} show the most unique curve behavior. Seen in Figure 3.10, the alloy reaches yield, has a quick drop in strength, followed by a gradual, smooth loss in strength until failure. Meanwhile, the samples tested at the slower strain rates do not have the sharp peak seen at yield. Rather, they reach yield and then have small oscillations until reaching fracture. As seen at 800° C, the curve of the slowest strain rate has a similar appearance to that tested at 10^{-4} s^{-1}, but with lower values. YS, UTS, and final elongation are all smaller at a strain rate of 10^{-5} s^{-1} than at a strain rate of 10^{-4} s^{-1}. Also seen at the slower strain rates is a single large peak reached at yield followed by cyclic serrations. Such cyclic behavior is an indication of recrystallization and signals the beginning of grain coarsening [5].

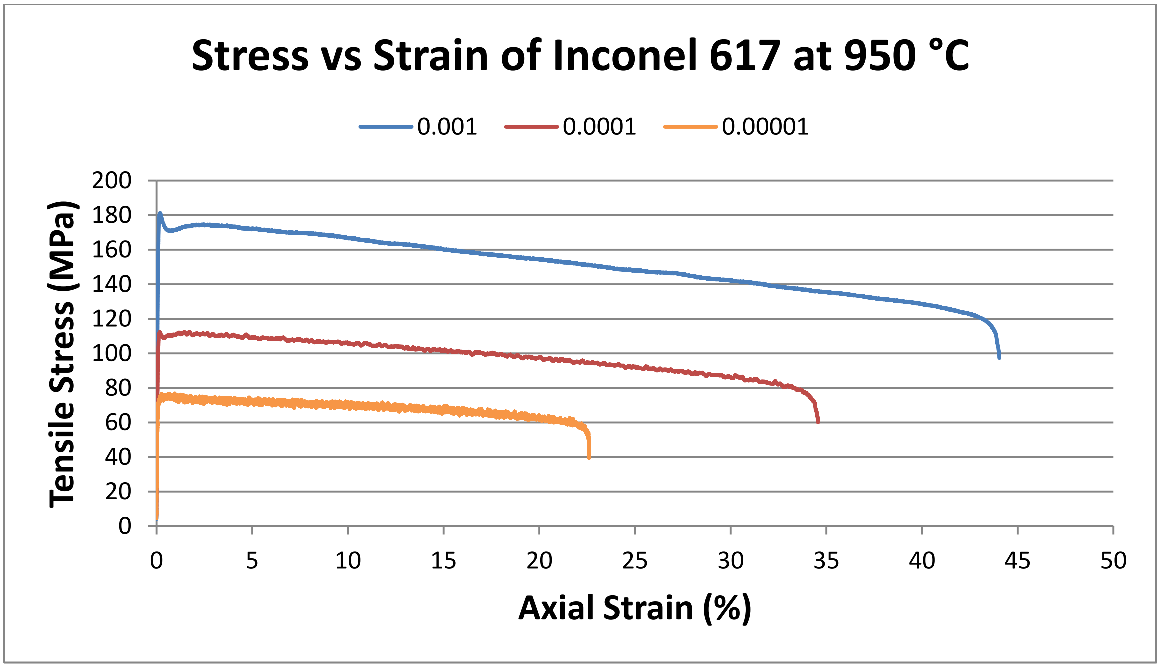

Figure 3.10 Stress-strain curve of Inconel 617 at 950 °C

3.1.1.2 Haynes 230

Haynes 230 shows very similar mechanical properties to Inconel 617 at all temperatures (the full results can be seen in Table 3.1 and in Figure 3.11), but reached failure at a lesser elongation. At 800 °C, YS and UTS values are within 5% of those of Inconel 617. Regardless of strain rate, Haynes 230 follows a similar curve to alloy 617. However, Haynes constantly fractures at a much earlier point than Inconel. At a strain rate of 10^{-3} s^{-1} Haynes reaches a final elongation of only 44%, compared to 72% reached by Inconel. When tested at the slower strain rate of 10^{-4} s^{-1}, the difference is even more pronounced as Haynes fractures at 34% compared to 71% elongation by Inconel. While Haynes showed the same strength seen by Inconel, it fails to match the total elongation at

800 °C. This decline in total elongation is illustrated by the plot of total elongation in Figure 3.12, along with other mechanical properties of Haynes 230.

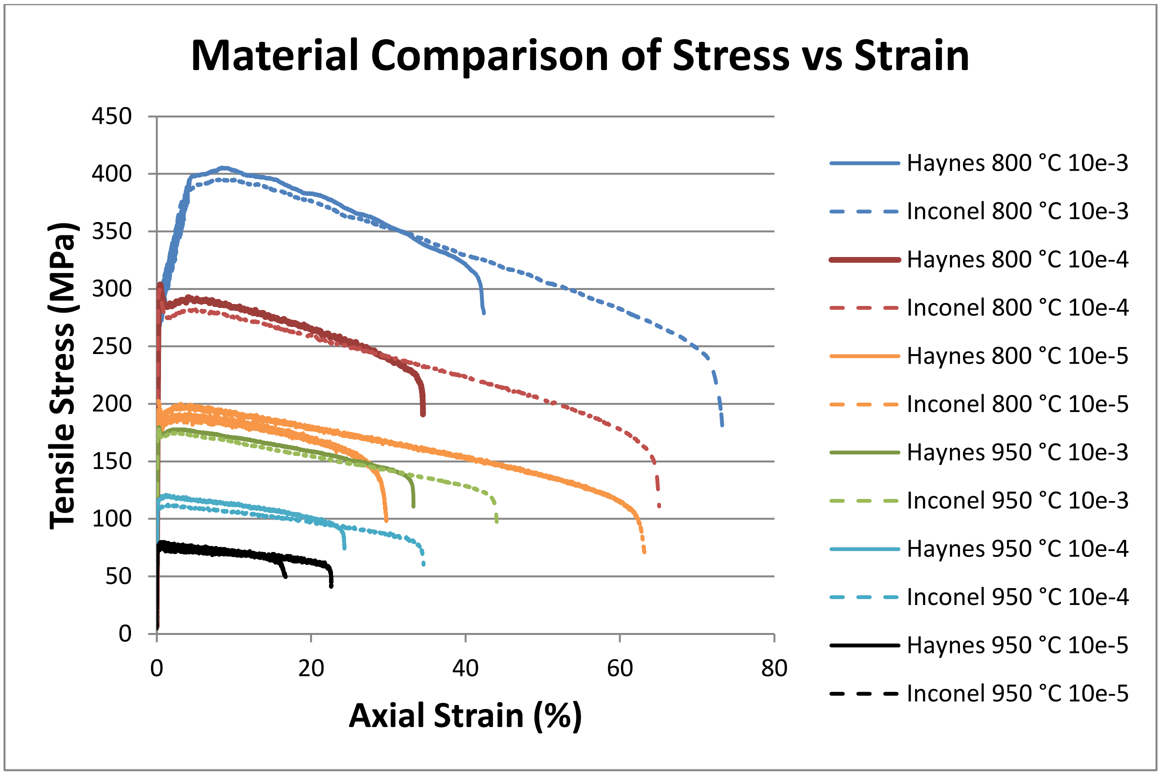

Figure 3.11 Comparison of stress-strain curve between Inconel 617 and Haynes 230

At 950 °C Haynes again shows the same behavior as Inconel. The values of YS and UTS are within percentage points of each other for every strain rate. At a strain rate of 10^{-3} s^{-1} the YS of Haynes and Inconel are 178 MPa and 181 MPa, respectively. The UTS of the two alloys are 180 and 183 MPa. Again the elongation at fracture of Haynes 230 is less than that of Inconel 617, although the difference is not as apparent as at 800 °C. The elongation of 230 only reaches 33%, while 617 hits 44% elongation before fracture.

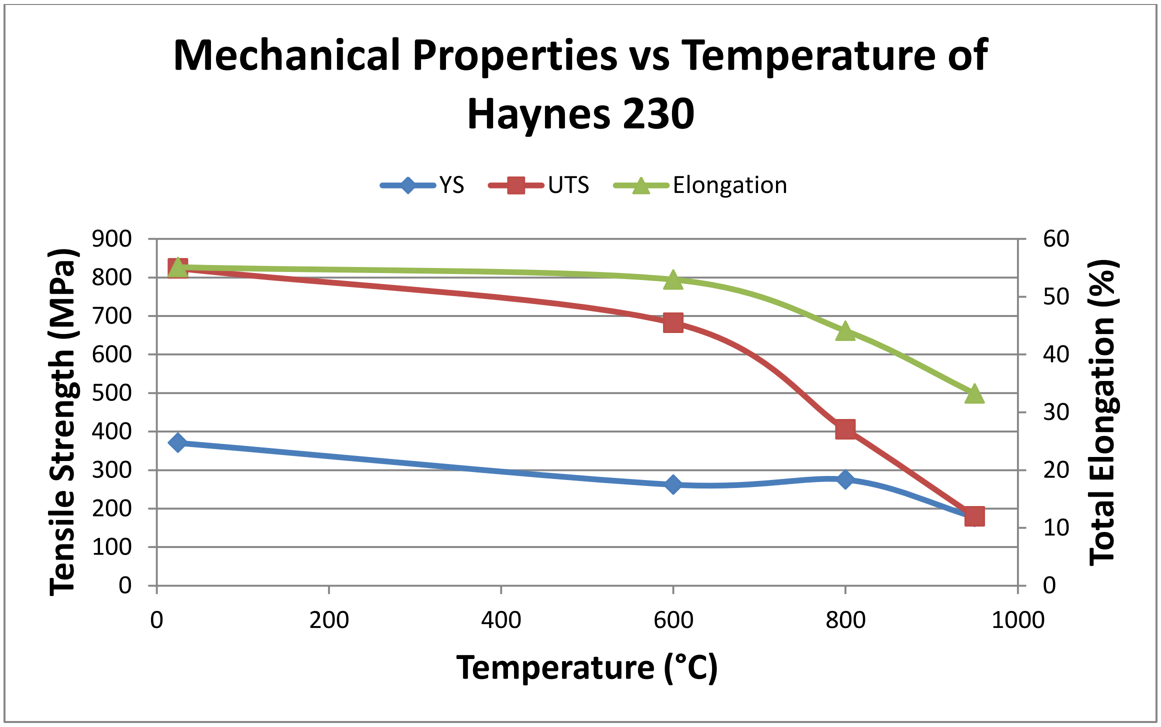

Figure 3.12 Mechanical properties of Haynes 230 as a function of temperature at 10^{-3} s^{-1}

Listed below in Table 3.2 are the mechanical properties given by Haynes International [37]. The gentle decrease in UTS until 760 °C agrees with the results in our study. Haynes International also found a plateau in YS between 540-760 °C, followed by a quick decrease in YS. However, the values in final elongation continually increase from those tested at room temperature all the way up to 1205 °C. Our results showed a general decrease with an increase in temperature.

Table 3.2 Mechanical properties of Haynes 230 provided by Haynes International

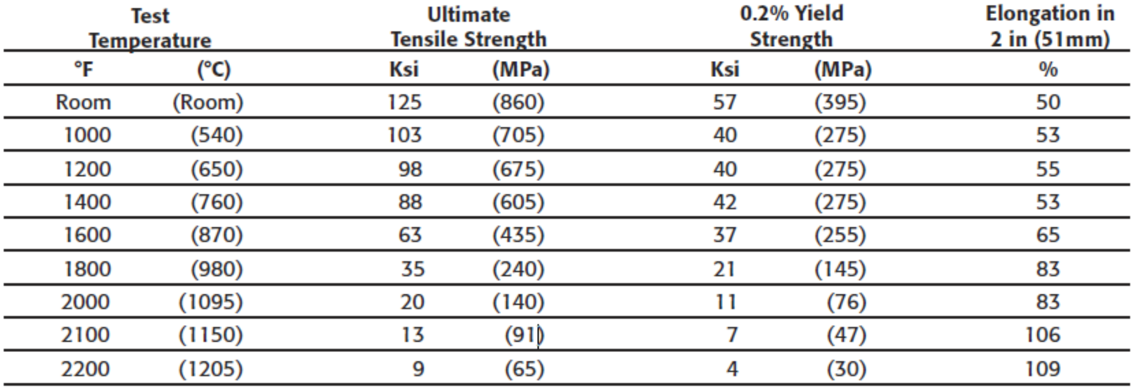

Test Temperature		Ultimate Tensile Strength		0.2% Yield Strength		Elongation in 2 in (51mm)
°F	(°C)	Ksi	(MPa)	Ksi	(MPa)	%
Room	(Room)	125	(860)	57	(395)	50
1000	(540)	103	(705)	40	(275)	53
1200	(650)	98	(675)	40	(275)	55
1400	(760)	88	(605)	42	(275)	53
1600	(870)	63	(435)	37	(255)	65
1800	(980)	35	(240)	21	(145)	83
2000	(1095)	20	(140)	11	(76)	83
2100	(1150)	13	(91)	7	(47)	106
2200	(1205)	9	(65)	4	(30)	109

Haynes 230 exhibits similar stress-strain curve behavior to Inconel 617. At room temperature Haynes exhibits continuous plastic flow. Upon reaching the intermediate temperature of 600 °C, the same large oscillations observed in Inconel are again seen in Haynes. Figure 3.13 shows the curve behavior as the temperature increases for Haynes 230.

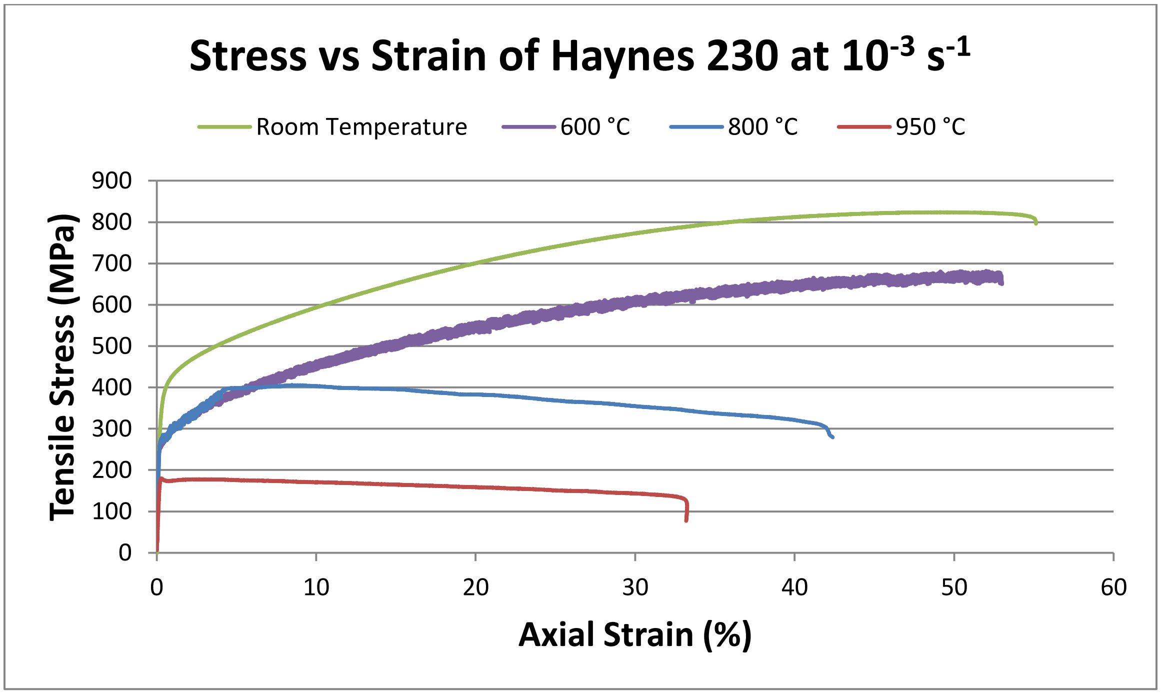

Figure 3.13 Stress-strain curve of Haynes 230 at various temperatures

At 800 °C and a strain rate of 10^{-3} s^{-1}, Haynes undergoes the same strain hardening as Inconel up until about 5% strain. After this point the material softens until fracture. At higher temperatures and slower strain rates Haynes displays the same strain softening phenomena as observed in Inconel. The main effect that strain rate has is to decrease the YS, the UTS, and the final elongation. However, Haynes tends to fracture at a much earlier point than Inconel, as can be seen in Figure 3.11.

3.1.2 Stress Serrations

Several samples tested at different temperatures and strain rates experience stress serrations. These serrations occur over numerous sections of the flow stress curve and differ in magnitude and periodicity. Also worth noting is the shape of the serrations which vary between saw tooth and sinusoidal. It is expected that the deformation mechanisms at play during testing correlate with microstructure evolution, resulting in the serration types observed in the curves. Shown below in Table 3.3 are the amplitude, period, and type of serration at each testing condition that serrations were observed.

Table 3.3 Stress serration information for Inconel 617 at elevated temperatures

Temperature	Strain Rate(s^{-1})	Amplitude (N)	Amplitude (MPa)	Period (s)	Type
600	10^{-3}	95	22	0.25	Sawtooth
600	10^{-4}	97	23	4	Sawtooth
600	10^{-5}	100	23	35	Sawtooth
800	10^{-3}	60	15	0.25	Sawtooth
800	10^{-4}	7	2	35	Sinusoidal
800	10^{-5}	13	3	45	Sinusoidal
950	10^{-3}	N/A	N/A	N/A	N/A
950	10^{-4}	8	2	40	Sinusoidal
950	10^{-5}	13	3	45	Sinusoidal

At 600 °C, every strain rate exhibits serrations upon reaching yield. The serrations remain fairly constant along the length of the curve and fluctuate anywhere between 22 MPa and 25 MPa in amplitude. The period of these serrations is about 0.25 s at a strain rate of 10^{-3} s^{-1}, and increases to roughly 35 s at a strain rate of 10^{-5} s^{-1}. All of the curves also have sharp serrations, rising and falling with discrete peaks as seen in inset of Figure 3.12. For a comparison of the period at different strain rates, all three plots are presented with the same time scale in Figure 3.14. The time scales on these plots are arbitrary but all strain takes place between 10-20%. The biggest difference between the three strain rates is that the oscillations remain steady along the curve at a strain rate of 10^{-3} s^{-1}, but they ultimately disappear after roughly 30% strain for strain rates of 10^{-4} and 10^{-5} s^{-1}. However, the strain rates all show a similarity in size and shape of the flow serrations.

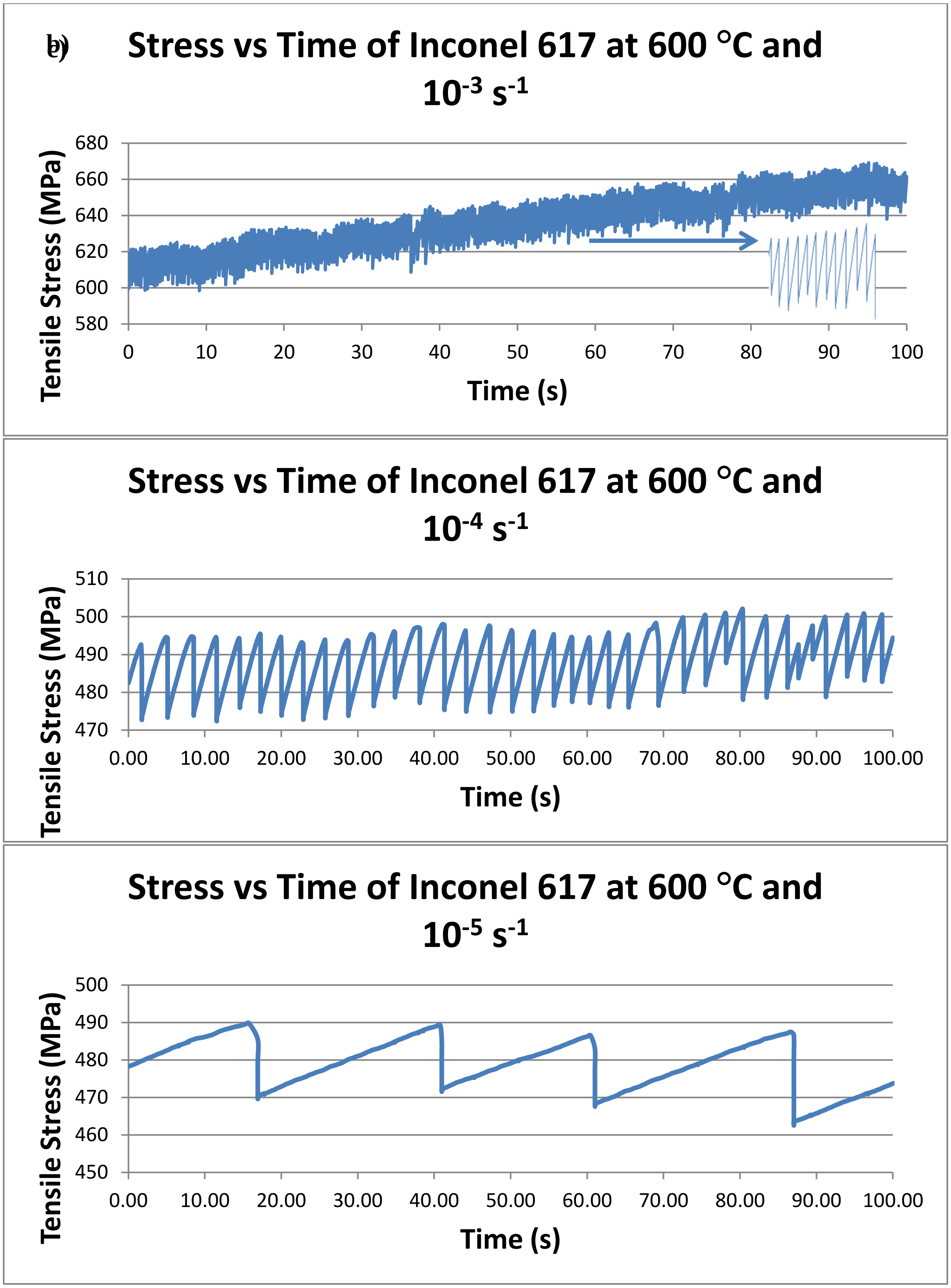

Figure 3.14 Plots of stress vs time of Inconel 617 at 600 °C over an arbitrary 100 second span for strain rates of a) 10^{-3} s^{-1}, b) 10^{-4} s^{-1}, and c) 10^{-5} s^{-1}

At 800 °C, each strain rate has its own unique serration behavior. A strain rate of 10^{-3} s^{-1} produces serrations similar to those seen at 600 °C. Although smaller in magnitude (roughly 15 MPa), they have a similar period of 0.25 s and a shape consistent with that seen in Figure 3.15. However, they only occur over a small portion of the curve from 2-5% strain, in which the sample is experiencing strain hardening, there are no serrations in the softening region. The slower strain rates of 10^{-4} and 10^{-5} s^{-1} produce oscillations with a more sinusoidal wave character. As seen in Figure 3.15 there is also an underlying region of sharp peaks; however, these have been determined to be background noise, with an amplitude less than 0.5 MPa. Again the three different strain rates are presented together in Figure 3.15 to compare the periods. The time scale is arbitrary but oscillations at 10^{-3} s^{-1} occur early between 2-5% while the oscillations shown at slower strain rates of 10^{-4} and 10^{-5} s^{-1} occur in the softening portion of the curve between 10-20% strain. The slower strain rates produce sinusoidal oscillations more consistent with those observed at higher temperatures.

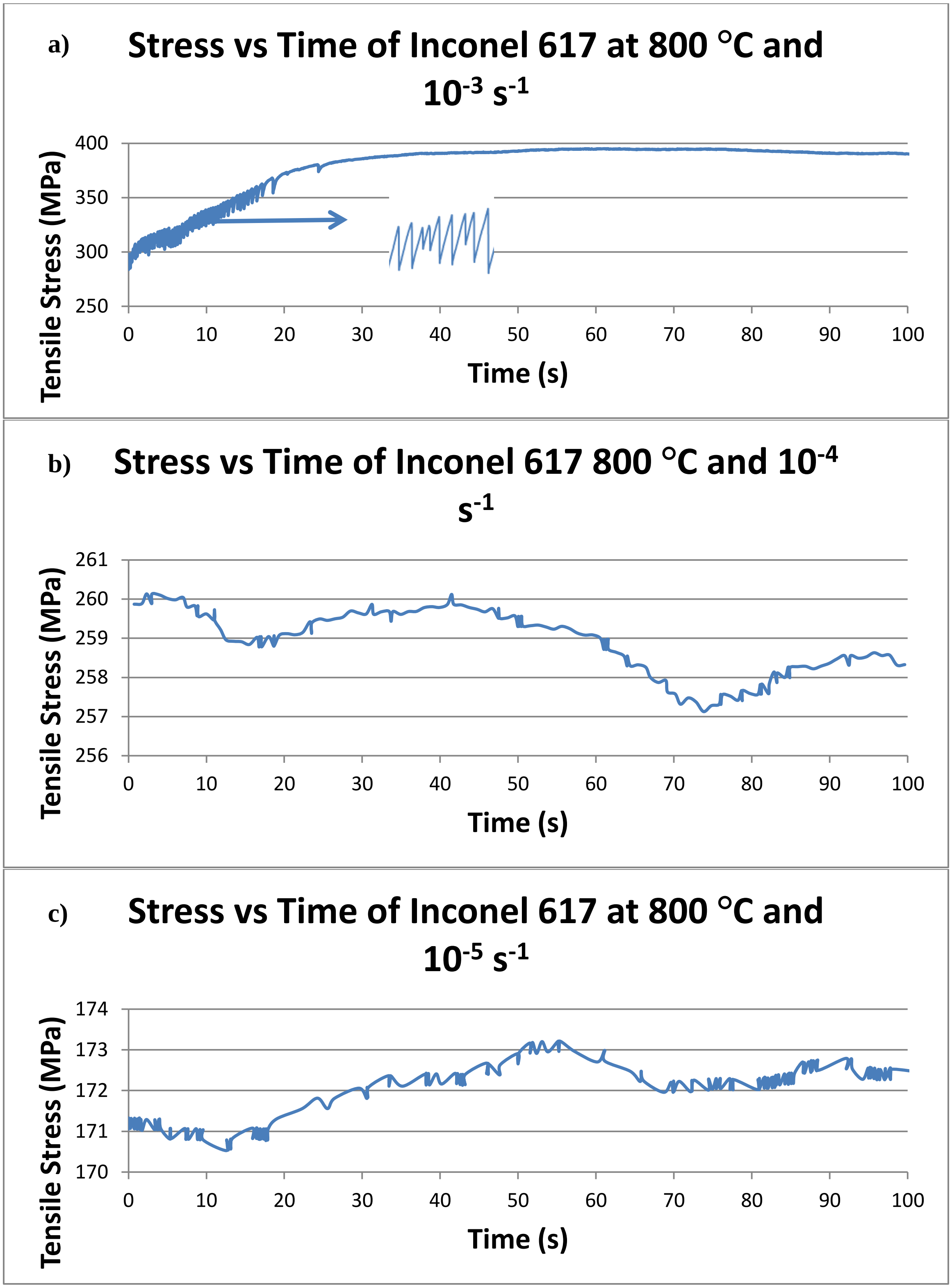

Figure 3.15 Plots of stress vs time of Inconel 617 at 800 °C over an arbitrary 100 second span for strain rates of a) 10^{-3} s^{-1}, b) 10^{-4} s^{-1}, and c) 10^{-5} s^{-1}

At 950 °C, the stress oscillations definitely become less visible. In fact, the fastest strain rate of 10^{-3} s^{-1} doesn't show any oscillations, but they become more apparent at 10^{-4} and 10^{-5} s^{-1}. As seen in Figure, these oscillations have the same shape as those seen in the above Figure 3.15. Again small, sharp oscillations underlie the more dominant sinusoidal oscillations, caused by a similar background noise as seen at 800 °C. Although the amplitude doesn't change between the two strain rates, the oscillations occur much more frequently at 10^{-4} s^{-1}, suggesting that the underlying deformation mechanism is occurring at a greater rate. Lastly, the three strain rates are all shown together in Figure 3.16 to gain perspective on the period of the serrations. Again, the time scale is ambiguous but all of the serrations occur in the softening region between 10-20% strain.

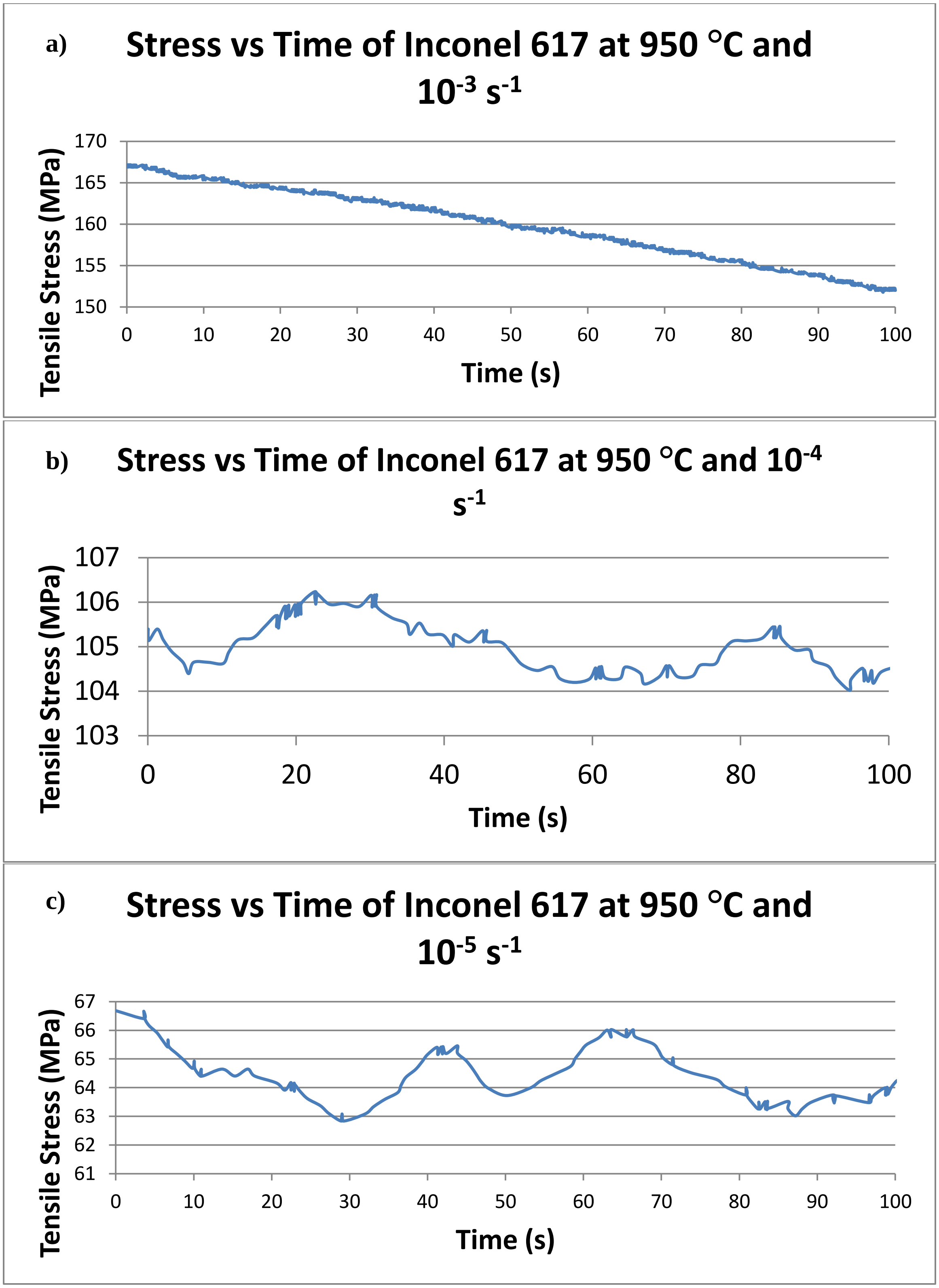

Figure 3.16 Plots of stress vs time of Inconel 617 at 950 °C over an arbitrary 100 second span for strain rates of a) 10^{-3} s^{-1}, b) 10^{-4} s^{-1}, and c) 10^{-5} s^{-1}

3.2 Microstructure Examination

The following section details the microstructural features of Inconel 617 and Haynes 230 after tensile deformation. Microstructural analysis was carried out using SEM, EDX, XRD and TEM. Characteristics investigated include grain size, precipitate redistribution, and dislocation movement.

3.2.1 Inconel 617

Specimens of Inconel 617 were observed under SEM and TEM in order to identify precipitates, grain boundaries, and grain morphology. Samples deformed at temperatures of 600 °C, 800 °C and 950 °C and strain rates of 10^{-3} and 10^{-5} s^{-1} were examined, and each temperature and strain rate possessed a unique microstructure. As mentioned in Chapter 2, three mm discs were punched at the area of fracture to ensure that all microstructure observations are as near to the fractured region as possible.

a) 600 °C/10^{-3} s^{-1}

The grain size of those samples tested at 600 °C remained largely undisturbed. As seen in Figure 3.17 the grains near the fracture area exhibit slight deformation along the tensile axis but not enough to cause any change in the grain size. Also noticeable in these SEM images is the presence of the M_6C carbides, which are still littered throughout the surface. Further evidence of these large carbides will be seen below in TEM micrographs.

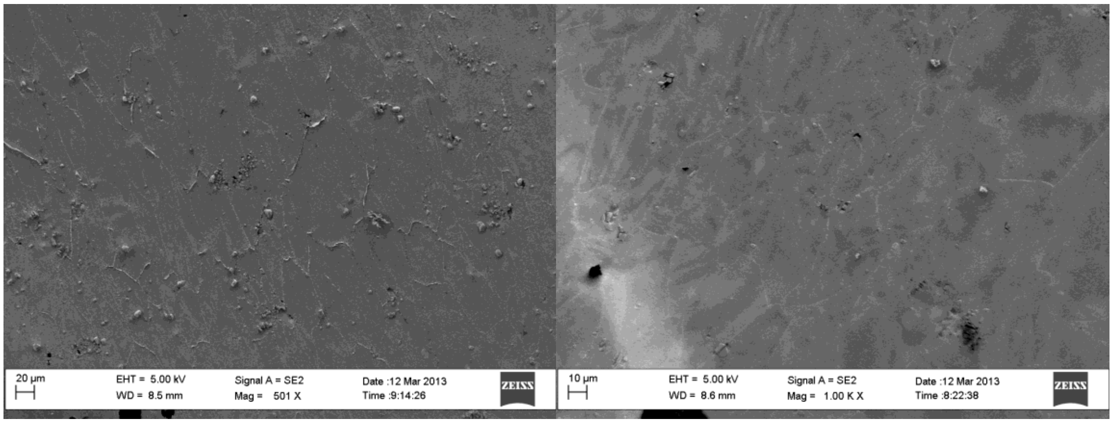

Figure 3.17 SEM images of the grain size of Inconel 617 deformed at 600 °C and 10^{-3} s^{-1}

The specimens tested at 600 °C and 10^{-3} s^{-1} showed some dissolution of large carbides. But the dissolution was not extensive as the average size of precipitates remained close to the initial size as seen in Figure 3.18. As can be seen in Figure 3.19 many smaller $M_{23}C_6$ carbides have reprecipitated from the larger M_6C carbides. In such precipitates the carbon atoms have yet to diffuse throughout the matrix. At the same time these original carbides have decreased in size indicating that the diffusion process has begun but requires a higher temperature for full dissolution.

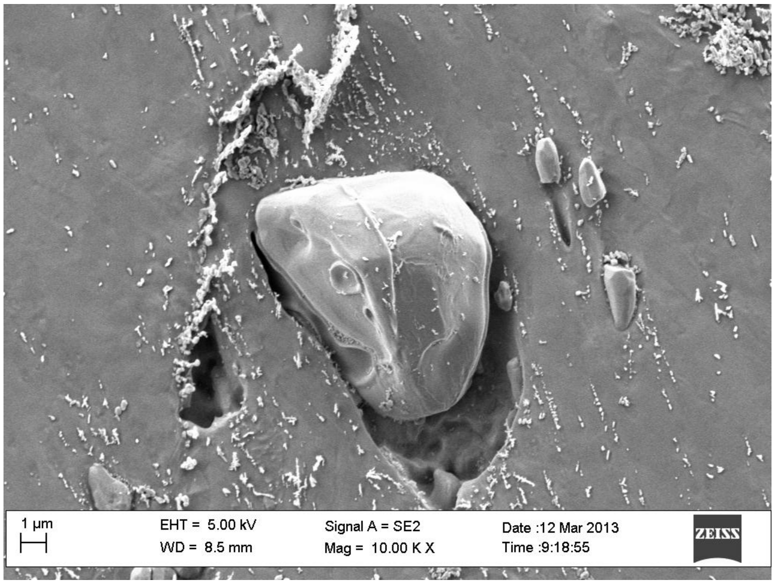

Figure 3.18 SEM image of larger precipitate in Inconel 617 after testing at 600 °C and 10^{-3} s^{-1}

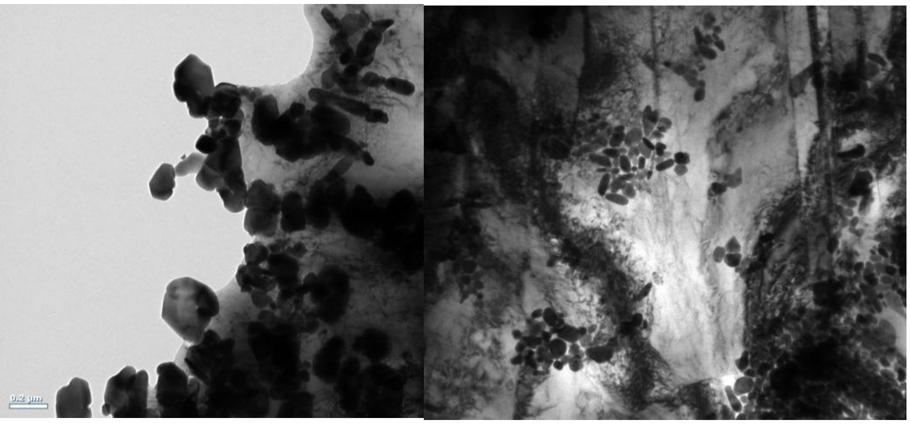

Figure 3.19 TEM micrographs of reprecipitated $M_{23}C_6$ carbides at of Inconel 617 after tensile testing at 600 °C and 10^{-3} s^{-1}

b) 800 °C/10^{-3} s^{-1}

Inconel samples tested at 800 °C and 10^{-3} s^{-1} possessed an elongated grain structure when observed close to the fracture area. The average size of grains actually increased to 39 µm as the grains were stretched along the deformation axis as can be seen in Figure 3.20. Distinct slip bands were also observed under both TEM and SEM. Such slip bands form during the initial plastic deformation when strain hardening takes place. Two types of precipitates were observed under these conditions. Large, faceted precipitates similar to the as-received material were found throughout the grains. These precipitates were anywhere in size from 1-3 µm, a severe reduction in size from the 4-10 µm precipitates seen in the as-received material. However, smaller precipitates were also present, covering a large portion of the surface as can be seen in Figure 3.21. These smaller precipitates were anywhere from 20-200 nm in size. In some cases these smaller carbides were found on top of the larger carbides. Both types were chromium and molybdenum rich carbides, with the smaller ones most likely being the $M_{23}C_6$ type [38]. There was also some evidence of the original locations of the M_6C carbides along the grain boundaries.

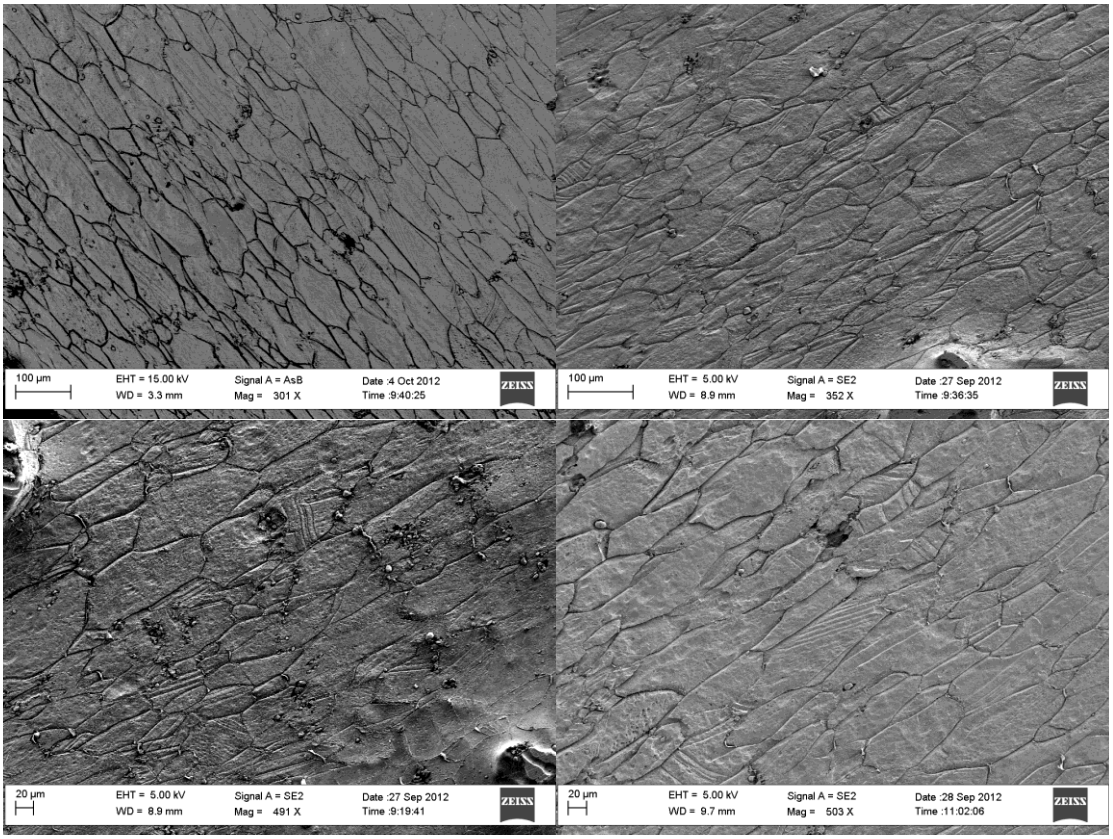

Figure 3.20 Elongated grain structure of Inconel 617 at 800 °C and 10^{-3} s^{-1}

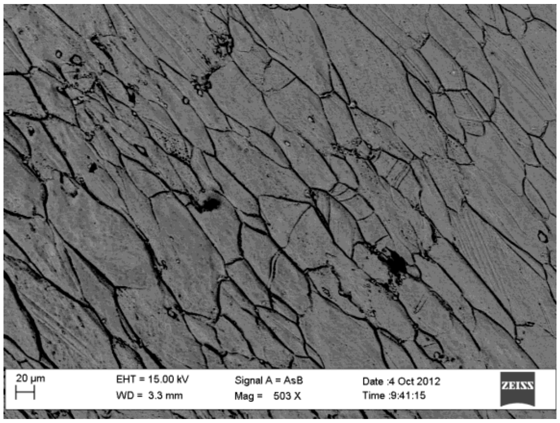

Figure 3.20 Elongated grain structure of Inconel 617 at 800 °C and 10^{-3} s^{-1}

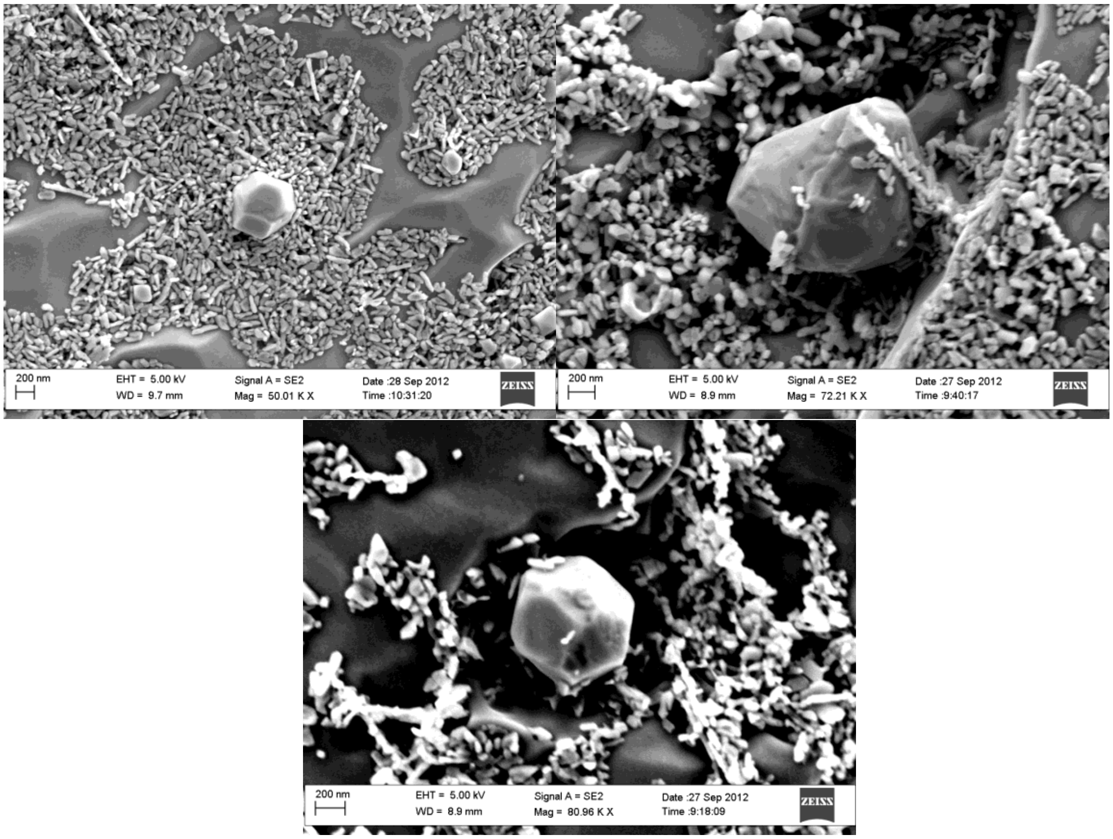

Figure 3.21 Precipitates present in Inconel 617 deformed at 800 °C and 10^{-3} s^{-1}

c) 800 °C/10^{-5} s^{-1}

When the strain rate was slowed to 10^{-5} s^{-1}, posttest examinations showed grains near the fracture area with some elongation but recrystallization had also occurred. Grain boundaries were less distinct so grain size measurements weren't possible, but grain refinement seems to have occurred as seen in Figure 3.22. Recrystallized grains appeared to nucleate on grain boundaries and deformation twins. The same types of carbides existed as at 10^{-3} s^{-1}, but the $M_{23}C_6$ type completely covered the surface and to a larger extent they laid on top of the M_6C carbides.

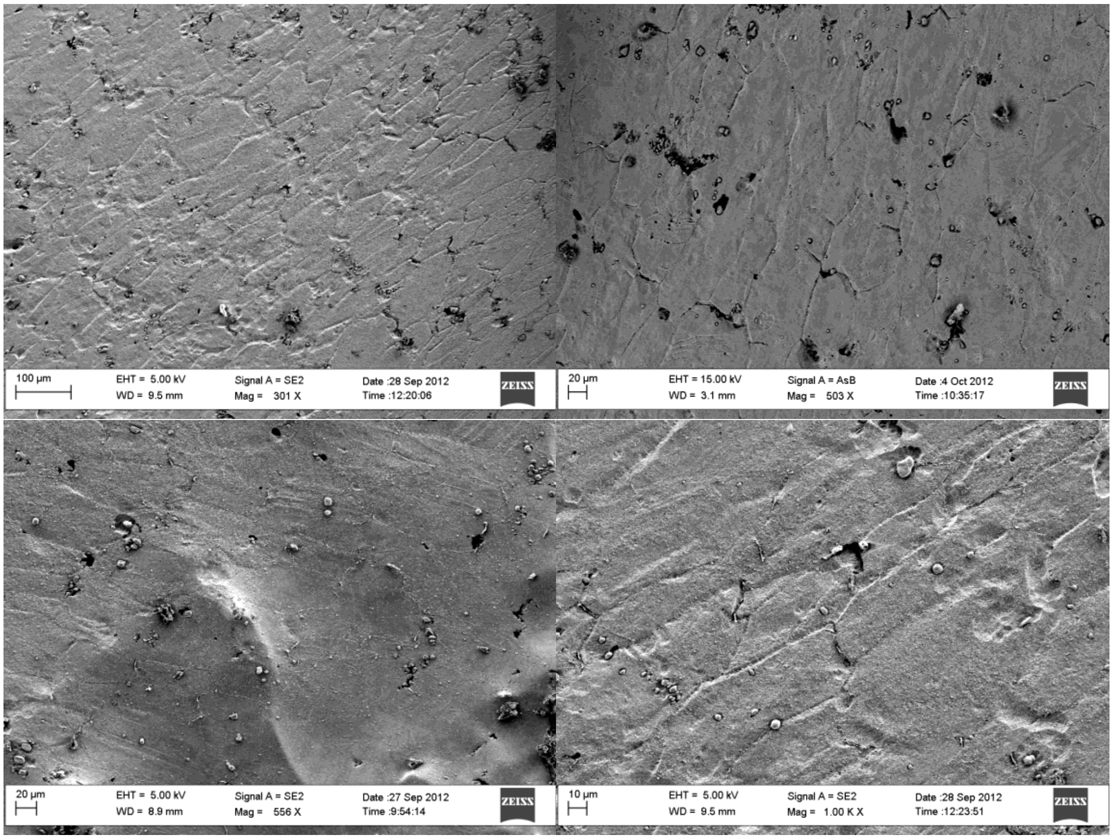

Figure 3.22 Recrystallized grains of Inconel 617 deformed at 800 °C and 10^{-5} s^{-1}

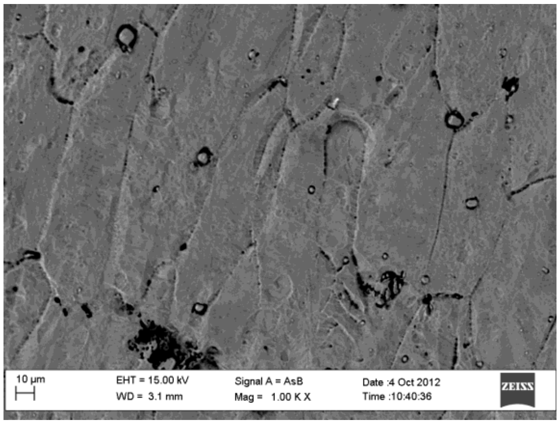

Figure 3.22 Recrystallized grains of Inconel 617 deformed at 800 °C and 10^{-5} s^{-1}

d) 950 °C/10^{-3} s^{-1}

At higher temperatures of 950 °C, complete recrystallization ensued near the fracture region. Again, it was difficult to discern each grain boundary but the large, equiaxed grains present in the as-received material had completely disappeared. Comparing Figures 3.22 and 3.23 it is evident that recrystallization occurred to a greater extent at 950 °C than at 800 °C. TEM micrographs also clearly show these smaller grains, with some recrystallized grains as small as 500 nm as seen in Figure 3.25. Also notice in Figure 3.25 that the reprecipitated carbides tend to aggregate along the subgrain boundaries. As can be seen in Figure 3.26, TEM micrographs of the smaller $M_{23}C_6$ carbides are a predominant feature of the microstructure now as nearly all of the initial M_6C carbides have dissolved, leading to reprecipitation. The $M_{23}C_6$ type carbides are sometimes found along subgrain and grain boundaries as seen in Figure 3.25. They also covered a large portion of the matrix surface as evidenced in Figure 3.26. This may be a result of electropolishing as electrostatic forces cause the precipitates to stick to the surface of the sample. Both types of precipitates were again found to be rich in chromium and molybdenum.

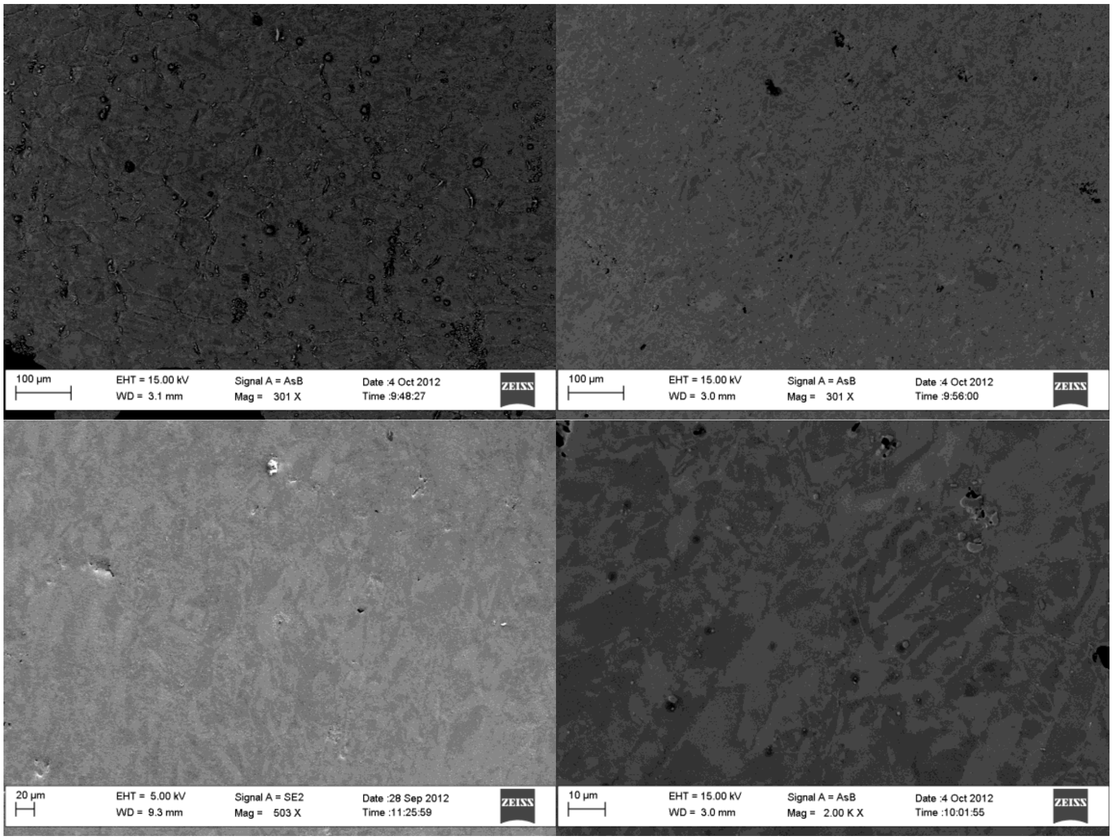

Figure 3.23 Grain structure of Inconel 617 after deformation at 950 °C and 10^{-3} s^{-1}

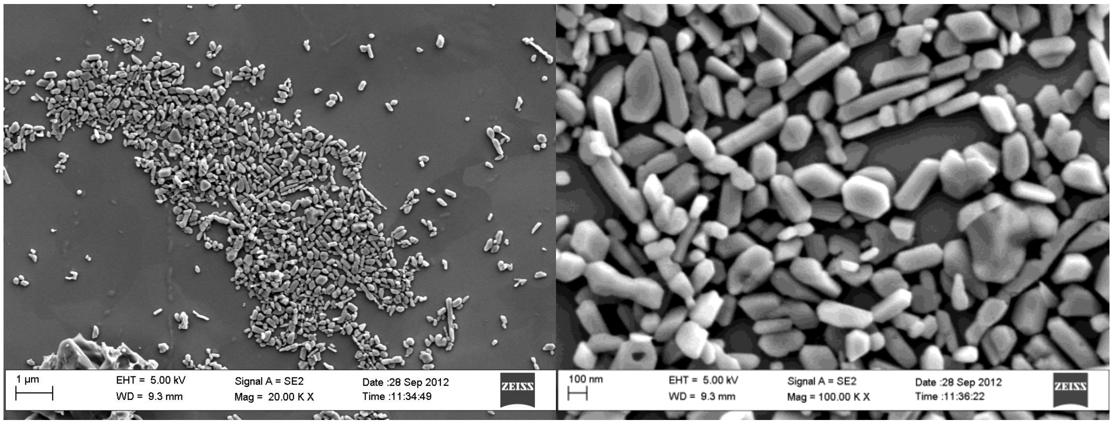

Figure 3.24 Small $M_{23}C_6$ carbides which have reprecipitated in Inconel 617 deformed at 950 °C and 10^{-3} s^{-1}

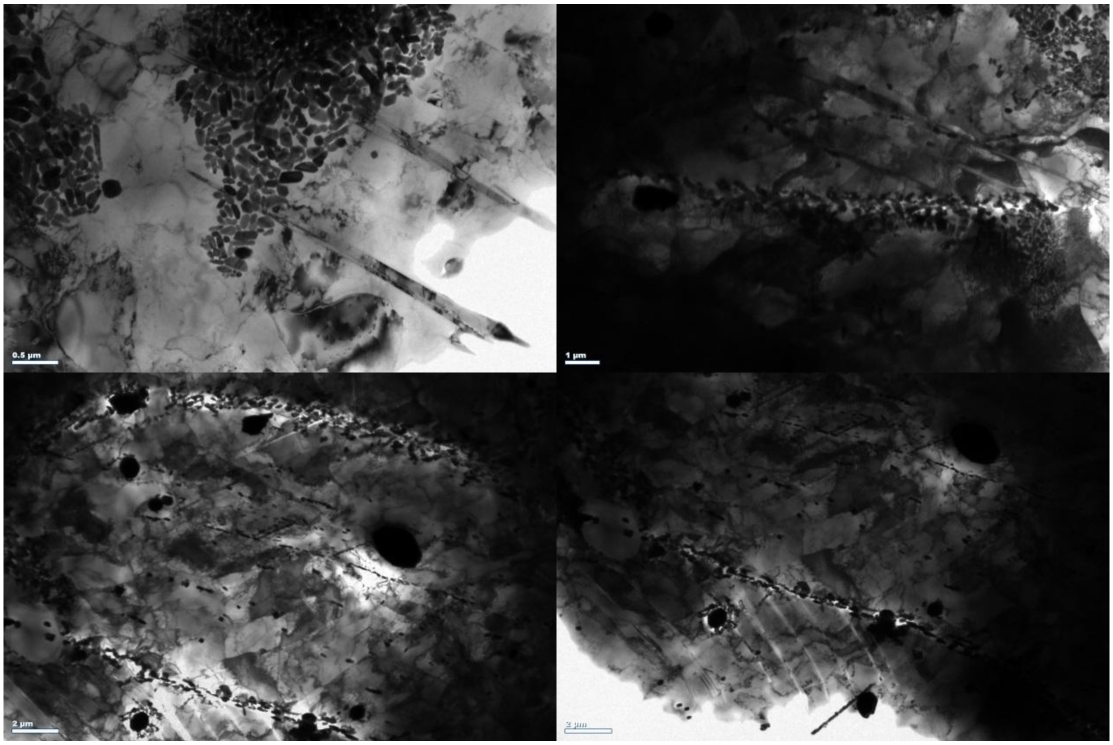

Figure 3.25 TEM micrographs of Inconel 617 deformed at 950 °C and 10^{-3} s^{-1} showing small recrystallized grain structure and carbides forming along subgrain boundaries

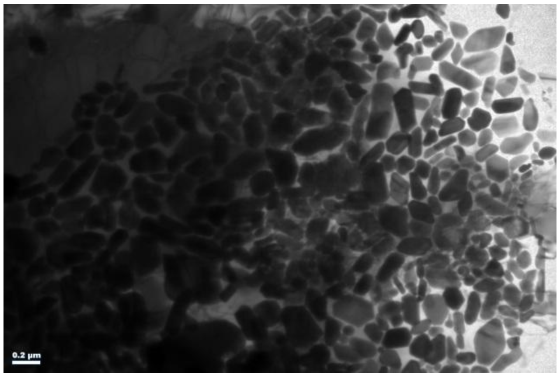

Figure 3.26 TEM micrographs of Inconel 617 deformed at 950 °C and 10^{-3} s^{-1} with $M_{23}C_6$ carbides precipitated throughout matrix

Further evidence of the reprecipitated $M_{23}C_6$ carbides can be found from XRD analysis. As can be seen in Figure 3.27a the five main matrix peaks are located at two theta values of 43.60°, 50.79°, 74.68°, and 90.63°, and 95.90°. These peaks are some mixture of nickel, chromium, and iron which make up a large part of the matrix. The relative intensity of these five peaks changes from the as-received material to those tested at elevated temperatures of 800 °C and 950 °C, indicating that there is a change in texture of matrix which may be caused by recrystallization. However, a zoomed-in look of the same spectrum seen in Figure 3.27b shows that the secondary peaks also evolve with temperature. Especially evident are the three peaks at two theta values of 19.04°, 21.08°, and 22.76°. In the as-received material there are no secondary peaks in these locations however they are quite distinct at 800 °C, and become even more so at 950 °C. This is indicative of carbide evolution taking place at higher temperatures. The same is true of the peaks located at two theta values of 35.81°, 39.23°, 72.83°, 77.04°, 81.43°, and 83.65°. Due to the complexity of Inconel 617 these peaks could not be distinctively identified. But previous studies have identified these metals by extracting the carbides from the matrix. They were identified as $M_{23}C_6$ carbides with the metals being a combination of molybdenum and chromium [38].

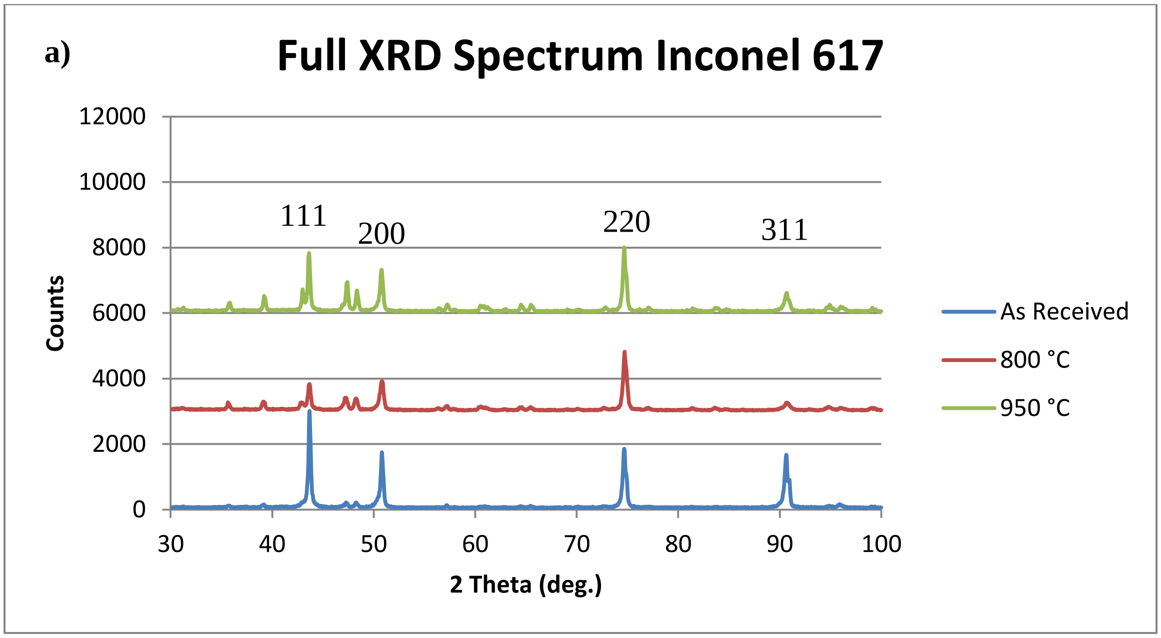

Figure 3.27 XRD spectrums of bulk samples of Inconel 617 with a) showing full peaks and b) showing the zoomed-in peaks

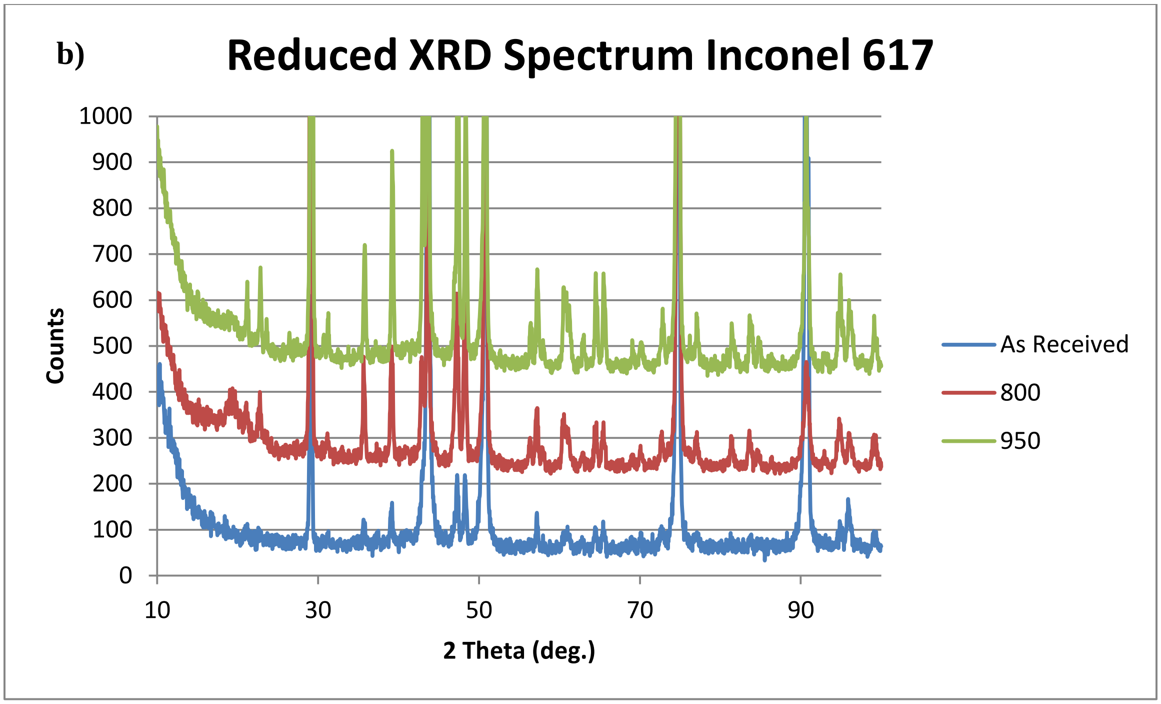

Figure 3.27 XRD spectrums of bulk samples of Inconel 617 with a) showing full peaks and b) showing the zoomed-in peaks

3.2.2 Haynes 230

Specimens of Haynes 230 were observed under SEM and TEM in order to identify precipitates, grain boundaries, and grain morphology. Samples deformed at temperatures of 600 °C, 800 °C and 950 °C and strain rates of 10^{-3} and 10^{-5} s^{-1} were examined, and each temperature and strain rate possessed a unique microstructure.

a) 600 °C/10^{-3} s^{-1}

When deformed at 600 °C, Haynes 230 retains a very similar grain structure to the as received material. Figure 3.28 shows the grains near the fracture region which are still mostly equiaxed, with a slight elongation in the tensile direction. Also noticeable are traces of slip bands in some of the grains. This sample is also characterized by large carbides with sporadically placed smaller precipitates seen in Figure 3.29. Many of these smaller precipitates seem to align along slip bands as seen in Figure 3.30. The rows may be areas where slip bands have formed, where diffusing carbon atoms migrate to and reprecipitate into the smaller carbides. They also congregate around the larger precipitates where the carbon appears to diffuse and reprecipitate into the smaller $M_{23}C_6$ carbide. Forests of dislocations appear throughout the matrix which further pin other dislocations into immobile locations, shown in Figure 3.31. The pinning of dislocations may be responsible for the serrated flow observed at 600 °C, as dislocations build up in one area until there are enough to break free of the immobile dislocation and continue smooth plastic flow. This will be discussed further in Chapter 4.

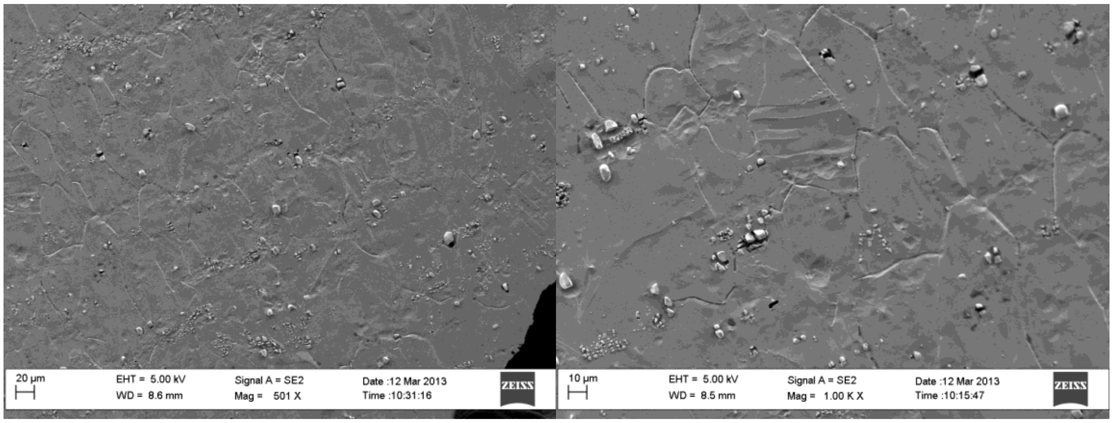

Figure 3.28 Grain structure of Haynes 230 deformed at 600 °C and 10^{-3} s^{-1}

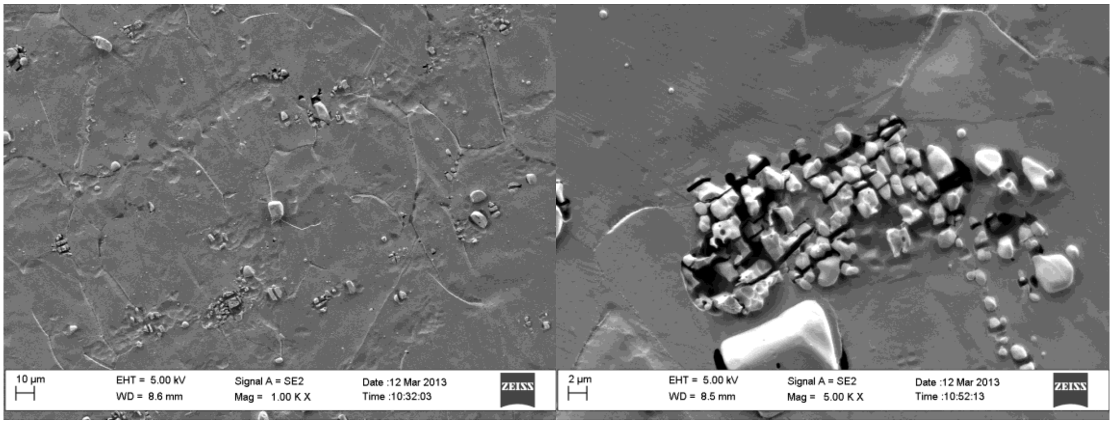

Figure 3.29 Many large carbides continue to exist in Haynes 230 microstructure deformed at 600 °C and 10^{-3} s^{-1}

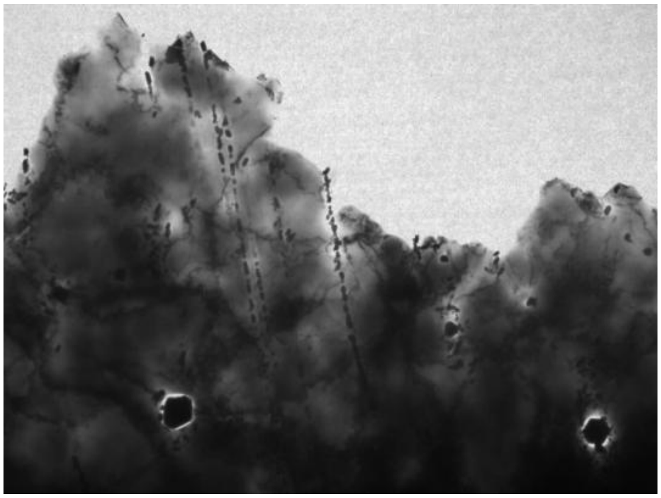

Figure 3.30 Rows of smaller carbides aligning into grain boundaries in Haynes 230 deformed at 600 °C and 10^{-3} s^{-1}

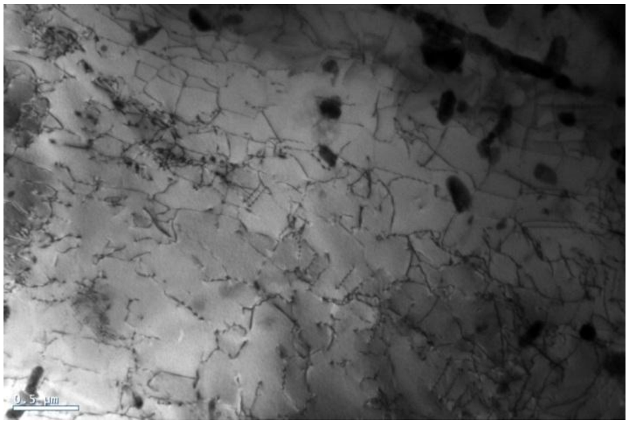

Figure 3.31 Forests of dislocation impeding further dislocation motion in Haynes 230 deformed at 600 °C and 10^{-3} s^{-1}

b) 800 °C/10^{-3} s^{-1}

Alloy 230 displayed a similar microstructure to that of alloy 617 at 800 °C and 10^{-3} s^{-1}. Grain elongation took place near the fractured area; however grain size was only reduced to 38 µm as shown in Figure 3.32. The images used to analyze grain size data are presented in Appendix A. $M_{23}C_6$ type carbides were observed to a lesser extent than Inconel 617, as they were sparsely interspersed through the matrix. More common were the M_6C type carbides which were anywhere in size from 4-9 µm in size and can be seen in Figure 3.33. These carbides exhibited much less dissolution as the initial carbides were no larger than 11 µm. Both of these carbides were rich in tungsten.

TEM micrographs again confirm large amounts of small reprecipitated carbides littered throughout the matrix. In many cases the carbides are aligned into parallel lines forming small bands as seen in Figure 3.34. These bands often form in parallel and terminate at grain boundaries. In some areas it is also possible to observe the diffusion process as large M_6C carbides are seen shrinking and have a more globular appearance (Figure 3.36). Along with these carbides there are large tangles of dislocations. Such a high dislocation density probably improves the strength of the alloy and gives it the region of work hardening observed at 10^{-3} s^{-1}.

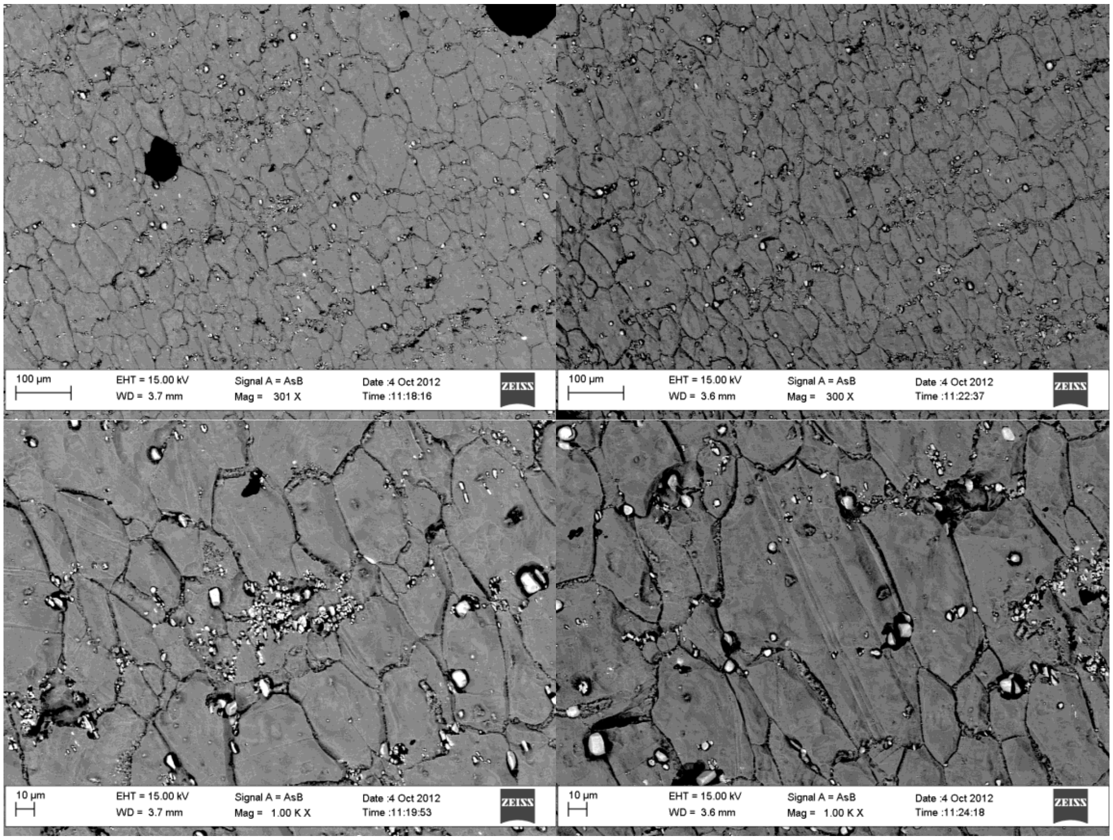

Figure 3.32 Grain Structure of Haynes 230 after deformation at 800 °C and 10^{-3} s^{-1}

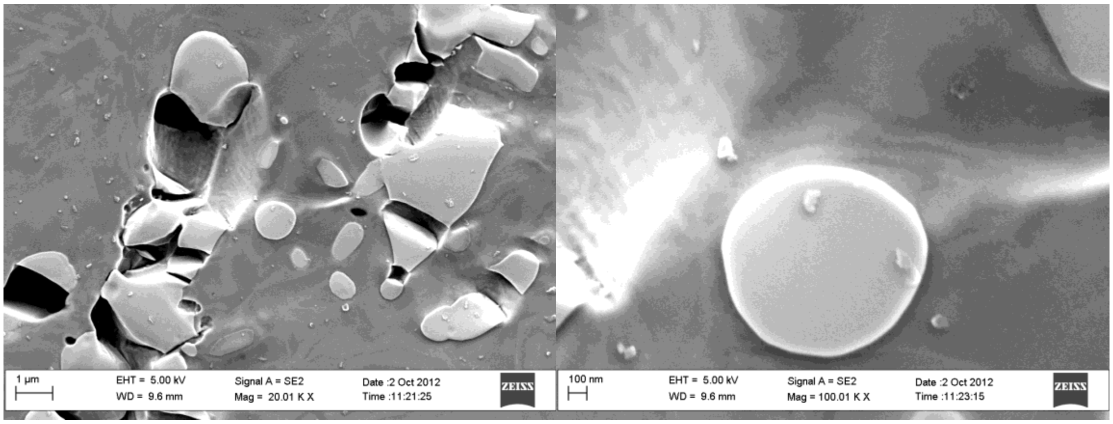

Figure 3.33 Haynes 230 carbides after deformation at 800 °C and 10^{-3} s^{-1}

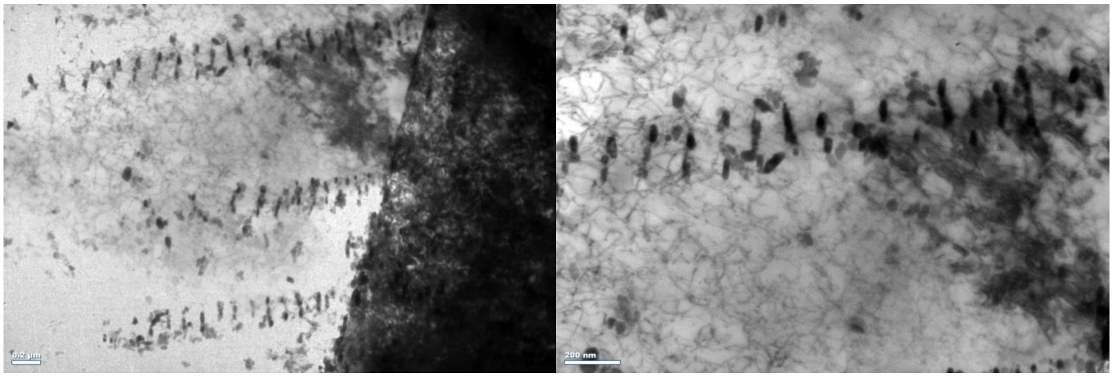

Figure 3.34 Bands of small reformed carbides in Haynes 230 after deformation at 800 °C and 10^{-3} s^{-1}

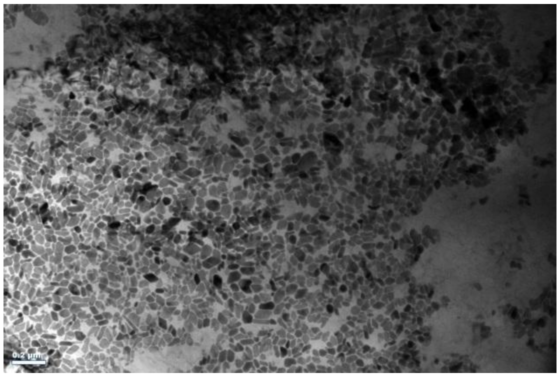

Figure 3.35 Aggregations of tiny secondary precipitates in Haynes 230 after deformation at 800 °C and 10^{-3} s^{-1}

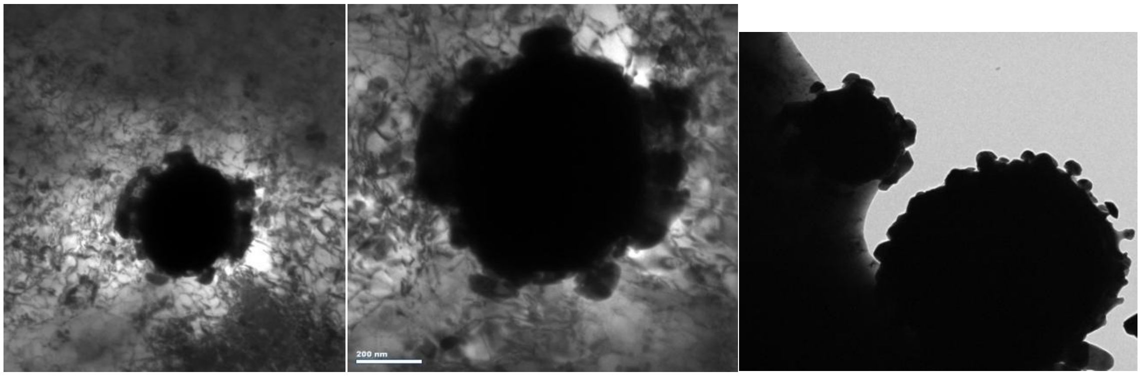

Figure 3.36 Large M_6C carbides start to lose their shape as solute atoms diffuse into the matrix at 800 °C and 10^{-3} s^{-1} in Haynes 230

c) 800 °C/10^{-5} s^{-1}

At a strain rate of 10^{-5} s^{-1}, grain boundaries were easier to locate than Inconel 617 as seen in Figure 3.37. Also, near the fracture region Haynes retained more of the original carbide structure than Inconel, as deformed carbides could still be seen in the rolling direction. However the size of the large precipitates decreased when compared to initial microstructure partial dissolution which is clearly visible in Figure 3.38. Recrystallization had taken place to some extent and the grains were more equiaxed than elongated. Reprecipitation of the $M_{23}C_6$ carbides also took place with the presence of numerous small precipitates as shown in Figure 3.38. In addition to amassing on subgrain boundaries, the $M_{23}C_6$ carbides also appeared preferentially on slip bands. These also were tungsten rich and ranged in size from 50-100 nm. TEM micrographs show bands of these precipitates as seen in Figure 3.39. In some cases these bands were observed to cross which could impede plastic deformation of the material (Figure 3.40).

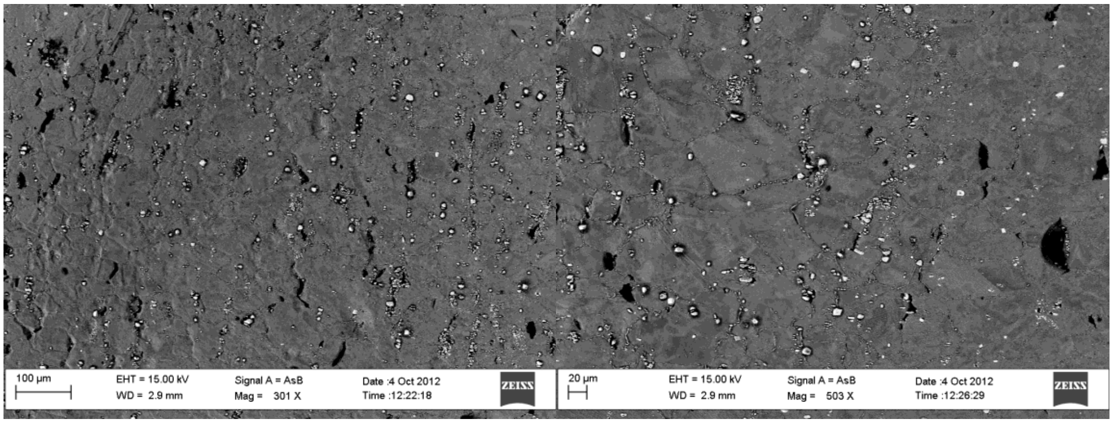

Figure 3.37 Grain Structure of Haynes 230 after deformation at 800 °C and 10^{-5} s^{-1}

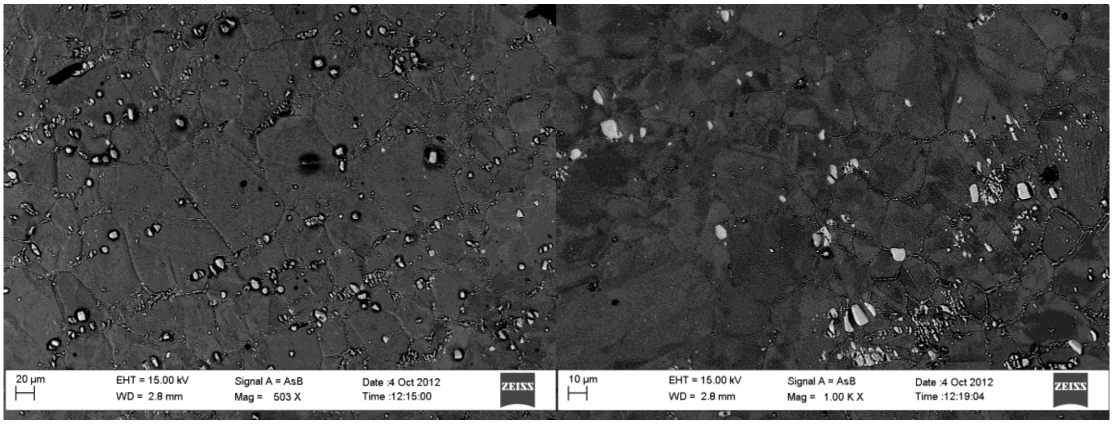

Figure 3.37 Grain Structure of Haynes 230 after deformation at 800 °C and 10^{-5} s^{-1}

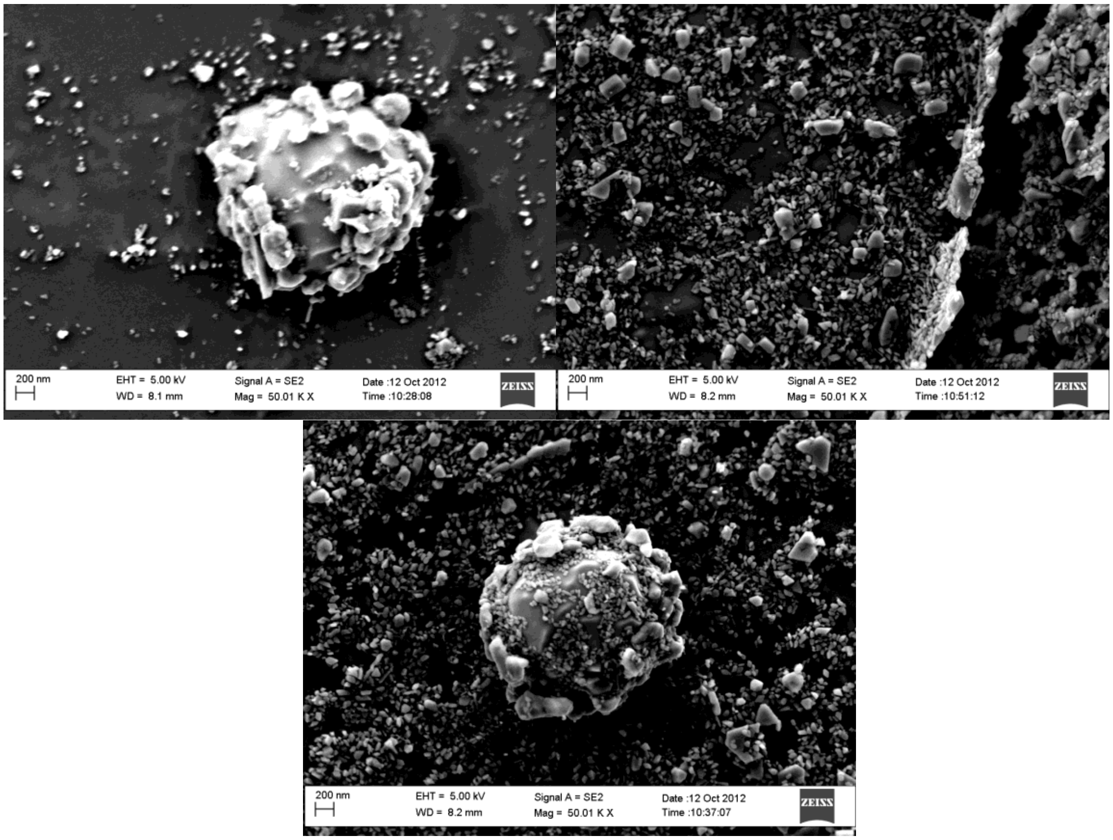

Figure 3.38 Surface of Haynes 230 after deformation at 800 °C and 10^{-5} s^{-1}

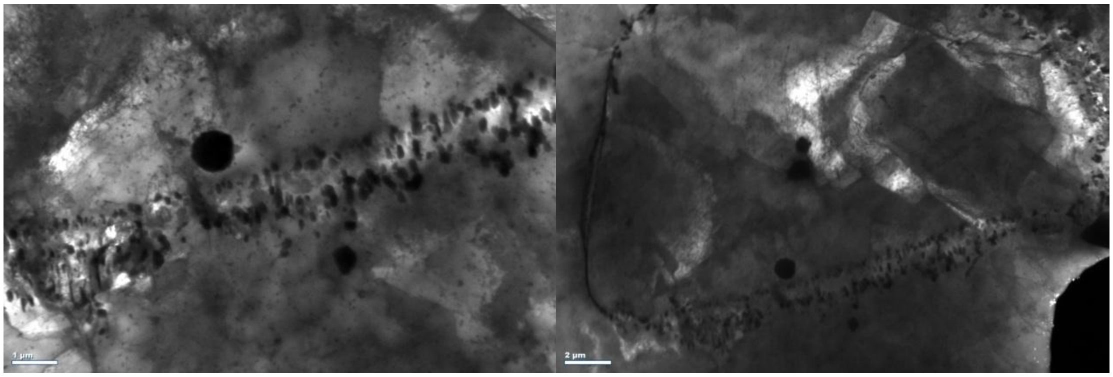

Figure 3.39 Bands of precipitates aligned in Haynes 230 following deformation at 800 °C and 10^{-5} s^{-1}

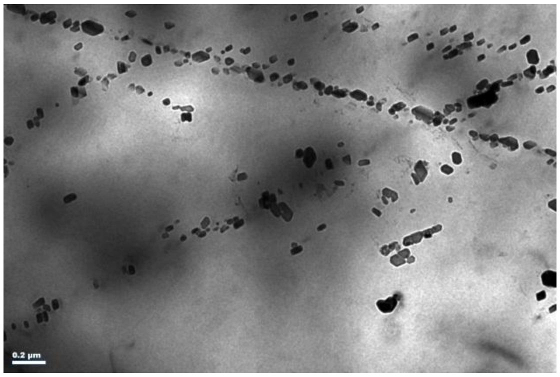

Figure 3.40 Crossing bands of precipitates formed in Haynes 230 following deformation at 800 °C and 10^{-5} s^{-1}

d) 950 °C/10^{-3} s^{-1}

Recrystallization is even more apparent in Haynes 230 than Inconel 617 at 950 °C. Low magnification SEM photos show a texture of refined grains much smaller than the as-received material as shown in Figure 3.41. Such grain refinement is due to recrystallization. Similar to lower temperatures, the alloy again maintained much of its original carbide structure with deformed carbides observed in the rolling direction. However the size of these large precipitates decreased indicating partial dissolution. Also reprecipitation of small carbides happened along grain boundaries as shown in Figure 3.42. A higher magnification micrograph shows that reprecipitation also occurs intragranularly (Figure 3.42). Unlike alloy 617, the original carbides changed morphology and seemed to form a more globular shape.

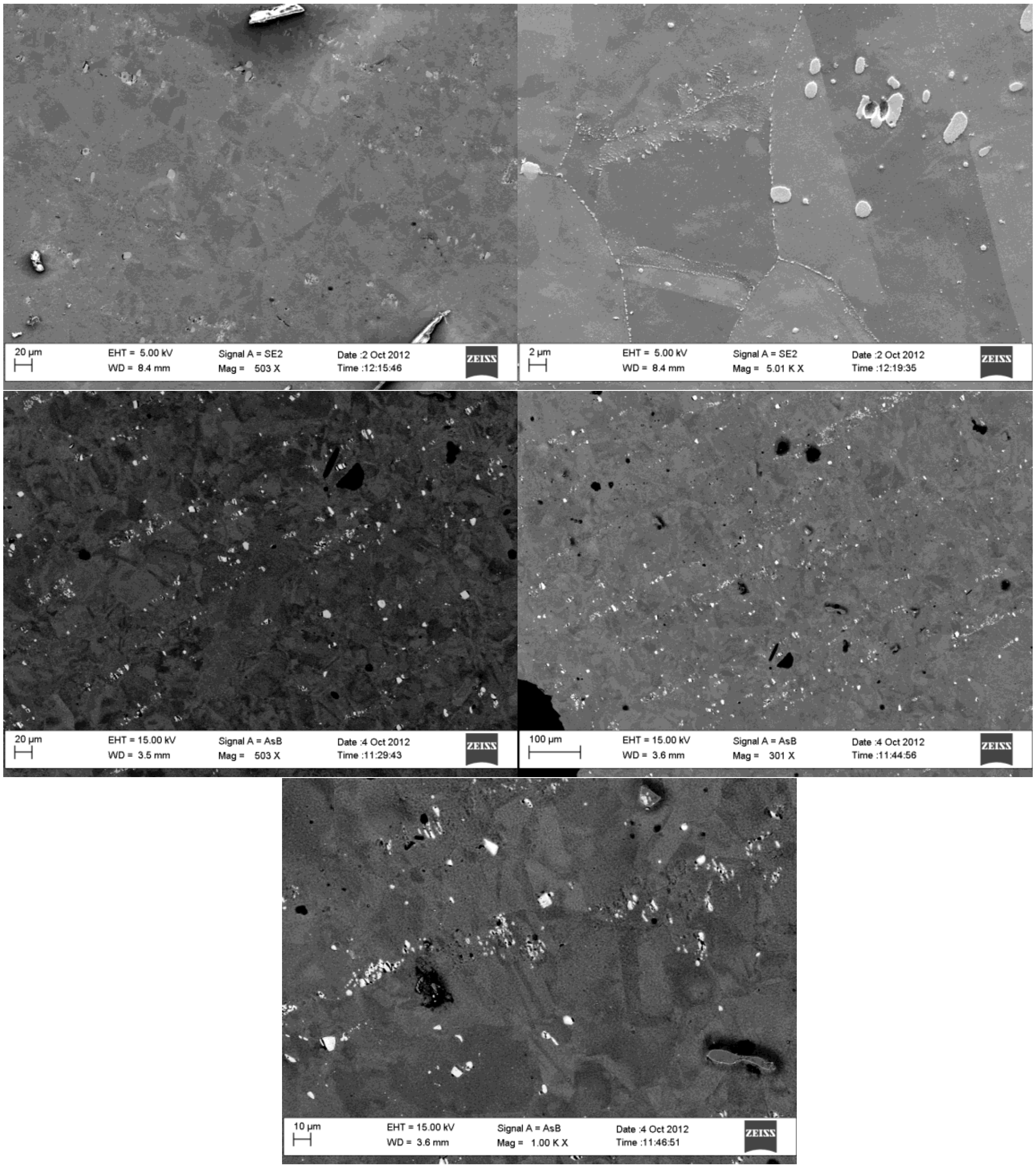

Figure 3.41 Grain structure of Haynes 230 after deformation at 950 °C and 10^{-3} s^{-1}

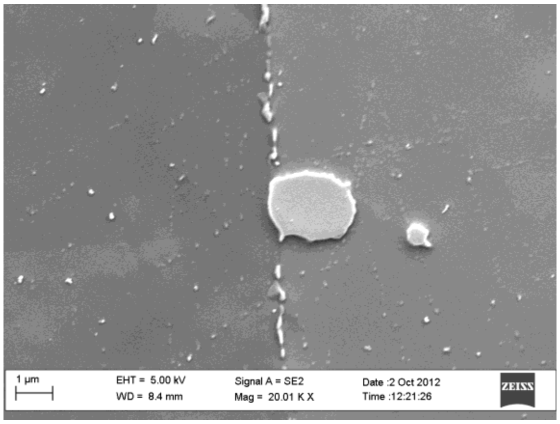

Figure 3.42 Carbide morphology of Haynes 230 after deformation at 950 °C and 10^{-3} s^{-1}

XRD analysis of Haynes 230 was very similar to that of Inconel 617. The matrix peaks were located at two theta values of 43.60°, 50.79°, 74.67°, and 90.63° and 95.90°. Again this identified with some variation of nickel chromium iron mixture which formed the matrix. The relative intensity of these five peaks changes from the as-received material to those tested at elevated temperatures of 800 °C and 950 °C, indicating that there is a change in texture of matrix possibly caused by recrystallization. More interesting are the secondary peaks which can be seen in Figure 3.43b. As stated before, Haynes 230 retains more of its original microstructure at elevated temperatures than does Inconel 617. The secondary peaks show less relative growth at higher temperatures than those in Inconel 617. This agrees with previous SEM and TEM observations in which fewer secondary carbides were observed forming at higher temperatures. Again, the peaks could not be explicitly identified as several phases interfere with each other and the peaks are convoluted. Extractions were performed on Haynes 230 using aqua regia however many of these peaks were obscured by chlorides which were formed with tungsten. These spectra are presented in Appendix B. Comparisons of Inconel 617 and

Haynes 230 can also be seen in Appendix B, in which the carbide evolutions can clearly be distinguished between the two.

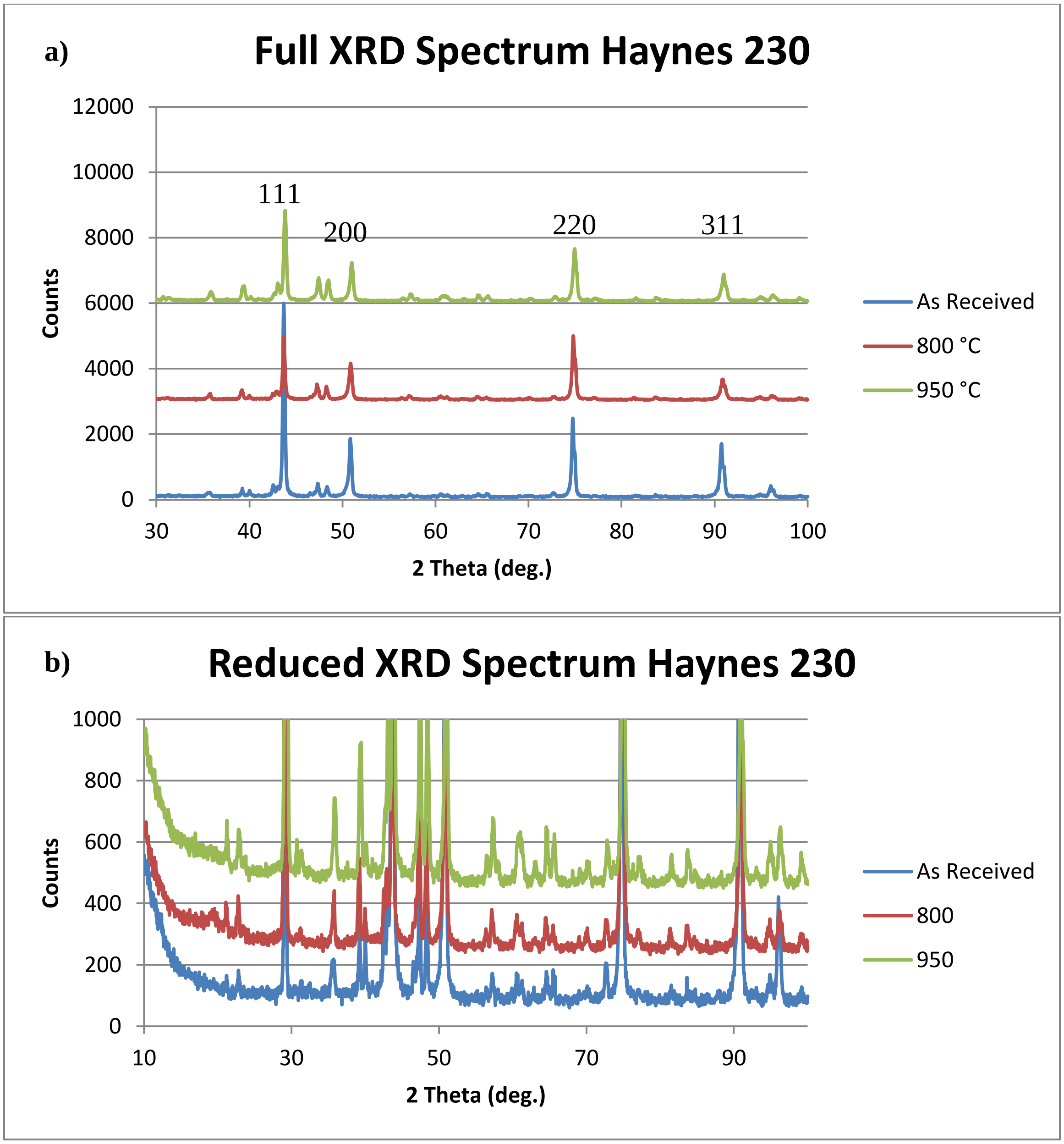

Figure 3.43 XRD spectrums of bulk samples of Haynes 230 with a) showing full peaks and b) showing the zoomed-in peaks

CHAPTER 4

Discussion

This chapter discusses the experimental results presented in chapter 3. Results are compared to previous studies and deformation mechanisms are discussed, with the overall goal to explain the effects of strain rate and temperature on the mechanical properties as well as the observed serrated yielding.

4.1 Mechanical Properties

This section explores the shifts observed in yield strength, ultimate tensile strength, and total elongation as the temperature and strain rate change. Competing processes take place as the materials are deformed: hardening processes such as dynamic strain ageing (DSA), and softening processes such as dynamic recrystallization (DRX). The following subsections explore the dominant mechanism at each temperature and strain rate.

4.1.1 Yield Strength

a) Temperature Effect:

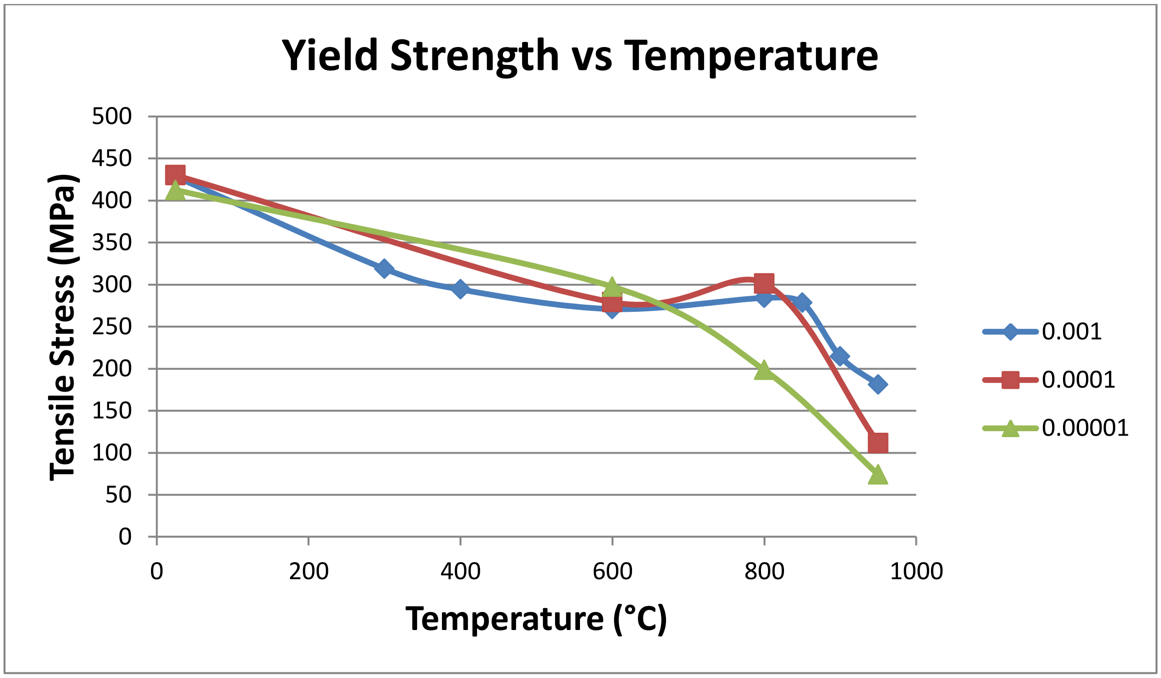

Figure 4.1 Yield strength as a function of temperature of Inconel 617

The yield strength tends to decrease with an increase in temperature. Especially at a strain rate of 10^{-5} s^{-1}, the yield strength quickly decreases above temperatures of 600 °C (Figure 4.1). However, there are some interesting irregularities at the faster strain rates. At strain rates of 10^{-3} and 10^{-4} s^{-1} there is an increase in yield strength from 600-800 °C before decreasing to the value recorded at 950 °C. As mentioned in Chapter 3 this is a phenomenon known as Yield Strength Anomaly (YSA) in which the yield strength actually increases at elevated temperatures. YSA is generally found in ordered, intermetallic $L1_2$ alloys at about one half of the melting point [39]. The melting point of Inconel 617 is in the range of 1332-1380 °C [36], so that YSA occurs at 45-60% of the melting temperature in this study. Roy et. al observed the phenomena when testing

Inconel alloys 617 and 718 in the temperature ranges 800-900 °C and 700-800 °C, respectively [40, 41]. The mechanism behind YSA is not fully understood yet, but may be due to the phase transformation of precipitates formed at 800 °C, as indicated in previous micrographs. The dissolution of the original carbides, reported in our study above 600 °C, works in two manners to harden the alloys. First it adds a significant amount of solute atoms into the matrix which act as barriers to dislocation motion. At 800 °C, the initial large M_6C carbides have significantly dissolved and reprecipitated into small $M_{23}C_6$ carbides as can be seen in Figure 4.2. Figure 4.3 also shows dislocation pile-ups at grain boundaries which would cause further hardening. The same could be said at 950 °C, however at this higher temperature the thermal energy is great enough for dislocations to move by barriers more easily. And more importantly, at 950 °C the strengthening provided by the precipitates must also compete with the softening process of recrystallization which was observed to be more extensive at 950 °C.

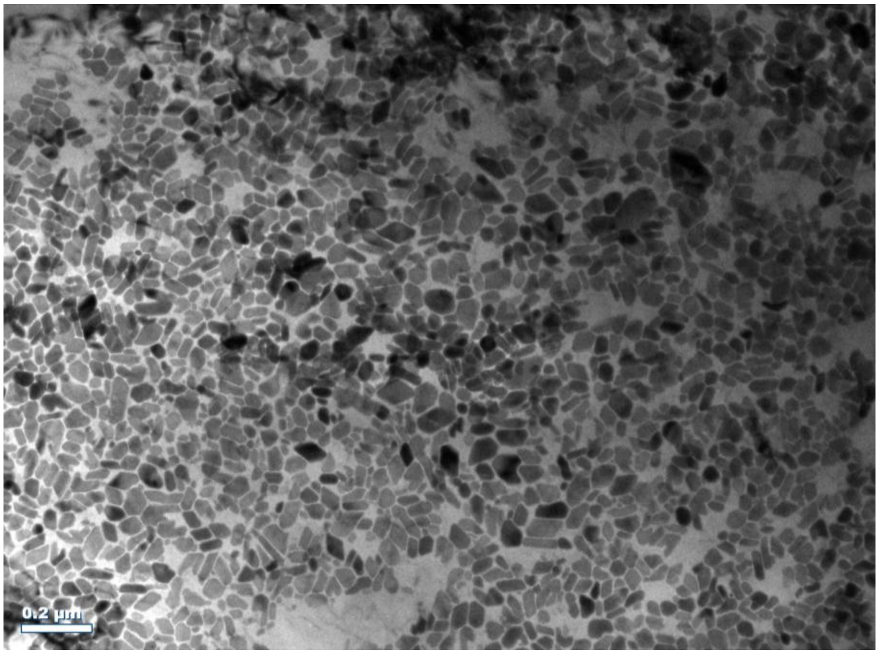

Figure 4.2 TEM micrograph of reprecipitated $M_{23}C_6$ carbides in Haynes 230 deformed at 800 °C and 10^{-3} s^{-1}

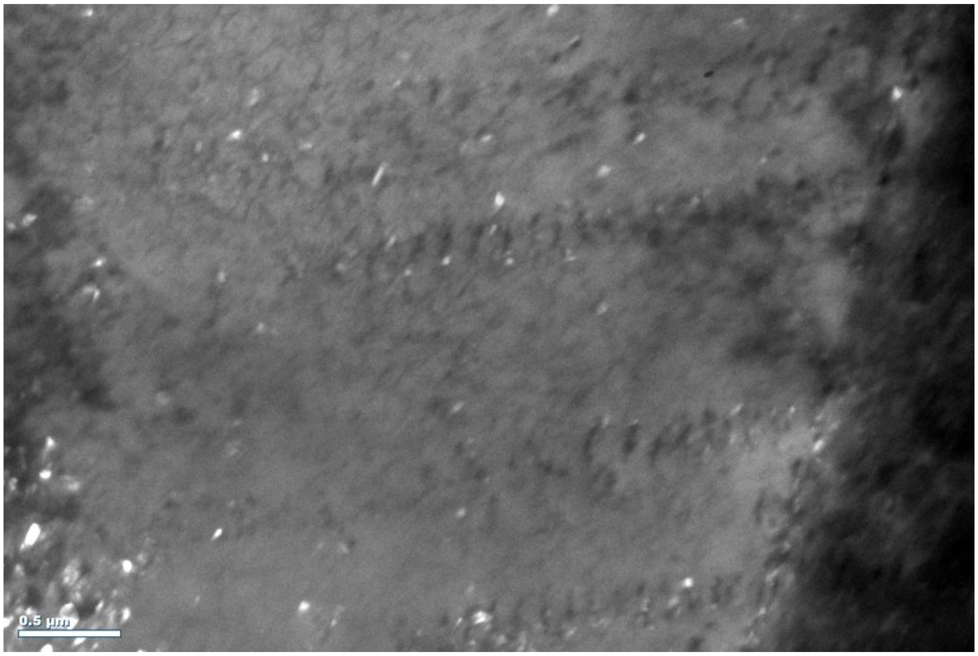

Figure 4.3 TEM micrograph showing dislocation pile-ups at grain boundaries in Haynes 230 deformed at 800 °C and 10^{-3} s^{-1}

b) Strain Rate Effect:

In our experiments, strain rate had a noticeable effect on the yield strength of the material depending on the temperatures. At room temperature, there was a minimal change in the yield stress due to strain rate.

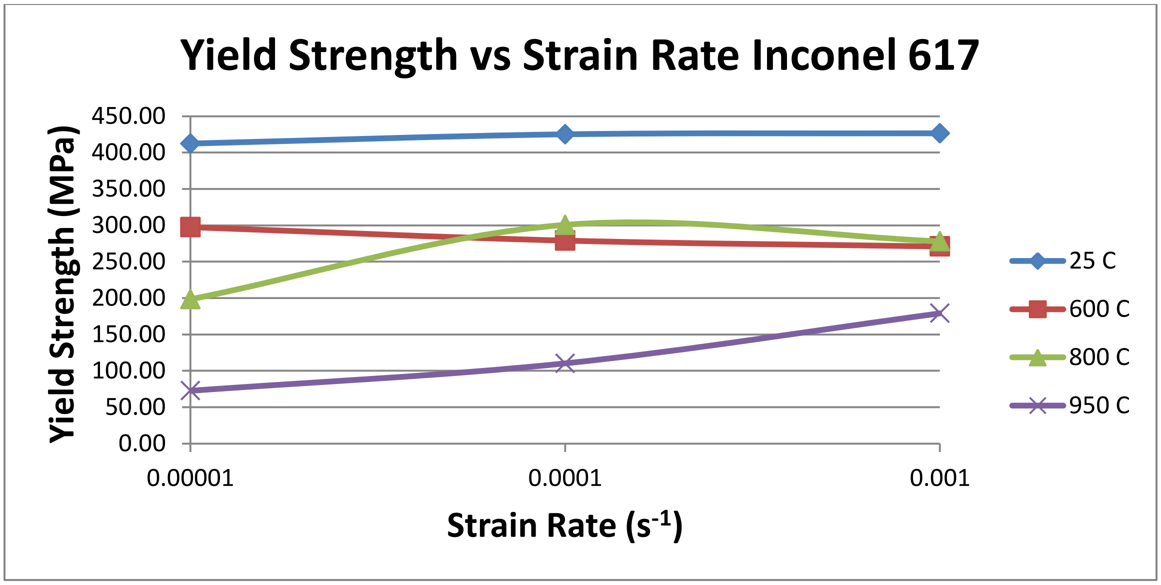

Figure 4.4 Yield strength as a function of strain rate of Inconel 617

At 600 °C, there is a slight increase in yield stress with decreasing strain rate from 270.9 MPa at 10^{-3} s^{-1} to279.0 MPa at 10^{-4} s^{-1} and 297.5Mpa at 10^{-5} s^{-1} as seen in Figure 4.4. This increase may be due to the onset of the dissolution of the large carbides which puts a certain amount of solute atoms in solution followed by reprecipitation of smaller intra and inter granular carbides. TEM evidence of the smaller secondary precipitates is shown in Figure 4.5. Electron microscopy of the test samples showed that this process is limited at 600 °C compared to 800 °C and 950 °C. When decreasing the strain rate, the time necessary to reach yield is increased and the process of dissolution may be enhanced during that time frame. Indeed, the dissolution of the large precipitates and the formation of small $M_{23}C_6$ carbides may occur to a great extent in the time frame needed to reach yield at lower strain rates as shown in table 4.1. The difference in time it takes to reach yield at a given temperature increases with decreasing strain rate, while the yield stress value reached decreases. Increasing times necessary to reach yield allow for the dissolution of the larger precipitates to occur to a greater extent. The solute atoms act as obstacles to dislocation motion which is known as solute drag. But once these solutes have reached a certain concentration they begin to form the secondary $M_{23}C_6$ carbides mentioned above. Again these larger formations inhibit the movement of dislocations. Dislocations may have the ability to cut through some precipitates with enough applied energy, or they may have to bow around other precipitates.

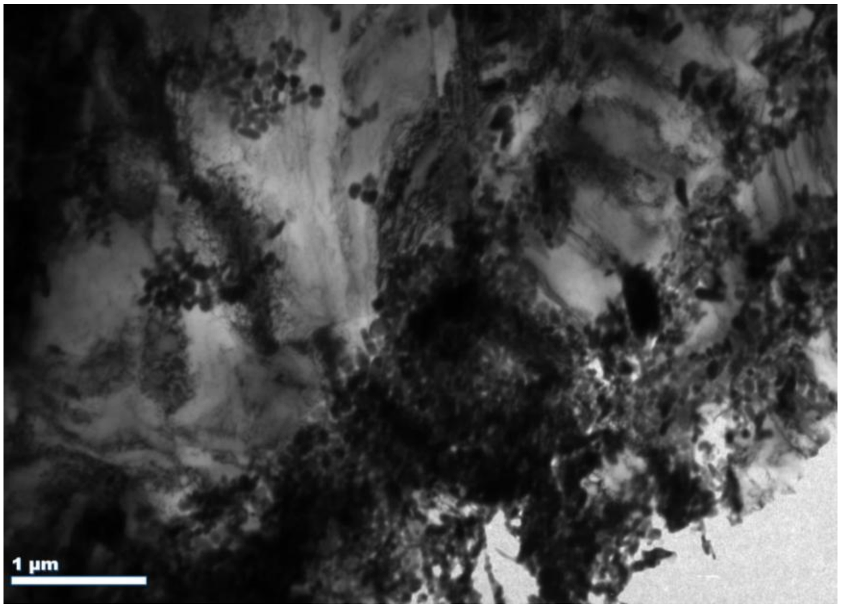

Figure 4.5 TEM micrograph of secondary precipitate formation in Inconel 617 deformed at 600 °C and 10^{-3} s^{-1}

At 800 °C, the yield stress increases when going from 10^{-3} s^{-1} to 10^{-4} s^{-1} and then a noticeable decrease in yield stress occurs from 10^{-4} s^{-1} to 10^{-5} s^{-1}. The shape of the stress-strain curve is affected by the transition in strain rate from 10^{-4} s^{-1} to 10^{-3} s^{-1} as seen in figure 4.4. The yield point is followed by a short strain hardening section at 10^{-3} s^{-1} which is suppressed at 10^{-4} s^{-1}as the material is subject to a softening mechanism. Indeed, at 10^{-4} s^{-1} and 10^{-5} s^{-1}, the stress-strain curve decreased after yielding, probably due to dislocations escaping from Cotrell atmospheres, followed by a slight increase which leaves the values of stress below the yield stress value; quickly thereafter the stress-strain monotonically decreases showing that the material deformation is controlled essentially by a softening mechanism (dynamic recrystallization).

Similarly to 600 °C, the small increase in yield stress from 10^{-3} s^{-1} to 10^{-4} s^{-1} may be attributed to the dissolution of the large precipitates and the formation of small $M_{23}C_6$ carbides as the dissolution of the original large M_6C carbides may occur to a greater extent in the time frame needed to reach yield at lower strain rates as shown in table 4.1. But at this temperature the process of dynamic recrystallization is noticeable and plays a big part in the microstructure evolution, which could explain the elimination of the strain hardening section of the stress-strain curve at 10^{-4} s^{-1} and the decrease in yield strength when going from 10^{-4} s^{-1} to 10^{-5} s^{-1}.

Table 4.1 Time to reach yield stress of Inconel 617

	1.00E-03		1.00E-04		1.00E-05	
	Time (s)	YS (MPa)	Time (s)	YS (MPa)	Time (s)	YS (MPa)
25	7.4	426.5	69	425.1	643	412.4
600	5.2	270.9	54	279.0	518	297.5
800	5	277.9	66	301.3	476	198.4
950	4.8	181.1	38	111.4	311	72.6

At 950 °C, the yield strength decreased monotonically with decreasing strain rate as seen in Figure 4.4. The yield stress follows the power law developed by Alder and Philips:

$$\sigma_y = C\dot{\varepsilon}^m$$

in which C is a constant and m is the strain rate sensitivity [42]. When applied to the values plotted in Figure 4.5 at 950 °C, the strain rate sensitivity is 0.1918. While the process of dissolution of initial large carbides and reprecipitation is even more extensive as shown in Figure 4.6, it is also likely to happen much more quickly in the first few minutes at this temperature (samples were held at each test temperature for 30 minutes to allow for thermal equilibrium). The dominant mechanism under deformation is dynamic recrystallization which should explain the trend of yield stress with strain rate: slower rates allow for more extensive recovery, recrystallization, and grain growth, than higher strain rates (i.e. shorter tests).

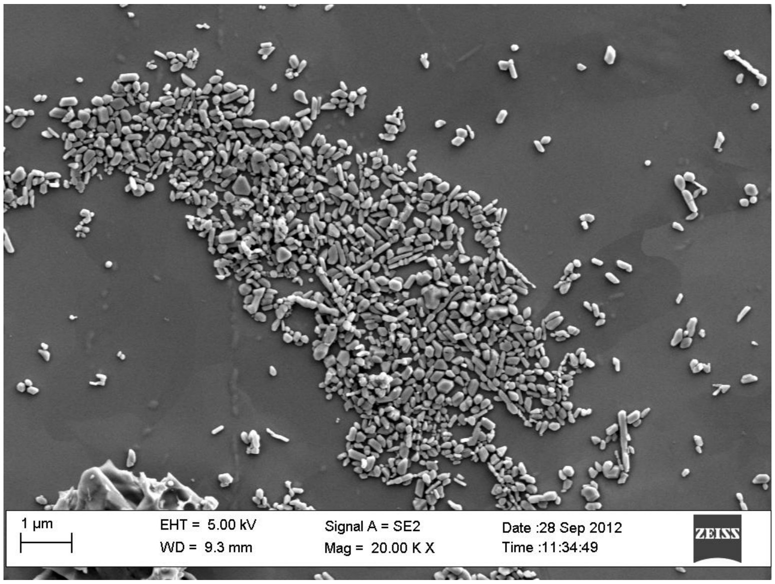

Figure 4.6 SEM image showing extensive reprecipitation in Inconel 617 deformed at 950 °C and 10^{-3} s^{-1}

4.1.2 Ultimate Tensile Strength

a) Temperature Effect:

Following yield, the alloys either undergo strain hardening or softening. Temperature is an important factor in determining whether hardening or softening occurs. The hardening process is caused by DSA, in which dislocations interact with solutes and their motion is impeded. On the other hand, the softening is caused by either recovery or recrystallization. Recovery occurs at intermediate temperatures when pairs of dislocations annihilate each other, decreasing the dislocation density. As mentioned in section 1.3, recrystallization is a process by which deformed grains with high density of dislocations are replaced by a new set of "undeformed" grains that nucleate and grow until the original grains have been entirely consumed. Recrystallization is usually accompanied by a reduction in the strength and hardness of a material and a simultaneous increase in the ductility. These hardening and softening processes at play in our alloys are all competing mechanisms which influence the tensile strength of the alloys.

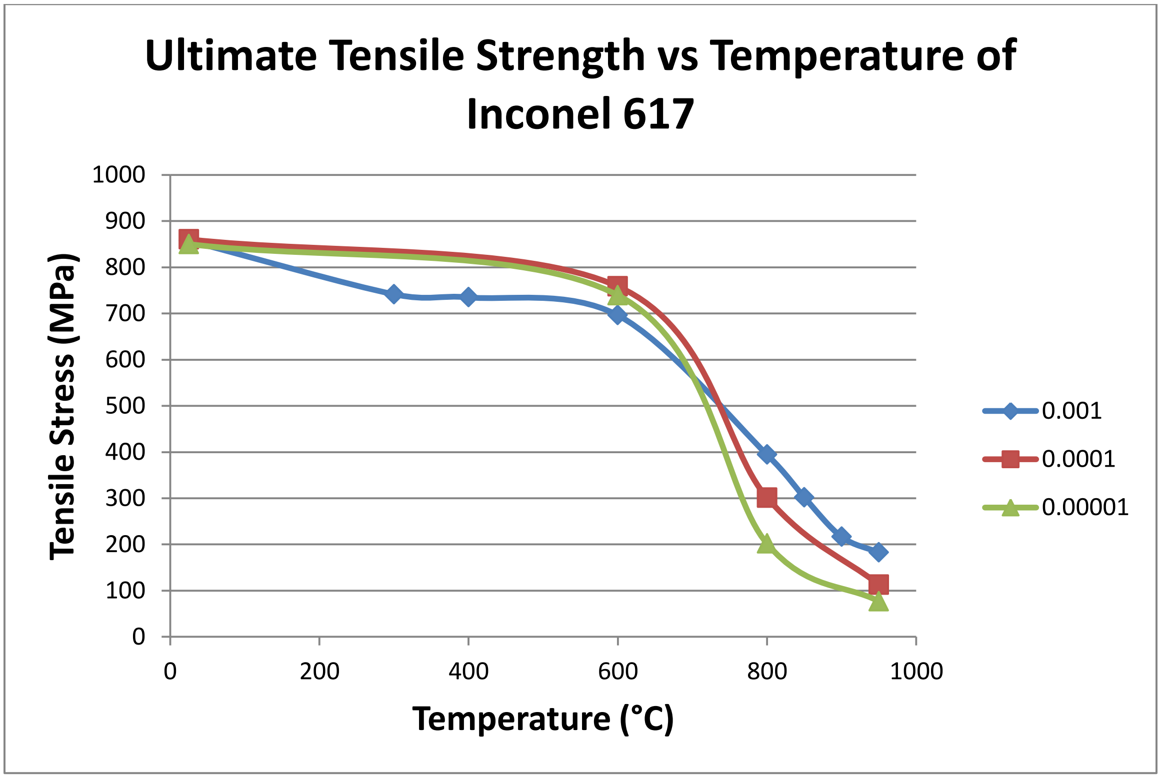

Figure 4.7 Tensile strength as a function of temperature of Inconel 617

As seen above in Figure 4.7 there is a gradual decrease in UTS up until about 600 °C. At room temperature until 600 °C, the material continually work hardens and the UTS is met just before fracture. Following this temperature there is a sharper decline in UTS up to the temperature of 950 °C. At higher temperatures the YS and UTS converge so that the UTS is met very early in the stress-strain curve. This is due to the softening caused by recovery and recrystallization. It is in the transition temperature regime from 600 °C to 800 °C when the dominant mechanism changes from hardening to softening. At temperatures below 600 °C, the dislocations caused by work hardening accumulate and interact with each other and DSA plays a critical role in deformation. The gradual decrease in UTS is a result of recovery as dislocations of opposite sign meet, cross-slip and annihilate each other. At temperatures above 600 °C, recrystallization begins to come into effect. As new grains nucleate, dislocations are annihilated, leading to a crystal structure with new, strain-free grains.

b) Strain Rate Effect:

Strain rate does not play as large of a role in the UTS of a material. As seen in Figure 4.7, the UTS is fairly constant from room temperature to 600 °C. The stress-strain curves of these materials shown in Chapter 3 show similar curve behavior at every strain rate. At the highest temperature of 950 °C, the UTS converges to meet the YS which was discussed in the previous section.

800 °C is a temperature of interest as different curve behavior occurs at different strain rates. As seen in Figure 4.8, the UTS at 800 °C increases following a logarithmic trend line. When strained at 10^{-3} s^{-1}, there is a significant hardening region before the alloy begins to soften after 5% strain. This is an indication that the DSA is the dominant mechanism to a point, before recrystallization begins to govern the deformation. However, at the slower strain rate the alloy reaches its yield strength and immediately begins to soften, indicating that DRX becomes the dominant mechanism. At the slower strain rates of 10^{-4} and 10^{-5} s^{-1}, softening ensues throughout deformation due to the

recrystallization. The further discussion of this process is presented in subsequent sections.

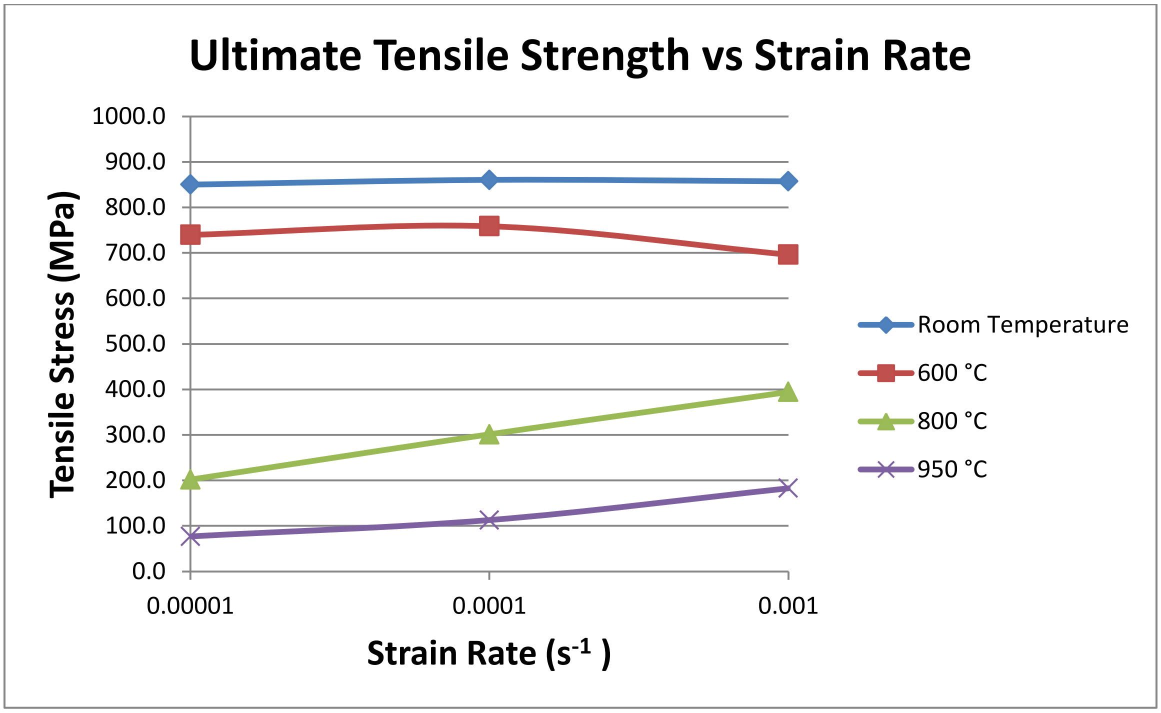

Figure 4.8 Ultimate tensile strength as a function of strain rate of Inconel 617

4.1.3 Total Elongation

a) Temperature Effect:

Ductility of a material is strongly influenced by the deformation temperature. Again ductility is highly dependent on the dislocation density because dislocations allow crystal planes to slip rather than fracture when undergoing an external stress. Dislocations carry the plastic deformation and in an FCC metal dislocation motion requires much less energy than to fracture the material, which requires the simultaneous breaking of bonds of an atomic plane.

Oddly there is no simple relationship between temperature and the elongation of the two alloys. Regardless of strain rate elongation is nearly uniform from room temperature up to 600 °C, as seen in Figure 4.9. Between 800 to 950 °C there is a drop in total elongation. In this temperature regime recrystallization is the dominant mechanism. Because recrystallization is a local process the strain is concentrated in a particular area of the material. The localized strain results in a soft spot in the material which will eventually be the point of fracture.

Interestingly, there is a significant increase in total elongation between 600 to 800 °C. This increase in total elongation somehow coincides with the YSA. 800 °C is a transition temperature when the softening and work hardening begin to balance each other, as suggested by the stress-strain curve at 10^{-3} s^{-1}. At this temperature the large amount of dissolution and reprecipitation provides obstacles for dislocations. At the same time grains are beginning to recrystallize which would annihilate dislocations. It may be that thermally assisted climb is occurring at this temperature, allowing dislocations to continue their motion and for the alloy to deform plastically. The temperature dependence of the total elongation in Inconel 617 and Haynes 230 deserves further analysis. In the literature, trends reported for 617 are not consistent with each other.

In a study carried out by Chomette et al. they found similar values for YS and UTS in Inconel 617 [43]. YSA was observed in the same temperature regime; however the total elongation reached a minimum at this point, followed by a significant increase at temperatures above 900 °C. Abd El-Azim reported values total elongation in Inconel 617 at 800-950 °C. At slower strain rates the total elongation decreased as the temperature increased, while faster strain rates produced a larger elongation with increasing temperature [44]. Finally, Rahman et. al reported both a decrease in YS, as well as a decrease in total elongation between the temperatures of 600-800 °C [11]. None of the studies mentioned above offered an explanation to what controlled the ductility of alloy 617.

Also, in their study of nickel superalloys, Kim et. al found that their alloys displayed the same YSA phenomena as seen in this study, however this coincided with a decrease in elongation [29]. They reported that the formation of microtwins impeded dislocation motion in the temperature of interest, which hardened the material, but at the same time reduced the ductility as slip could not occur. Zhao et al. observed the same phenomena when working with fine-grained copper [45]. They suggested that the high twin density and high density of high angle grain boundaries effectively block the dislocations and prevented them from annihilating. Evidence of extensive twinning was not found in the TEM and SEM analysis of our samples.

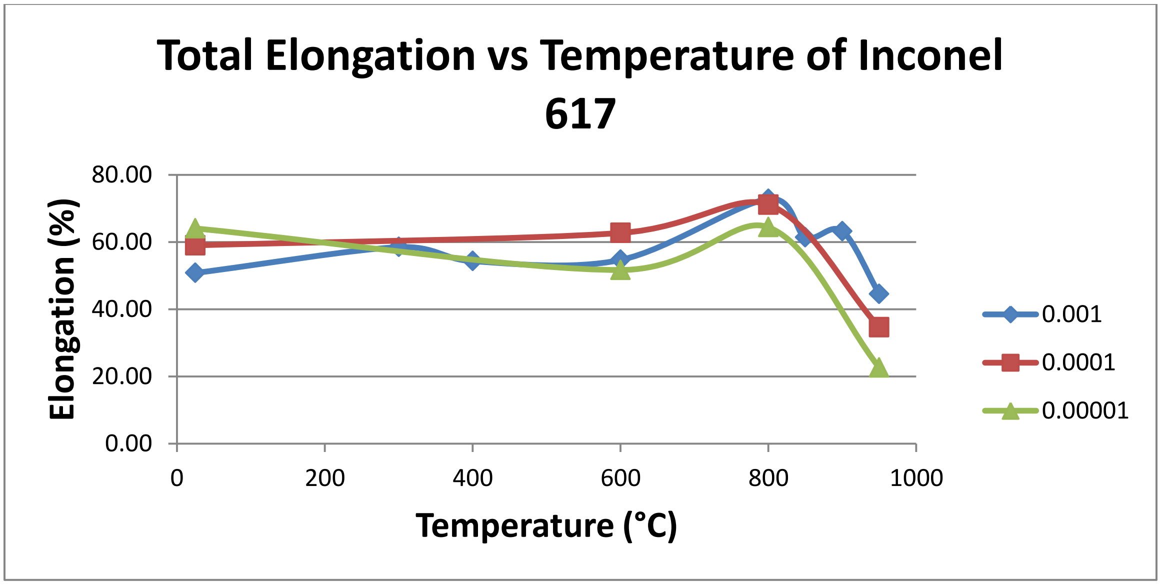

Figure 4.9 Elongation as a function of temperature of Inconel 617

b) Strain Rate Effect:

As seen in Figure 4.10 the elongation decreased with a slower strain rate at the high temperatures of 800 °C and 950 °C. At the higher temperatures the increased thermal energy aids even more in dislocation motion by causing dislocation climb, and could explain why the total elongation increases.

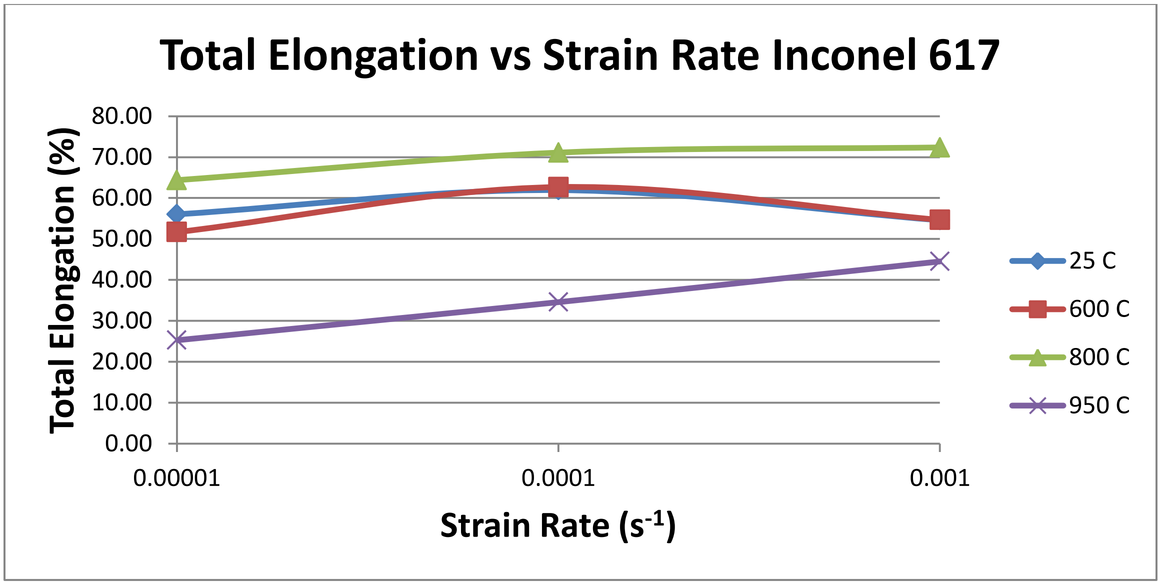

Figure 4.10 Elongation as a function of strain rate for Inconel 617

4.2 Microstructure

Overall, Haynes 230 retains much more of its initial microstructure than Inconel 617. Even after deformation at high temperatures, several large carbides still remain and can be seen oriented along the rolling direction as seen in Figure 4.11a, as opposed to Inconel 617 seen in Figure 4.11b. Such differences can be explained by the major alloying elements in each material. Haynes 230 primarily contains tungsten and molybdenum rich carbides while Inconel 617 forms chromium and molybdenum rich carbides. In the temperature range of interest (600-950 °C) tungsten has a solubility limit of 11-12 at% in nickel compared to chromium which has a solubility limit of 32-43 at% in nickel [46, 47]. As noted in section 3.2 the makeup of both alloys is some form of a nickel-iron matrix. Because of the much lower solubility limit of tungsten in nickel it is less likely for the original carbides to dissolve into the nickel solution and diffuse to form new carbides. Another factor is the diffusivity of the two metals in nickel. At 1.4 cm^2/s, tungsten has a lower diffusion coefficient through nickel than chromium whose value is 1.9 cm^2/s [48, 49]. Thus chromium atoms can migrate more freely throughout the matrix and interact to form more new carbides. Chromium atoms also have the ability to move farther away from the original carbide causing precipitates to be spaced more evenly throughout the alloy. The last factor which may come into play is the melting temperatures of tungsten carbide and chromium carbide. Because tungsten carbide melts at a much higher temperature (2870 °C) than chromium carbide (1895 °C) the diffusion/dissolution process should begin at a higher temperature. Combined with tungsten carbides extreme hardness it suggests that these carbides would remain in their original state at lower temperatures. A combination of these three factors leads to less dissolution and reprecipitation of $M_{23}C_6$ carbides in Haynes 230.

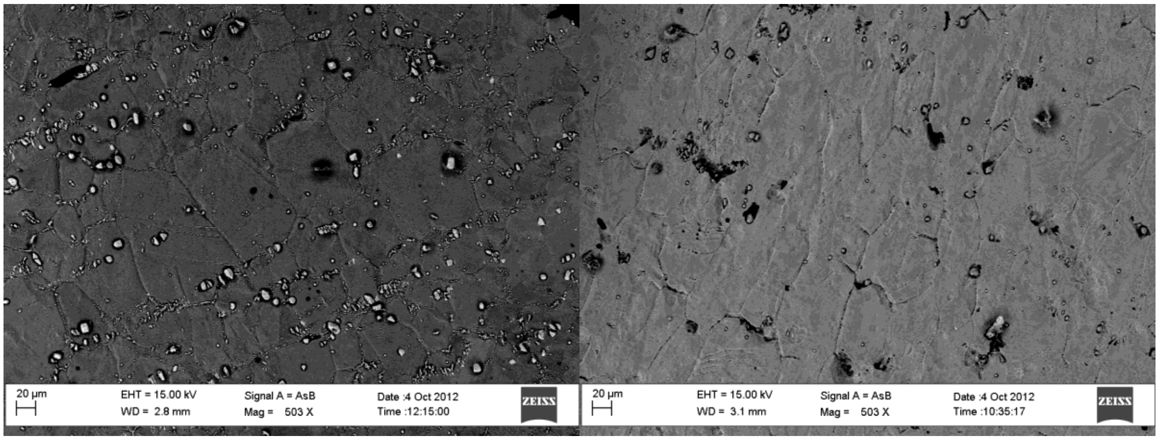

Figure 4.11 SEM micrograph of a) Haynes 230 and b) Inconel 617 after deformation at 800 °C and 10^{-5} s^{-1}

It is interesting to note that while Haynes seems to retain more of its initial microstructure, especially at lower temperatures regarding the precipitates, the mechanical properties of the alloy are very close to those of Inconel 617 at every test condition, as reported in previous sections; the main difference being the inferior elongation of Haynes 230 at each temperature.

4.3 Serrated Yielding

Deformation behavior of Inconel 617 and Haynes 230 at elevated temperatures showed the onset of serrated flow at a critical temperature of 300 °C. Serrations reached a maximum amplitude at 600 °C. Different deformation processes are generally associated with stress serrations depending on both temperature and strain rate. Two mechanisms associated with these serrations in the stress curve are dynamic strain ageing (DSA) and recrystallization and they will both be explored in the following sections.

4.3.1 Serration Type

Hong et. al observed similar oscillations in tensile tests conducted on Inconel 600 in the temperature range of 150-700 °C. In their study they identified four different types of oscillations as seen below in Figure 4.12 [50]. The A1 type of oscillation consisted of a periodic rise and drop of stress with small amplitude. The A2 type of serration had a more continuous rise and drop in serration with a larger amplitude. The B type serration was a successive oscillation of stress while the C type was characterized by irregular stress drops. Each oscillation corresponded to a different temperature range, and accordingly was reached at different activation energies.

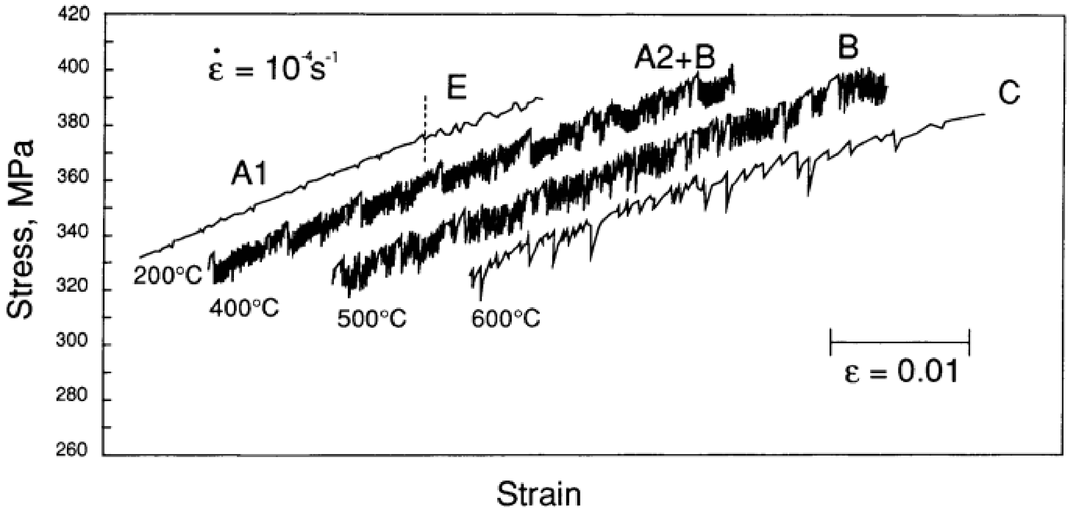

Figure 4.12 The four different types of oscillations observed by Hong in Inconel 600

In this study two types of serrations were observed in the intermediate temperatures: type B and type C. Type B serrations occurred at higher strain rates and continued throughout the entirety of the tensile test. The stress oscillations hovered around the general level of the curve and were as large as 25 MPa. However, at slower strain rates type B and type C serrations were observed. At the beginning of the test until roughly 25% strain type B serrations existed which were then followed by type C serrations until the end of the test. Both types were roughly 25 MPa but the type C serrations were characterized by sudden drops from the existing curve. Accompanying all serrations there was an audible clicking sound which coincided with each drop in the curve. Many studies have observed macroscopic deformation bands linked with the PLC which propagate along the gauge length in a continuous manner [51]. However, no such bands were observed in this study. Digital Imaging Correlation experiments may help visualize such bands if they actually happen during testing of Inconel 617 and Haynes 230.

Previous studies have been conducted which reported similar curve behavior and oscillation characteristics to the current study [40, 43, 52]. These studies report the mechanical properties and the presence of serrations but do not fully explain the mechanisms causing the serrations.In contrast to these previous studies, Rahman et. al reported jerky flow in Inconel 617 at the temperatures of 600 °C and 800 °C [11]. However, the flow curve lacked the regularity of serrations observed in this study as can be seen in Figure 4.13. Also, at 800 °C all of the curves have a hardening region (regardless of strain rate), unlike the flow stress curves in this study which showed a continuous softening at strain rates of 10^{-4} and 10^{-5} s^{-1}. While the temperatures and strain rates between the two studies are the same, Rahman et al. used a bulk sample for tensile tests while this study used Inconel 617 in the form of a sheet.

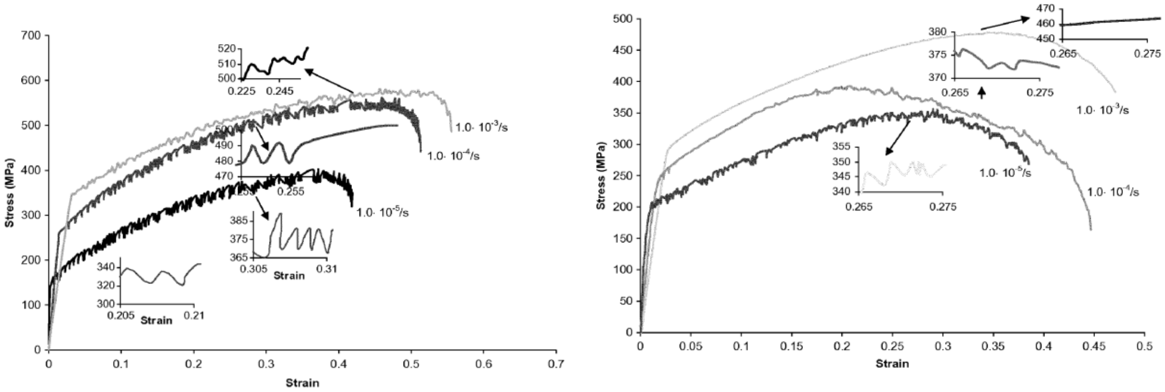

Figure 4.13 Stress-strain curves of Inconel 617 reported by Rahman at a) 600 °C and b) 800 °C

4.3.2 Dynamic Strain Ageing

The temperature and the strain rate dependence of serrated yielding as observed in both alloys indicate that the DSA mechanism is controlled by a thermally activated process. In other words it is a diffusion controlled process as suggested by Kocks and van den Beukel [30, 32, 53].

Tensile tests conducted at intermediate temperatures showed a saw tooth shape and occurred during the strain hardening process; serrations were linked to discontinuous slip as diffusing solute atoms pin dislocations in place, a mechanism supported in the literature [11, 53, 54]. As described in section 1.3.4 the two most widespread models explaining DSA are DSI and DDI. Both of these models can be evidenced in this study as TEM micrographs reveal precipitates surrounded by dislocations as well as dislocation forests seen in Figure 4.14. Based on the DDI model, solute atoms form on forest dislocations and then drain by pipe diffusion to the mobile dislocations which are temporarily arrested at the forest locations. Eventually enough stress is applied for dislocations to break free from these obstacles, only to be locked by further solute atoms. This locking and unlocking process manifests itself as serrations in the stress-strain curve. Features of DSA include serrated yielding, negative strain rate sensitivity, peaks in the UTS-temperature curves, and plateaus in the elongation-temperature curves [55, 56]. Serrated yielding has been mentioned throughout this study, and as noted in the previous section there is a plateau in the elongation-temperature curve at temperatures below 600 °C.

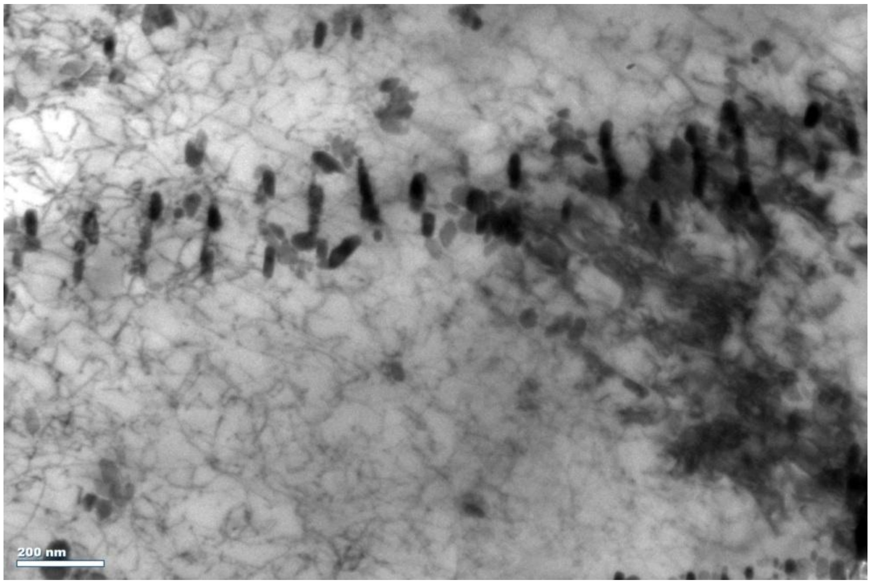

Figure 4.14 TEM micrograph of forest dislocations surrounding fine carbide precipitates in Haynes 230 after deformation at 800 °C

Figure 4.15 shows traces of multiple slip bands activated during deformation in Inconel 617 at 600 °C and 10^{-4} s^{-1}. Such slip band configurations were typical in low to intermediate temperatures, as slip and cross-slip of dislocations happens along these bands.

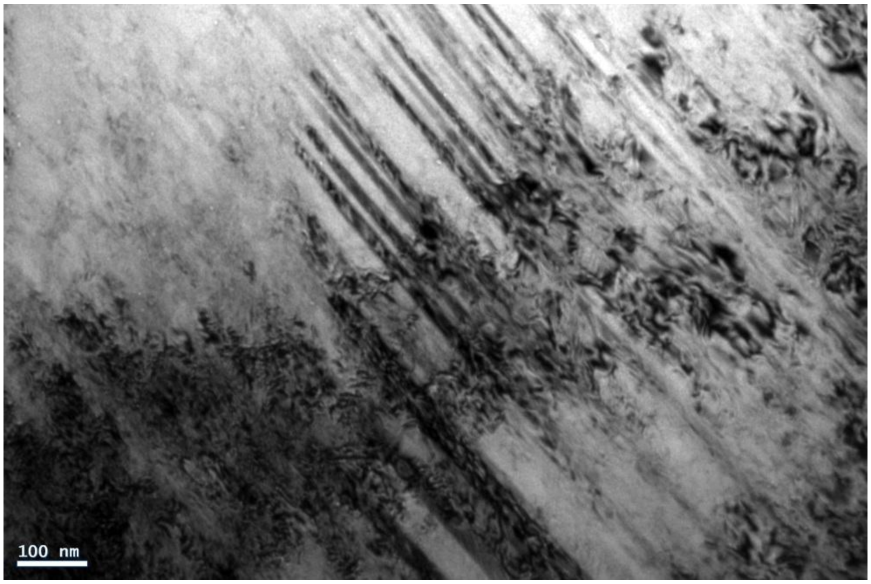

Figure 4.15 TEM micrograph showing traces of slip bands in Inconel 617 deformed at 600 °C and 10^{-4} s^{-1}

DSA most likely only occurs in this intermediate temperature range because at higher temperatures there is enough thermal energy for dislocations to overcome the immobile barriers and more importantly recrystallization also becomes the dominant mechanism at higher temperatures as subgrains begin to nucleate at grain boundaries, seen in Figure 4.16.

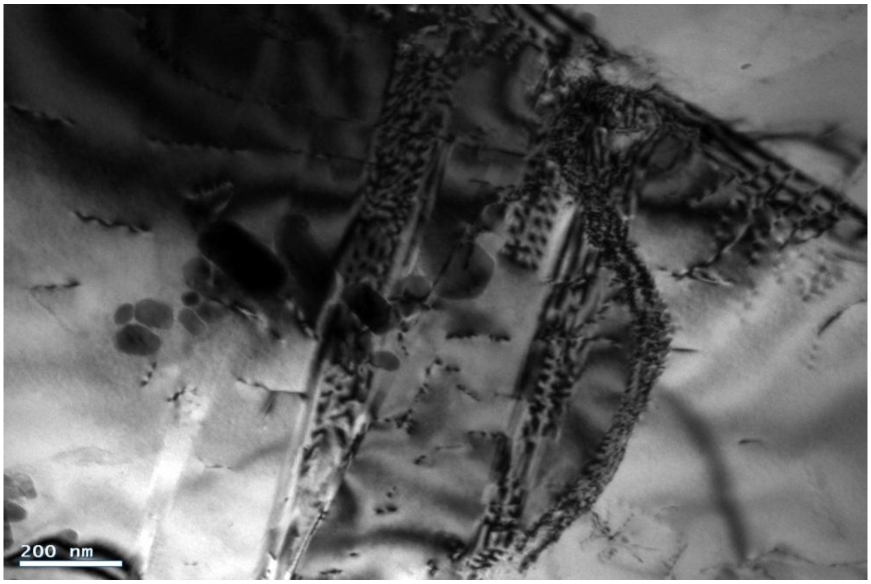

Figure 4.16 TEM micrograph showing subgrain boundary formation in Haynes 230 deformed at 600 °C and 10^{-3} s^{-1}

Many studies have suggested that pipe diffusion of solutes occurs while dislocations are blocked by precipitates [57-60]. As the solutes diffuse along the dislocations they aggregate to form precipitates in parallel bands and remain in this position even after dislocations have migrated. Figure 4.17 shows a TEM micrograph from this study in which precipitates have formed in areas formerly occupied by dislocation bands. The precipitates appear in neatly organized rows parallel to each other, where dislocations were previously in a band. Figure 4.18 shows the same image but at a higher magnification to highlight the forest dislocations which still remain immobilized.

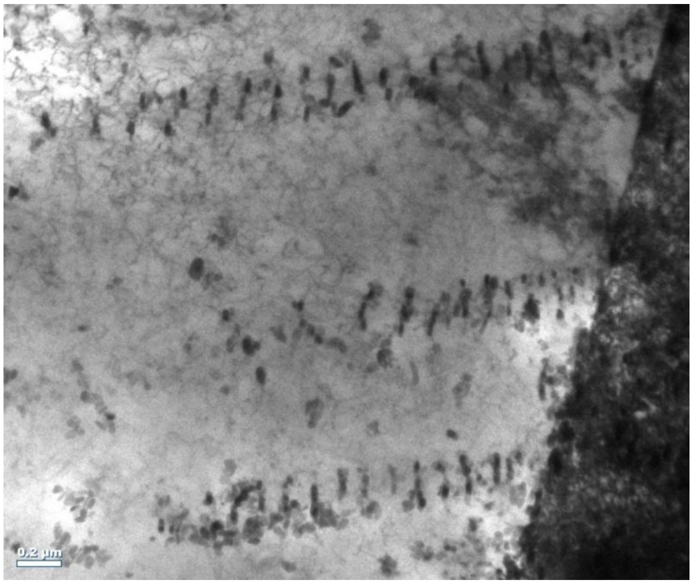

Figure 4.17 TEM micrograph of Haynes 230 deformed at 800 °C and 10^{-3} s^{-1}. Precipitates align to form rows at positions previously occupied by dislocations.

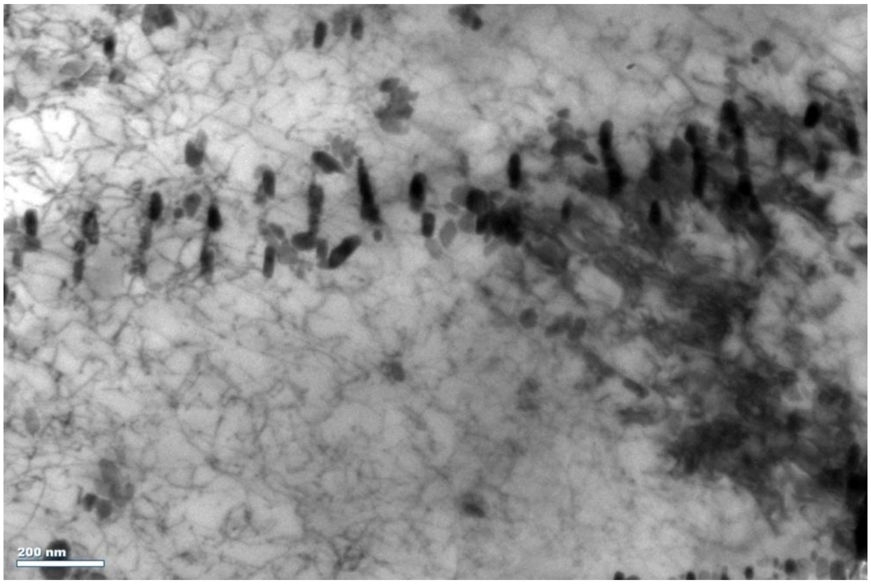

Figure 4.18 Close up of previous TEM micrograph showing forest dislocations in the background

Others have suggested that a long range stress field due to dislocations causes synchronized movements of these bands of dislocations [57]. Such synchronization in the movement causes the hardening succeeded by the relaxation period when the entire dislocation band moves as one. It is also this long range stress field which gives rise to the negative strain rate sensitivity phenomena.

In a study conducted by El-Azim he found DSA caused serrated flow at 300 °C and 400 °C in the ferrite stainless steel Incoloy alloy MA956. Based on the previous models he determined the DSA was due to the interaction of carbon and nitrogen solute atoms [61]. Chen and Chaturdevi also observed the serrated stress-strain behavior in Inconel 718 at 200-545 °C. They reported the serrations involve the segregation and depletion of interstitial elements to and from depletion cores [62].

4.3.3 Dynamic Recrystallization

The other deformation mechanism responsible for serrations in the flow curve of Inconel 617 and Haynes 230 at the highest temperatures is dynamic recrystallization. Dynamic recrystallization is a softening mechanism which occurs in metals at high temperatures. Dislocations are eliminated by the migration of recrystallized high angle grain boundaries causing the material to soften [5]. According to this mechanism, the recrystallization nuclei form during straining, and continue to grow when deformation is interrupted.

In this study softening occurred at both 800 °C and 950 °C. At the lower temperature of 800 °C, the softening was a function of strain rate. At the faster strain rate of 10^{-3} s^{-1}, there was a short hardening region up until 5% strain followed by a relatively smooth softening region. At slower strain rates, the curve was characterized by continuous softening following yield with sinusoidal serrations present throughout.

However, at 950 °C, softening occurred during all tensile tests but serrations only occurred during the two slower strain rates of 10^{-4} and 10^{-5} s^{-1}. The amplitude of the serrations increased as the strain rate decreased, while the period decreased with decreasing strain rate. Both the softening character and the sinusoidal oscillations observed in this study are indicative of recrystallization. New grains with new orientations are formed following the first drop in stress and these new high-angle boundaries facilitate further recrystallization [63].

Li et. al observed similar serrated flow in compression tests conducted on Inconel 625 in the temperature range 900-1200 °C. By means of EBSD they determined that full recrystallization occurred at 1150 °C at a strain of 0.7 [14]. Petkovic et. al determined that there was a correlation between temperature and the occurrence of sinusoidal serrations due to recrystallization in carbon steel. As is evidenced in Figure 4.19, flow serrations become more prevalent with increasing temperature [15]. Luton et. al showed that transition from periodic serrations to continuous behavior is associated with strain rate. A low strain rate produces cyclic sinusoidal serrations during recrystallization, consistent with the periodicity of softening and hardening [12]. Coryell again reinforced these observations with his study of Incoloy alloy 945 in the temperature range of 950-1150 °C. During compression tests run at various temperatures he reported the onset and extent of recrystallization increased with increasing temperatures and decreasing strain rates [13].

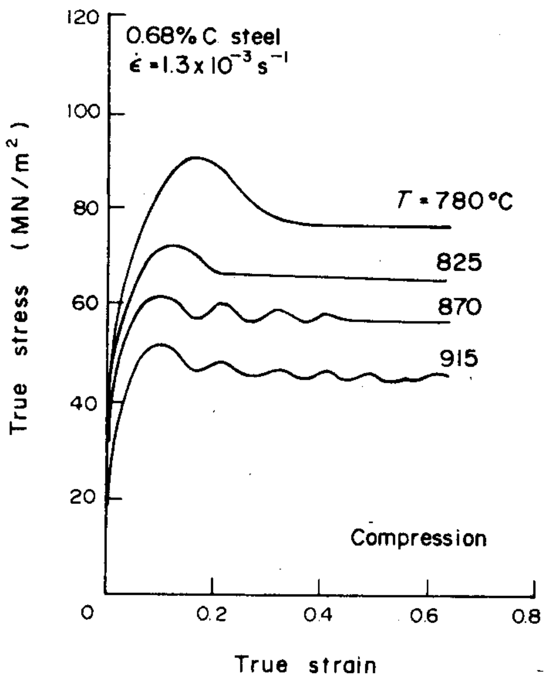

Figure 4.19 Stress serrations reported by Petkovic in carbon steel

SEM images of the Inconel 617 deformed at 950 °C and 10^{-3} s^{-1} are shown below in Figure 4.15, are inconclusive as to whether recrystallization has occurred because grain boundaries are difficult to identify. However, the grain boundaries become less distinct than those observed at lower temperatures, indicating that the original grain boundaries are no longer present and that recrystallization has occurred. In order to accurately identify and measure the recrystallized grains electron backscatter diffraction (EBSD) would be necessary. With the aid of TEM new, high-angle subgrain boundaries can be identified more directly due to the change in contrast between the newly nucleated grains. Notice in Figure 4.20 the subgrain boundary in which carbides have reprecipitated. In Figure 4.21 TEM micrographs show grain refinement due to dynamic recrystallization in Inconel 617 tested at 950 °C at 10^{-3} s^{-1}.

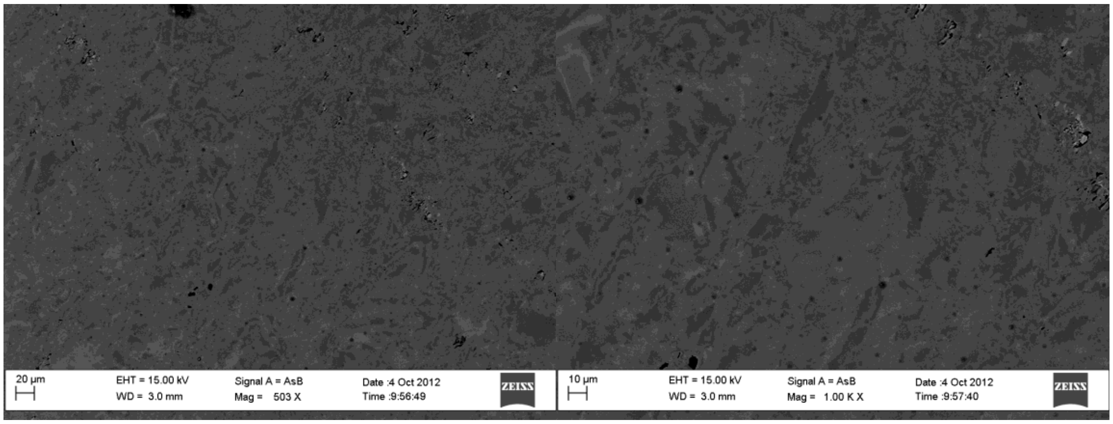

Figure 4.20 SEM images of less distinct grain boundaries in Inconel 617 deformed at 950 °C and 10^{-3} s^{-1}

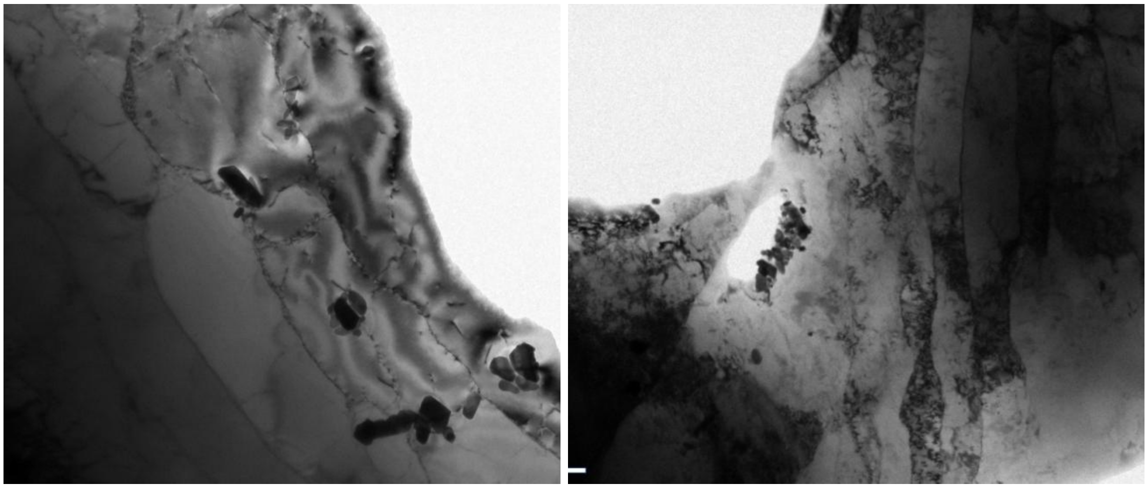

Figure 4.21 TEM micrograph showing grain refinement with low dislocation density as result of dynamic recrystallization in Inconel 617 deformed at 950 °C and 10^{-3} s^{-1}

The mechanisms causing dynamic recrystallization are primarily grain and twin boundary bulging [64]. Such grain bulging was observed in post-test examination of fractured samples as shown in Figure 4.22. This bulging area then acts as a nucleation source for additional recrystallized grains. The bulging mechanism is consistent with literature in which materials with low stacking fault energy and large initial grain size experience discontinuous DRX. Dudova proposed that grain boundary bulging was the dominant mechanism for recrystallization above 0.5 T_m for a Ni-20%Cr alloy [65]. The migration of grain boundaries leads to the formation of nuclei which then grow out and consume an area of the deformed matrix and eventually forming a recrystallized grain. This process repeats itself as the original grains are continually deformed until complete recrystallization has occurred. Figure 4.23 presents a TEM micrograph showing grain refinement with the formation of subgrains with serrated subgrain boundaries in Haynes 230 deformed at 950 °C and 10^{-4} s^{-1}.

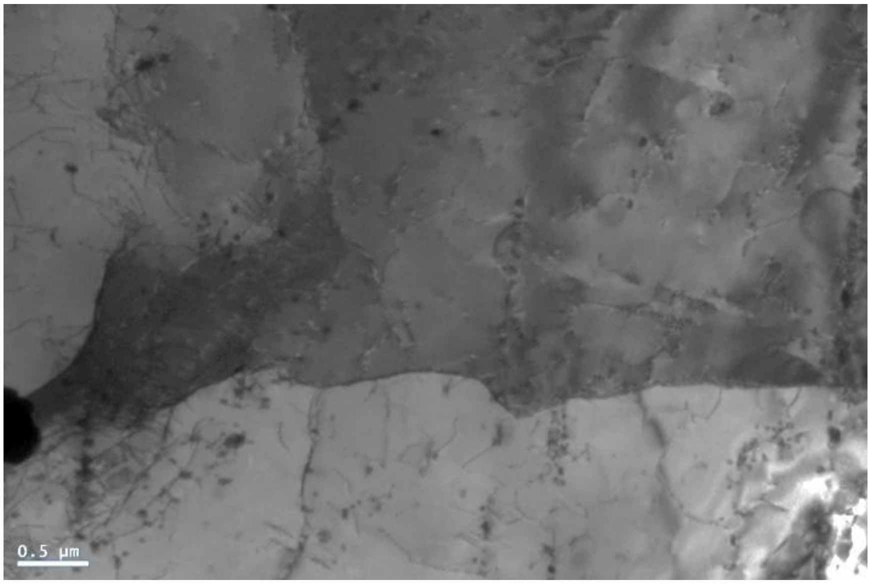

Figure 4.22 TEM micrograph showing bulging grains in Inconel 617 deformed at 950 °C and 10^{-3} s^{-1}

The bulging process described above also leads to GBS. Grains boundaries become wavy rather than maintaining their straight edges. As mentioned in chapter 1, GBS can be linked to recrystallization as the bulging grain boundaries provide sites for the dislocations to realign into new, defect-free grains.

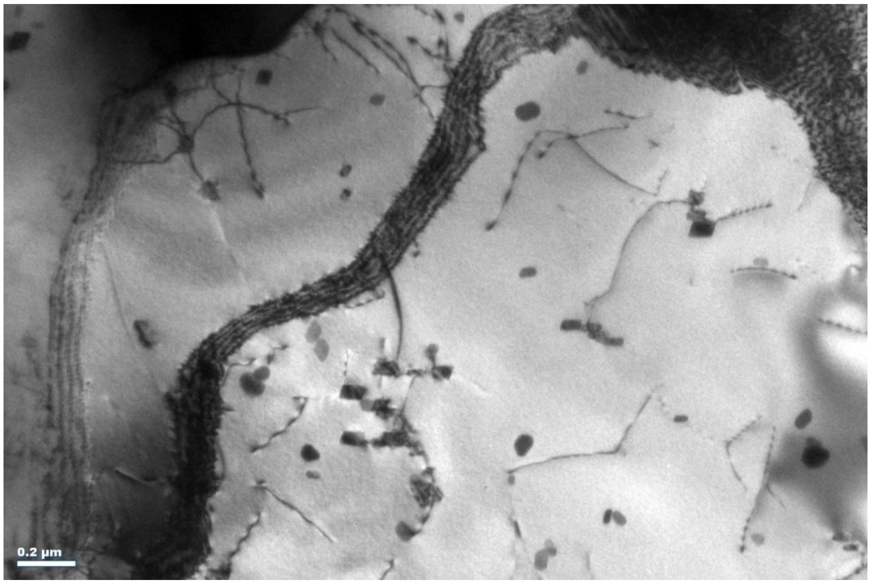

Figure 4.23 TEM micrograph showing grain refinement with formation of subgrains with serrated subgrain boundaries in Haynes 230 deformed at 950 °C and 10^{-4} s^{-1}

CHAPTER 5

Summary and Conclusions

All of the original goals discussed in the first chapter were met during this study. This chapter addresses these objectives and discusses the conclusions with respect to each project goal.

1. Both strain rate and temperature had a significant impact on the mechanical properties of Haynes 230 and Inconel 617. In the temperature range of 600-800 °C, the phenomenon of YSA was observed. The increase in YS with increasing temperature could be explained by dissolution of carbides which provided obstacles to dislocation motion. In the same temperature regime, an increase in total elongation was also observed. Strain rate played little importance at low and intermediate temperatures. However, upon reaching 800 °C a faster strain rate was characterized by a period of strain hardening while a slower strain rate resulted in softening throughout deformation. At the higher temperatures of 800 and 950 °C, YS, UTS, and final elongation all decreased with a slower strain rate. A comparison of the mechanical properties of Haynes 230 and Inconel 617 were very similar. The YS and UTS of both alloys were very similar, but they varied in the final elongation. Inconel 617 was

2. consistently more ductile than Haynes 230 regardless of temperature or strain rate.
3. The flow behavior of Haynes 230 and Inconel 617 was investigated at room temperature, 600 °C, 800 °C, and 950 °C at strain rates between 10^{-3}-10^{-5} s^{-1}. At temperatures up to 600 °C significant strain hardening took place after yield until rupture. The strain hardening was systematically accompanied by large saw-tooth serrations from 300-600 °C. At 800 °C and 10^{-3} s^{-1} a small region of strain hardening occurred along with stress serrations followed by smooth softening, plastic flow until fracture. At lower strain rates the strain hardening section was suppressed, indicating that 800 °C was a transition temperature. At higher temperatures of 950 °C, no strain hardening was observed regardless of the strain rate; the flow behavior of both alloys softened right after yield until rupture. Also, strain softening occurred accompanied by sinusoidal oscillations in the stress-strain curve, regardless of strain rate.
4. Stress serrations associated with hardening (sawtooth type) in the stress-strain curves were associated with DSA. Discontinuous flow occurs from the pinning of dislocations by solute atoms, and the subsequent unlocking of these dislocations due to an increase in stress. Serrations associated with softening of the stress-strain curve (sinusoidal type) were due to dynamic recrystallization.
5. Haynes 230 and Inconel 617 displayed remarkably similar microstructure. Both metals are nickel based austenitic superalloys with coarse grains

between 35-45 µm in size. The as-received material contained large M_6C carbides located primarily along grain boundaries, but also included intra-granular precipitates. These large carbides dissolved and reprecipitation occurred into small $M_{23}C_6$ carbides. The main difference between the two is that molybdenum and chromium constituted the carbides in Inconel 617 while tungsten made up the carbides in Haynes 230. Upon heating to temperatures above 600 °C dynamic recrystallization occurred which resulted in smaller grains and texture changes, as evidenced by XRD of deformed samples. At temperatures above 900 °C the large grains recrystallized into much smaller grains.

CHAPTER 6

Future Work

This work was performed to gain a better understanding of the mechanical properties and microstructural behavior of the two nickel superalloys Haynes 230 and Inconel 617. With the general understanding that this study provides further work can now be done on the two alloys to develop models describing their deformation characteristics.

The experiments in this study primarily consisted of uninterrupted tensile tests. In order to gain a better understanding of the dynamics of DSA and recrystallization, interrupted tests could provide microscopy information at different points of strain.

Secondary peaks in the XRD spectra obtained on the bulk samples could not be indexed with certainty due to convolution of the peaks and other factors. Further analysis of these peaks would be necessary in order to identify the peaks. Concerning the extraction of precipitates, the material did dissolve in aqua regia, but the alloying elements formed chlorides which further clouded the results. To correctly identify the carbides an acidic solution which is non-reactive with tungsten, chromium, and molybdenum is necessary in order to preserve the precipitates.

Another technique which would be useful in this study is Electron Backscatter Diffraction (EBSD). When the grains recrystallized at higher temperatures it was impossible to identify the grain boundaries with SEM imaging alone and TEM could only image very localized areas of the microstructure. EBSD has the capability to identify both high and low angle grain boundaries and would be a useful tool in verifying the amount of recrystallization which has taken place and the size of the recrystallized grains.

Both of these alloys are candidate materials for the IHX in a VHTR. In this case failure does not occur by simple tension, but rather as a result of prolonged creep. Thus, creep tests would naturally be the next step in determining the viability of these materials in a nuclear reactor. As suggested by the Generation IV Integrated Materials Technology Program, exposure to temperatures of 750 °C, 850 °C, 950 °C, and 1000 °C for 3000 hours should be conducted to observe the changes in microstructure that any candidate material would be likely to experience [66]. Furthermore, tests conducted in helium and nitrogen would provide results more fitting for a nuclear reactor as helium has been the suggested coolant in the VHTR.

References

1. Klarstrom, D.L. *The development of HAYNES 230 alloy*. in *Materials Design Approaches and Experiences. Proceedings of Symposium, 4-8 Nov. 2001*. 2001. Warrendale, PA, USA: TMS - Miner., Metals & Mater. Soc.
2. Rahman, S., et al., *Investigation of the secondary phases of alloy 617 by scanning Kelvin probe force microscope.* Materials Letters, 2008. **62**(15): p. 2263-6.
3. Cook, R.H., *Creep properties of Inconel-617 in air and helium at 800 to 1000C.* Nuclear Technology, 1984. **66**(2): p. 283-8.
4. Gorelik, S.S., *Recrystallization in metals and alloys*1981: Mir.
5. Sakai, T. and J.J. Jonas, *Dynamic recrystallization: mechanical and microstructural considerations.* Acta Metallurgica, 1984. **32**(2): p. 189-209.
6. Voter, A.F. and C. Shao Ping. *Accurate interatomic potentials for Ni, Al and Ni3Al*. in *Characterization of Defects in Materials Symposium, 1-2 Dec. 1986*. 1987. Pittsburgh, PA, USA: Mater. Res. Soc.
7. Haasen, P., *Physical Metallurgy*1978, Cambridge: Cambridge University Press.
8. Cotterill, P. and P.R. Mould, *Recrystallization and grain growth in metals*1976: Surrey University Press.
9. Urdanpilleta, M., J.M. Martinez-Eznaola, and J.G. Sevillano, *Strain rate sensitivity of superplastic Inconel 718.* Materials Transactions, 2005. **46**(7): p. 1711-19.
10. Hu, H.E., et al., *Microstructure characterization of 7050 aluminum alloy during dynamic recrystallization and dynamic recovery.* Materials Characterization, 2008. **59**(9): p. 1185-9.
11. Rahman, M.S., et al., *Characterization of high temperature deformation behavior of INCONEL 617.* Mechanics of Materials, 2009. **41**(3): p. 261-70.
12. Luton, M.J. and C.M. Sellars, *Dynamic recrystallization in nickel and nickel-iron alloys during high temperature deformation.* Acta Metallurgica, 1969. **17**(8): p. 1033-43.
13. Coryell, S.P., K.O. Findley, and M.C. Mataya. *Flow behavior of superalloy 945 during high temperature deformation*. in *TMS 2010. 139th Annual Meeting & Exhibition. Materials Processing and Properties, 14-18 Feb. 2010*. 2010. Warrendale, PA, USA: Minerals, Metals & Materials Society (TMS).
14. Li, D., et al., *The microstructure evolution and nucleation mechanisms of dynamic recrystallization in hot-deformed Inconel 625 superalloy.* Materials and Design, 2011. **32**(2): p. 696-705.
15. Petkovic, R.A., M.J. Luton, and J.J. Jonas, *RECOVERY AND RECRYSTALLIZATION OF CARBON STEEL BETWEEN INTERVALS OF HOT WORKING.* Canadian Metallurgical Quarterly, 1975. **14**(2): p. 137-145.

16. Jiang, L., et al., *The effect of M23C6 carbides on the formation of grain boundary serrations in a wrought Ni-based superalloy.* Materials Science and Engineering A, 2012. **536**: p. 37-44.
17. Kim, K.J., H.U. Hong, and S.W. Nam, *A study on the mechanism of serrated grain boundary formation in an austenitic stainless steel.* Materials Chemistry and Physics, 2011. **126**(3): p. 480-3.
18. Suh, D.-W., et al., *Serration of grain boundary in Ni-30Fe alloy through high temperature deformation.* ISIJ International, 2002. **42**(9): p. 1026-1032.
19. Tanaka, M., *Improvement of creep-rupture properties by serrated grain boundaries in high-tungsten cobalt-base superalloys.* Zeitschrift fur Metallkunde, 1993. **84**(1): p. 51-6.
20. Cahn, R.W., P. Haasen, *Physical Metallurgy*. Vol. III. 1996, Amsterdam: Elsevier Science.
21. Clark, D.S., *Physical Metallurgy for Engineers*1952, Princeton: D. Van Nostrand Company, Inc.
22. Dieter, G.E., *Mechanical Metallurgy*. Metallurgy and Metallurgical Engineering Series, ed. R.F. Mehl1961, York: The Maple Press Company.
23. Reed-Hill, R.E., *Physical Metallurgy Principles*1964, Princeton: D. Van Nostrand Company, Inc.
24. Aken, D.V. *Engineering Concepts: Formation of Annealing Twins*. 2000 [cited 2012 June].
25. Sourmail T., P.O., G. Hopkin. *Annealing Twins*. Metals and Alloys [cited 2012 June].
26. Mahajan, S., et al., *Formation of annealing twins in f.c.c. crystals.* Acta Materialia, 1997. **45**(6): p. 2633-8.
27. Meyers, M.A. and L.E. Murr, *A model for the formation of annealing twins in FCC metals and alloys.* Acta Metallurgica, 1978. **26**(6): p. 951-62.
28. Pande, C.S., M.A. Imam, and B.B. Rath, *Study of annealing twins in FCC metals and alloys.* Metallurgical Transactions A (Physical Metallurgy and Materials Science), 1990. **21A**(11): p. 2891-6.
29. Kim, I.S., et al., *Anomalous deformation behavior and twin formation of Ni-base superalloys at the intermediate temperatures.* Materials Science and Engineering A, 2011. **528**(24): p. 7149-7155.
30. Beukel, A.v.d. and U.F. Kocks, *Strain dependence on static and dynamic strain-ageing.* Acta Metallurgica, 1982. **30**(5): p. 1027-1034.
31. Kubin, L.P., Y. Estrin, and C. Perrier, *On static strain ageing.* Acta Metallurgica et Materialia, 1992. **40**(5): p. 1037-44.
32. Mulford, R.A. and U.F. Kocks, *The effect of solute on the obstacle profiles for dislocation intersection and solution strengthening in Ni alloys.* Scripta Metallurgica, 1979. **13**(8): p. 729-32.
33. Tawancy, H.M., D.L. Klarstrom, and M.F. Rothman, *DEVELOPMENT OF A NEW NICKEL-BASE SUPERALLOY.* Journal of Metals, 1984. **36**(9): p. 58-62.
34. Materials, A.S.f.T.a., *2008 Annual Book of ASTM Standards*, in *Standard Test Methods for Tension Testing of Metallic Materials*2008: Baltimore, MD. p. 69.
35. Conte, M., et al., *Aqua regia activated Au/C catalysts for the hydrochlorination of acetylene.* Journal of Catalysis, 2013. **297**: p. 128-136.

36. Metals, S., *Inconel Alloy 617 Data Sheet*, 2005, Special Metals Corporation.
37. International, H., *Haynes 230 Alloy Data Sheet*, H. International, Editor 2009: Kokomo.
38. Mankins, W.L., J.C. Hosier, and T.H. Bassford, *Microstructure and phase stability of INCONEL alloy 617.* Metallurgical Transactions A (Physical Metallurgy and Materials Science), 1974. **5**(12): p. 2579-90.
39. Baker, I. and E.P. George. *A model for the yield strength anomaly in FeAl*. in *High-Temperature Ordered Intermetallic Alloys VII. Symposium, 2-5 Dec. 1996*. 1997. Pittsburgh, PA, USA: Mater. Res. Soc.
40. Marthandam, V. and A.K. Roy. *Tensile deformation of Alloy 617 at different temperatures*. in *2007 ASME Pressure Vessels and Piping Conference, PVP 2007, July 22, 2007 - July 26, 2007*. 2008. San Antonio, TX, United states: American Society of Mechanical Engineers.
41. Roy, A.K. and A. Venkatesh, *Evaluation of yield strength anomaly of Alloy 718 at 700-800C.* Journal of Alloys and Compounds, 2010. **496**(1-2): p. 393-8.
42. Alder, J.F. and V.A. Phillips, *Effect of strain rate and temperature on resistance of aluminum, copper, and steel to compression.* Institute of Metals -- Journal, 1954. **83**(Part 3): p. 80-86.
43. Chomette, S., *The effect of microstructural evolution on the nickel base alloys Inconel 617 and Haynes 230 at high temperature*, in *Material Science*2009, L'universite de Toulouse: Toulouse.
44. Abd El-Azim, M.E., Ennis P. J., Schuster H., Hammad F. H., Nickel H., *The Tensile Properties of Alloys 800H and 617 in the Range 20 to 950 C*, in *Nuclear Physics*1990, Julich: Julich.
45. Zhao, Y.-H., et al., *Simultaneously increasing the ductility and strength of ultra-fine-grained pure copper.* Advanced Materials, 2006. **18**(22): p. 2949-2953.
46. Kourtoukova, G.L., et al., *Design and tailoring of Ni-Sn-W composites for bonded abrasive applications.* Materials Science & Engineering A (Structural Materials: Properties, Microstructure and Processing), 2000. **A276**(1-2): p. 58-69.
47. Turchi, P.E.A., L. Kaufman, and L. Zi-Kui, *Modeling of Ni-Cr-Mo based alloys: Part I-phase stability.* CALPHAD: Computer Coupling of Phase Diagrams and Thermochemistry, 2006. **30**(1): p. 70-87.
48. K., M., S. H., and O. H., *Diffusion of Ni and W in Nickel-Tungsten Alloys (On the Relation between High-Temperature Creep and Diffusion in Nickel Base Solid Solutions).* J. Japan Inst. Metals, 1964. **28**: p. 197-200.
49. Wilcox, B.A. and A.H. Clauer, *Creep of dispersion-strengthened nickel-chromium alloys.* Metal Science Journal, 1969. **3**: p. 26-33.
50. Hong, S.H., et al. *Dynamic strain aging behaviour of Inconel 600 alloy*. in *Proceedings of Eighth International Symposium on Superalloys, 22-26 Sept. 1996*. 1996. Warrendale, PA, USA: TMS.
51. A. Benallal, T.B., A. Clausen, O. Hopperstad, *Dynamic Strain Aging, Negative Strain-Rate Sensitivity and Related Instabilities.* Technische Mechanik, 2003: p. 160-166.
52. Abd El-Azim, M.E., K.E. Mohamed, and F.H. Hammad, *The deformation characteristics of alloy 800H and alloy 617.* Mechanics of Materials, 1992. **14**(1): p. 33-46.

53. Mulford, R.A. and U.F. Kocks, *New observations on the mechanisms of dynamic strain aging and of jerky flow.* Acta Metallurgica, 1979. **27**(7): p. 1125-35.
54. Beukel, A.v.d., *Theory of the effect of dynamic strain aging on mechanical properties.* Physica Status Solidi A, 1975. **30**(1): p. 197-206.
55. Kubin, L.P., K. Chihab, and Y. Estrin, *The rate dependence of the Portevin-Le Chatelier effect.* Acta Metallurgica, 1988. **36**(10): p. 2707-18.
56. Kubin, L.P., K. Chihab, and Y. Estrin. *Nonuniform plastic deformation and the Portevin-le Chatelier effect*. in *Patterns, Defects and Microstructures in Nonequilibrium Systems. Applications in Materials Science. Proceedings of the NATO Advanced Research Workshop, 24-28 March 1986*. 1987. Dordrecht, Netherlands: Martinus Nijhoff.
57. Yilmaz, A., *The Portevin-le Chatelier effect: a review of experimental findings.* Science and Technology of Advanced Materials, 2011. **12**(6): p. 063001 (16 pp.).
58. Schlipf, J., *On the kinetics of static and dynamic strain aging.* Scripta metallurgica et materialia, 1994. **31**(7): p. 909-914.
59. Picu, R.C. and D. Zhang, *Atomistic study of pipe diffusion in Al-Mg alloys.* Acta Materialia, 2004. **52**(1): p. 161-171.
60. Springer, F., A. Nortmann, and C. Schwink, *A study of basic processes characterizing dynamic strain ageing.* Physica Status Solidi A, 1998. **170**(1): p. 63-81.
61. Abd El-Azim, M.E., *Effect of dynamic strain ageing on the deformation behavior of Incoloy alloy MA956.* Mechanics of Materials, 1997. **25**(4): p. 255-61.
62. Chen, W. and M.C. Chaturvedi, *On the mechanism of serrated deformation in aged Inconel 718.* Materials Science and Engineering A, 1997. **A229**(1-2): p. 163-168.
63. Ponge, D., M. Bredehoeft, and G. Gottstein, *Dynamic recrystallization in high purity aluminum.* Scripta Materialia, 1997. **37**(11): p. 1769-1775.
64. Coryell, S.P., *Flow Behavior and Microstructural Evolution of Incoloy 945 During High Temperature Deformation*, in *Materials Engineering*2010, Colorado School of Mines: Golden. p. 60-100.
65. Dudova, N., et al., *Dynamic recrystallization mechanisms operating in a Ni-20%Cr alloy under hot-to-warm working.* Acta Materialia, 2010. **58**(10): p. 3624-32.
66. Corwin W., B.T., Halsey W., Hayner G., Katoh Y., Klett J., McGreevy T., Nanstad R., Ren W., Snead L., Stoller R., Wilson D., *Updated Generation IV Reactors Integrated Materials Program Plan Revision 2*, 2005, Department of Energy: Oak Ridge.

Appendix A

Grain Size Images

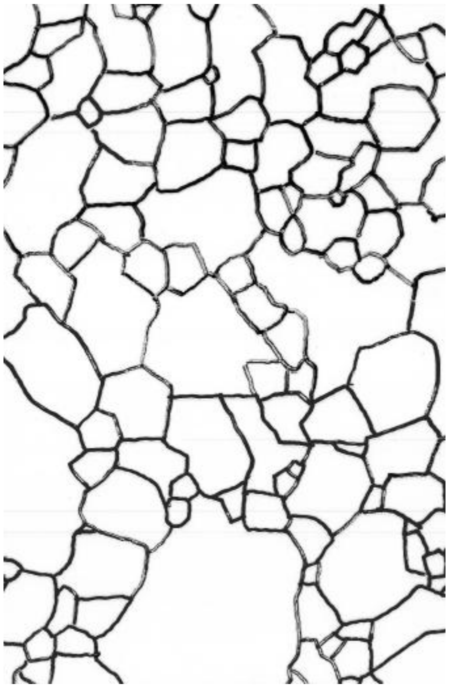

Figure A.1 Transparency used to calculate grain size of as-received Inconel 617

Figure A.2 Transparency used to calculate grain size of Inconel 617 at 800 °C

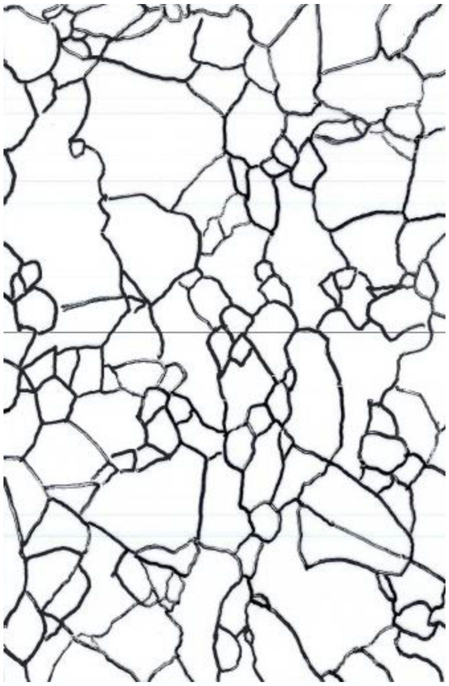

Figure A.3 Transparency used to calculate grain size of as-received Haynes 230

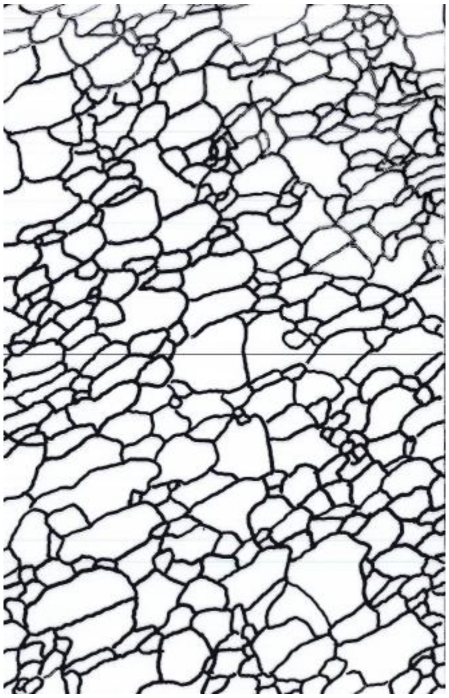

Figure A.4 Transparency used to calculate grain size of Haynes 230 at 800 °C

Appendix B

XRD Spectra

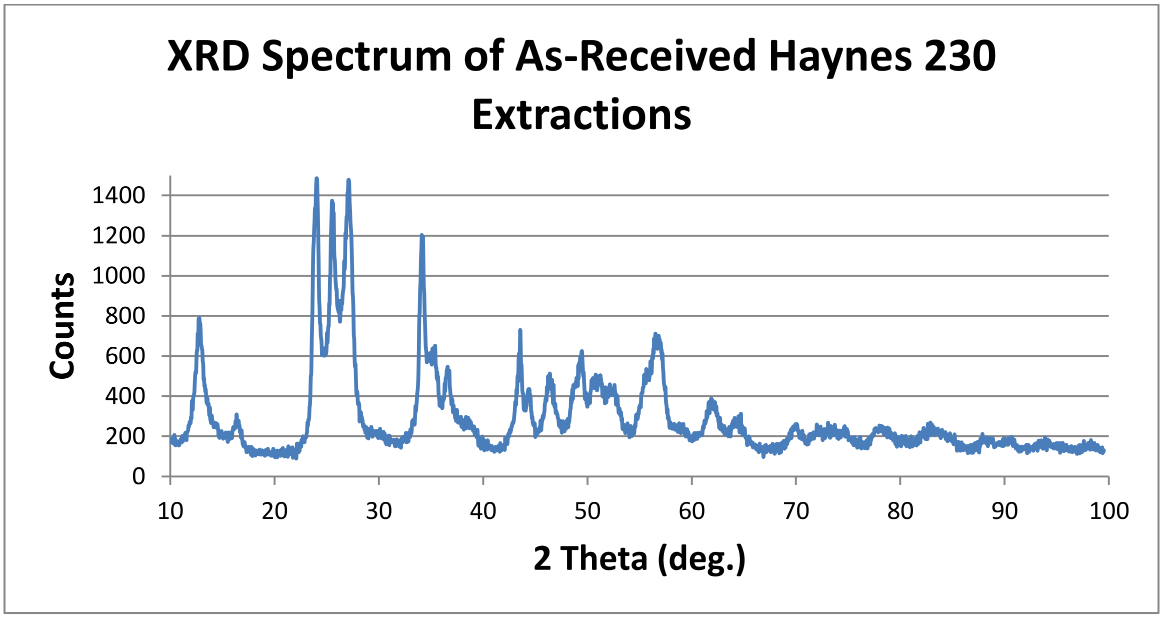

Figure B.1 XRD spectrum of the as-received extractions of Haynes 230

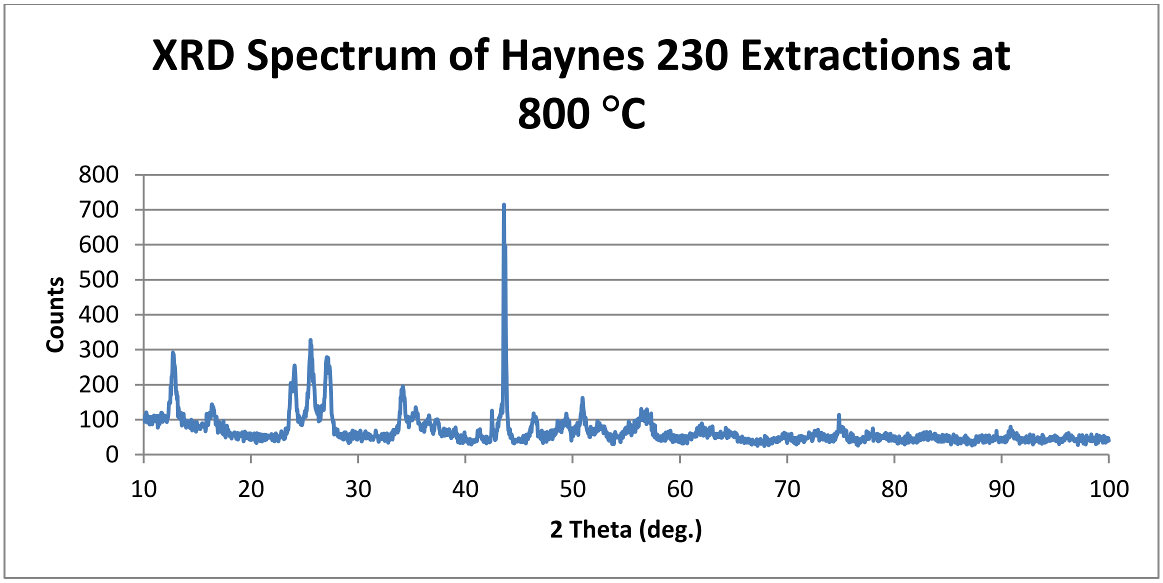

Figure B.2 XRD spectrum of the extractions of Haynes 230 deformed at 800 °C

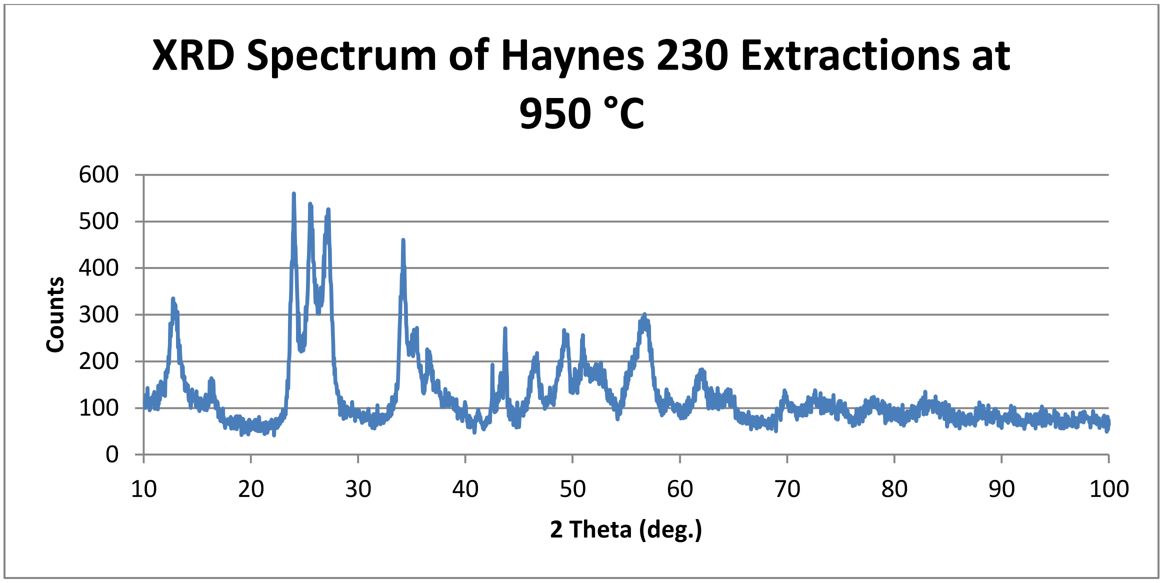

Figure B.3 XRD spectrum of the extractions of Haynes 230 deformed at 950 °C